Spring 5-19-2018

Mutual Information in the Frequency Domain for Application in Biological Systems

Rui Liu
Louisiana Tech University

Spring 5-19-2018

Mutual Information in the Frequency Domain for Application in Biological Systems

Rui Liu

Mutual Information in the Frequency Domain for Application in Biological Systems

by

Rui Liu, M.S.

A Dissertation Presented in Partial Fulfillment
of the Requirements for the Degree
Doctor of Philosophy

COLLEGE OF ENGINEERING AND SCIENCE
LOUISIANA TECH UNIVERSITY

May 2018

LOUISIANA TECH UNIVERSITY

THE GRADUATE SCHOOL

March 26th, 2018

Date

We hereby recommend that the dissertation prepared under our supervision by Rui Liu

entitled Mutual Information in the Frequency Domain for Application in Biological Systems

be accepted in partial fulfillment of the requirements for the Degree of Doctorate of Philosophy in Computational Analysis and Modeling

Supervisor of Dissertation Research

Head of Department

Computational Analysis and Modeling

Department

Recommendation concurred in:

Advisory Committee

Approved:

Director of Graduate Studies

Approved:

Dean of the Graduate School

Dean of the College

GS Form 13a
(6/07)

ABSTRACT

Biological systems are comprised of multiple components that typically interact nonlinearly and produce multiple outputs (time series/signals) with specific frequency characteristics. Although the exact knowledge of the underlying mechanism remains unknown, the outputs observed from these systems can provide the dependency relations through quantitative methods and increase our understanding of the original systems. The nonlinear relations at specific frequencies require advanced dependency measures to capture the generalized interactions beyond typical correlation in the time domain or coherence in the frequency domain. Mutual information from Information Theory is such a quantity that can measure statistical dependency between random variables. Herein, we develop a model–free methodology for detection of nonlinear relations between time series with respect to frequency, that can quantify dependency under a general probabilistic framework. Classic nonlinear dynamical system and their coupled forms (Lorenz, bidirectionally coupled Lorenz, and unidirectionally coupled Macky–Glass systems) are employed to generate artificial data and to test the proposed methodology. Comparisons between the performances of this measure and a conventional linear measure are presented from applications to the artificial data. This set of results indicates that the proposed methodology is better in capturing the dependency between the variables of the systems. This measure of dependency is also applied to a real–world electrophysiological dataset for emotion analysis to

study brain stimuli–response functional connectivity. The results reveal distinct brain regions and specific frequencies that are involved in emotional processing.

Replace this page with the approval for scholarly dissemination form.

DEDICATION

To whoever finds this topic interesting.

TABLE OF CONTENTS

LIST OF FIGURES

NOMENCLATURE

$X(f)$	discrete Fourier transform
$X^A(f)$	magnitude of $X(f)$
$X^\phi(f)$	phase of $X(f)$
$P_{XX}(f)$	auto-spectrum of $x(n)$
$P_{XY}(f)$	cross-spectrum of $x(n)$ and $y(n)$
$p_X(x)$	marginal probability distribution function
$p_{XY}(x,y)$	joint probability distribution function
$p_{X\|Y}(x\|y)$	conditional probability distribution function
ρ_{XY}	correlation
$\mathbf{E}$	expectation operator
$C_{XY}(f)$	coherence
K_H	kernel function
$\mathbf{H}$	bandwidth
$H(X)$	Shannon entropy
$H(X,Y)$	joint entropy
$I(X;Y)$	mutual information
$D_{KL}(P\|\|Q)$	Kullback-Leibler divergence
$h(X)$	differential entropy
$h(X,Y)$	joint differential entropy
$I_{XY}^{AA}(f)$	mutual information between magnitudes
$I_{XY}^{\phi\phi}(f)$	mutual information between phases
$I_{XY}^{A\phi}(f)$	mutual information between magnitude and phase
$SI_i(f)$	cumulative mutual information with respect to i

ACKNOWLEDGMENTS

I thank my doctoral advisor, Dr. Ioannis Vlachos, for his idea of this interesting topic that fits my background and for leading me to the field of applied statistics. I thank the Department of Mathematics and Statistics for offering the proper facility and work environment to conduct this research. I thank each of my committee members for their steady support. Appreciations are extended to Ms. Regina Foster at Prescott Library for her steady support with literature hunting.

CHAPTER 1

INTRODUCTION

1.1 General Concepts

A biological system could be a cell (micro–level), a collection of similar types of cells into an organ, several organs collaborating to accomplish tasks as a functional system (macro–level), or even a complete organism. Viewing biological phenomena from a system perspective gives ideas of both the local component functionality and the overall interaction of different parts within the system. For example, the heart works as a pump in the cardiovascular system to move blood to the whole body through arteries, veins, and capillaries. The heart is also connected with the lungs (part of the respiratory system) to exchange oxygen. Therefore, the concentration of oxygen in the blood affects the heart′s performance as a negative feedback to keep the homeostasis. The heart, blood vessels, the lungs, and airway comprise together the cardiorespiratory system. The cardiovascular system itself has lately been hypothesized to be associated with the nervous system, and abnormal interactions in this system can lead to death among patients with nervous system diseases [6]. In the nervous system, the action potential (an electrochemical impulse) is a micro–level observation per nerve cell for local information transmission, whose mechanism is well understood. On the other hand, the nature of task-specific macro–level communication among

neighboring neurons at a local area or among different brain parts at a larger scale is not fully known. Brain connectivity is a popular topic lately within brain science to better understand the functionality of every single component and their possible collaboration mechanisms on instantaneous performances of multiple tasks.

A major feature of the biological systems is they tend to work in a "repeated" manner during their normal activity. For example, the heart of a healthy individual holds a regular depolarization-repolarization behavior as it is collecting and sending the blood to the whole body. In heart muscle electrical activity recording, this behavior typically produces nonlinear pulses with a constant duration of time (the QRS complex). One can imagine that due to external factors, e.g. physical exercise or aging, the system performance will be sped up or slowed down with a slightly shorter or longer duration but in a similar QRS pattern to keep the organism adapted into the new status and maintain the internal overall stability. This series of repeated actions in time can normally be captured by frequency analysis from biological signal processing. Unlike the heart that works at the macro level, the nerve cell at the micro level generates the action potentials to pass information, and this tiny contribution to the local brain electrical activity at the macro level ends up with rich frequency content. In this context, the single nerve cells, or even neural masses (collection of neurons) are sub-systems or components of the system.

Nonlinearity is inherent in a biological system (e.g., QRS complex, action potential) [7, 8], so component-wise interactions are not always clear. Due to their "repeated" fashion of operation, it is of interest to know at the macro level how one component tunes its routine operation to interact with other components and influence

the overall system performance at a certain frequency. Observable outputs (time series) from different components of a biological system can be collected and frequency features can be extracted. To study the connectivity between system components, we consider a statistical dependency measure, Mutual Information (MI) originally from Information Theory, which is capable of capturing general associations [9], and extend this measure with respect to frequency features. We test the methodology using artificial data and then apply it to a dataset of electrophysiological brain recordings for the study of emotional processing. This new methodology has the potential to reveal aspects of connectivity in biological systems that are not measurable by existing methods.

1.2 Overview

The background to this research is given in Chapter 2. It covers various types of biological systems and their corresponding outputs (signals), the essential frequency perspective of these signals, some common statistical dependency measures in time series analysis, and a general statistical dependency measure –the MI, details regarding brain emotional processing are given in Section 2.5, and common applications of dependency measures in biological systems are presented in Section 2.6.

In Chapter 3 we present the developed methodology to capture nonlinear relation with respect to frequency by MI. We first provide the estimation procedure of MI along with relevant technical aspects in Sections 3.1 and 3.2. The technique of extracting frequency characteristics from time series is then detailed in Section 3.3. Finally, combining all the technical pieces, the model-free method to quantify nonlinear

interactions between biological time series with respect to frequency is described in Section 3.4. Models of coupled nonlinear systems, which are used to evaluate the methodology and a real-world electrophysiological dataset are then discussed in Section 3.5. Results are presented in Chapter 4, and Chapter 5 concludes this work with an evaluation of the methodology, discussions of the physical meaning of the results from the physiological dataset, and a description of future work directions.

CHAPTER 2

BACKGROUND

2.1 Signals from Biological Systems

Biological *signals* are usually recorded through some sensor or device and can represent diverse aspects of the systems characteristics, ranging from electrical activity, to chemical concentrations, or any other characteristic that has dynamic properties (i.e., changes over time). Commonly observed biological signals in research are: electroencephalogram (EEG), magnetoencephalogram (MEG), and blood–oxygen–level dependent (BOLD) signals detected by functional magnetic resonance imaging (fMRI) from the central nervous system; electrocardiogram (ECG), magnetocardiogram (MCG) and blood pressure from the circulatory system; galvanic skin response (GSR) from the autonomic nervous system; and potential of hydrogen (pH) from digestive or urinary systems. Electrograms, including ECG, EEG, electromyogram (EMG), and electrooculogram (EOG), record the electric potential measured between points in tissues as a result of electrochemical activity in certain types of excitable cells [2]. MEG and MCG reflect changes in the magnetic field produced by the electrophysiological activity. Functional MRI measures the brain blood flow activity. GSR records the electrodermal activity. Figure 2.1 graphically presents sample locations and the time profiles of EEG, EOG and EMG signals. Although physiological signals are

inherently different from each other, a nearly universally common characteristic is their quasi–periodic (oscillatory) structure due to specific frequency components [10, 11].

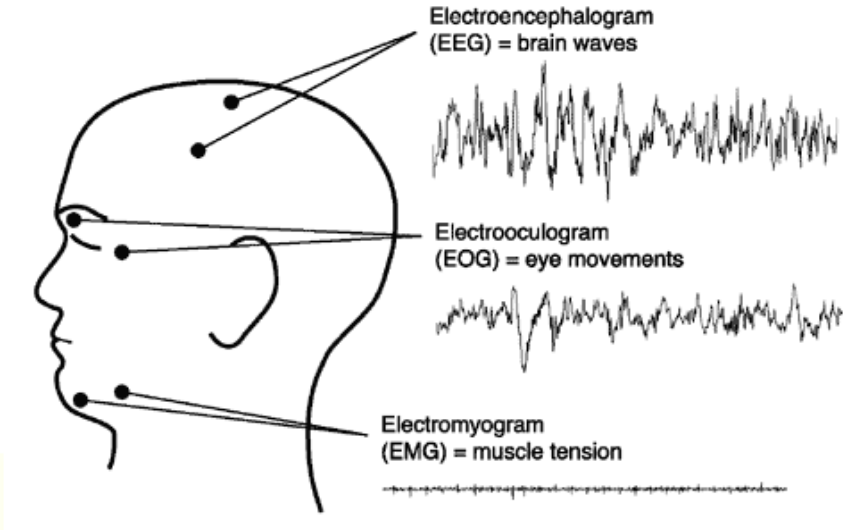

Figure 2.1: Examples of electrophysiological signals. Electroencephalogram, electrooculogram and electromyogram samples and their collection locations [1].

Single modality biological signals (i.e., signals recorded through a similar process, but possibly at different locations) have been employed in research extensively, e.g., to detect distinct frequency components from the human brain [12, 13], to help with the diagnosis of Alzheimer's disease [14, 15, 16], to study epilepsy [17], to estimate flow velocity and Doppler spectra of arterial disease [18], and to understand the anesthetic drug effect [19]. Study on multimodal biological signals (i.e., signals recorded (a) through different methods/devices from the same system, or (b) the same procedure from anatomically different sub–parts of a system) is not so common, but it has been used to reveal the communication between the nervous and cardiac systems, e.g., ECG–fMRI [20], ECG–EEG [6], or the interaction between the circulatory and

the respiratory systems, e.g., MCG based heart rate variability–MCG based respiration [21]. When dealing with signals from different modalities, the analysis methods are limited by the different nature of the signals themselves, and by possible nonlinear interactions among the sub–systems.

The most interesting and important biological system to study is the human brain, due to its complexity and the plethora of signals that it produces. The brain contains approximately 86 billion connected neuronal cells [22]. To execute different brain functions simultaneously, subsets of neurons work together under particular/individual tasks [23]. Furthermore, the different subsets may interact with each other. The normal EEG shows oscillatory activities with amplitudes in the range of 20–100 μV [24]. Physicians describe the EEG typically with "rhythmic and transient" characteristics and divide these activities into specific bands by frequency: δ (0.5–4 Hz), θ (4–8 Hz), α (8–13 Hz), β (13–30 Hz) and γ (30+ Hz).

By clinical convention and for the convenience of communication [25], EEGs are recorded under standard setups with respect to the sensor electrode locations on the head surface. One basic setup is the 10–20 system. First, the nasion and the inion are defined as the distinctly depressed area between the eyes and the lowest point of the skull from the back of the head. They naturally form a nasion–inion circle along the skull. Then the 10–20 system leaves the outermost electrode circle 10% of the total front–back distance from the nasion–inion circle and keeps the distances between adjacent electrodes 20% of the total front–back distance. According to resources availability, the conventional 10–20 system's electrode density can be increased by reducing the inter–electrode distance. A typical extension is the 10–10 system which

holds the 10% division for all measurements. More commonly, *modified combinatorial nomenclature* satisfies most of the applications by employing selected locations of interest from the formal frameworks. A standard 10–20 system montage is shown in Figure 2.2. Letters F, P, T, and O represent *frontal*, *parietal*, *temporal*, and *occipital* lobes (the four main sections of the brain), and C refers the central part of the brain. Odd numbers indicate electrode locations on the left hemisphere, even numbers indicate right hemisphere. Clinical neurophysiologists have observed that α waves of moderate amplitude are prominent in both the parietal and occipital cortices and are representative of relaxed wakefulness. Lower–amplitude β activity is more observed in the frontal area during intense mental activity. A natural transition from α brain activity to β activity may be caused by alerting a relaxed subject. Both θ and δ waves are believed as normal patterns during drowsiness and early stage in sleep, but they may also show certain brain dysfunction for wakeful situation [24]. Recent studies reported high–amplitude γ band oscillations during meditation [26, 27, 28].

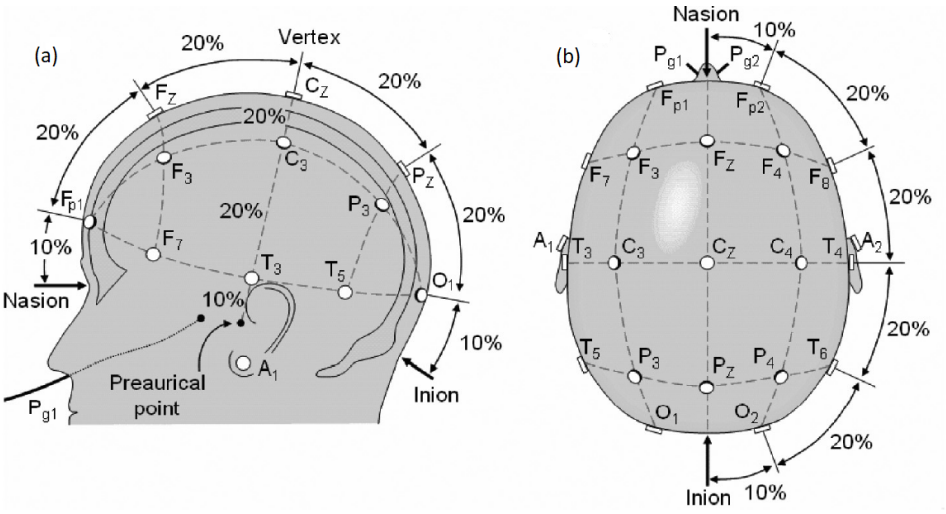

Figure 2.2: The standard 10–20 system setup [2]. Panel (a) is from the left view and panel (b) is from the top view of the head.

Several 10–second duration EEG sample data from selected locations—frontal lobe (Fp1, Fp2 and F3, F4), central brain region (C3 and C4), occipital lobe (O1 and O2)—are displayed in Figure 2.3. We can observe contamination of the signal from eye–movement related activity (eye blink artifacts) in the electrodes on the frontal lobe (i.e., Fp1, Fp2, F3 and F4) as four major spikes within this 10–second duration. We also observe the similar pattern highlighted in red boxes between electrodes from the same hemisphere (i.e., Fp2 and F4). Activity from the central brain locations C3 and C4 are not as similar as the activity from the occipital lobe locations (O1 and O2). Overall, EEG recordings from nearby electrodes tend to be similar because they may capture the same brain activity.

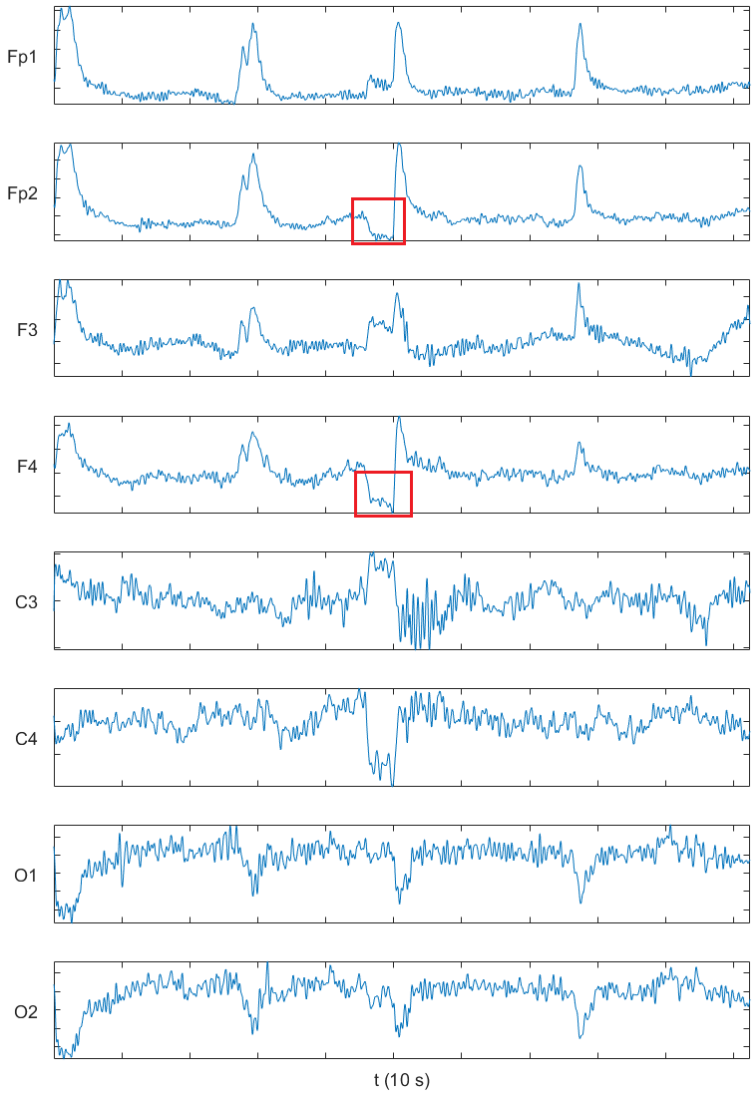

Figure 2.3: 10–second selected electrode EEG sample data. Hemisphere–wise paired electrodes from frontal lobe (Fp1, Fp2 and F3, F4), central brain region (C3 and C4), occipital lobe (O1 and O2).

2.2 The Frequency Domain

In the time domain, a signal is represented by its values arranged in time order. One may consider Fourier analysis as a model that approximates a signal from the time domain by a sum of simpler trigonometric functions (complex exponentials) each

with a distinct frequency f, amplitude, and phase, constituting the frequency domain representative of the signal. Figure 2.4 showcases the time–domain representation and frequency–domain approximation of a continuous signal. Considering the modern data acquisition, transmission, and storage techniques, continuous signals are always digitized to equal–spaced discrete type finite–length recordings. This time–ordered series can be modeled by deterministic formulas as well as considered as *time series* that are generated from stochastic processes. *Discrete Fourier Transform (DFT)* was developed for discrete time series $x(n), n = 1, 2, ..., N$ to perform Fourier analysis:

$$\mathcal{F}\{x(n)\} = X(f) = \sum_{n} x(n)e^{-j2\pi fn}. \tag{2.1}$$

Furthermore, an efficient algorithm for estimation of DTF, the Fast Fourier Transform (FFT) algorithm, has been implemented in many software toolkits as the default method and significantly expanded applications of Fourier analyses to multiple disciplines, e.g., acoustic signal reconstruction and identification, source localization from radar and ultrasound signals [29], or crack detection for infrastructures from image signal [30].

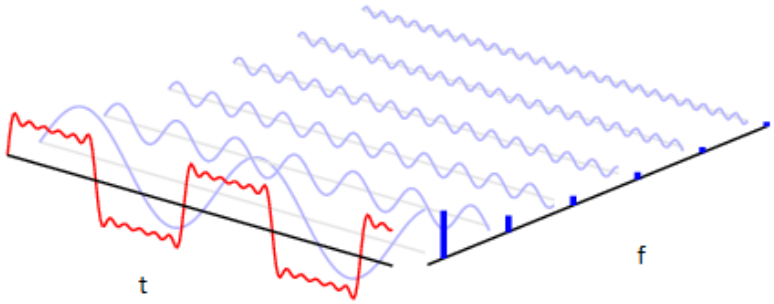

Figure 2.4: Time–domain representation (in red) and frequency–domain approximation (in blue) of the same signal [3].

Usually, the analysis of "frequency content" refers to the distribution of attributes derived from the complex domain representation generated by equation (2.1) over the spectrum (the range of the frequency values). Typical attributes are the magnitude and the phase, which produce the magnitude and phase spectra, respectively (equations (2.2) and (2.3)):

$$X^A(f) = |X(f)|, \tag{2.2}$$

$$X^\phi(f) = \arctan\left\{\frac{\mathrm{Im}\{X(f)\}}{\mathrm{Re}\{X(f)\}}\right\}. \tag{2.3}$$

where $\mathrm{Im}\{\cdot\}$ denotes the imaginary part of a complex value and $\mathrm{Re}\{\cdot\}$ denotes the real part. Spectral analysis, which focuses on power spectrum (magnitude) estimation, grew as a branch from modern signal processing. A classic nonparametric method to estimate the power spectrum (power spectral density) is the *periodogram* calculated through DFT in equation (2.4).

$$P_{XX}(f) = |X(f)|^2 \tag{2.4}$$

Modifications for accurate estimation of magnitude and phase are addressed in Section 3.3.

Frequency domain analysis has found numerous applications in the study of biological signals to assist diagnostic procedures, and prediction and intervention in the cardiovascular, respiratory, and nervous systems [10]. Examples of these applications include a study of different brain regions under resting state found correlation relationship of EEG and fMRI signals at the α frequency band [31], various Fourier analysis methods were applied to examine biological transients phenomena [32], DFT helped detect high–frequency content in arrhythmia–free intervals from ECG [33], dynamic spectral representation of electrogastrographic signals has been proved as a valid method to study gastric myoelectrical activity [34], and spectral analysis based features have been employed to contribute to the analysis of electromyography signals [35].

2.3 Statistical Dependency

In the context of probability theory, any random variable X that represents some measurable quantity is associated with a probability distribution P (probability mass function for discrete case and probability density function for continuous case –$p(x)$). Consider two random variables X and Y, $p_{XY}(x, y)$ is the joint probability distribution function (the distribution for all possible pairs of x, y), $p_X(x)$ and $p_Y(y)$ are their marginal probability distribution functions (probability distribution of one random variable disregarding the values of the other), and $p_{X|Y}(x|y)$ and $p_{Y|X}(y|x)$ are the conditional probability distribution functions (distribution of one of the random

variables when the other has a fixed value) [36]. If the joint probability is equal to the product of the marginal probabilities (equation (2.5)), or if the marginal distribution of one variable is equal to the conditional with respect to the other (equation (2.6)) for all pairs of x and y, the two random variables are independent.

$$p_{XY}(x, y) = p_X(x)p_Y(y) \tag{2.5}$$

$$p_{X|Y}(x|y) = p_X(x) \tag{2.6}$$

In contrast, when these equalities do not hold, X and Y are dependent. Furthermore, neither of these criteria offer a way to measure the strength of dependency once the equality fails. In this section, two statistical measures that quantify linear dependency between two random variables (i.e., X and Y satisfy the relation $Y = aX + b$, where a and b are constants) are discussed.

Correlation is a simple statistical measure to capture the linear dependency or association. British biostatistician Karl Pearson first developed and coined the Pearson's correlation coefficient from linear regression in the form of a fraction between the covariance and the product of standard deviations of X and Y as in equation (2.7).

$$\rho_{X,Y} = \frac{\mathbf{E}[(X - \mu_X)(Y - \mu_Y)]}{\sqrt{\mathbf{E}(X - \mu_X)^2\mathbf{E}(Y - \mu_Y)^2}}, \tag{2.7}$$

where $\mathbf{E}$ is the expectation operator ($\mathbf{E} = \sum p(x)x$ or $\mathbf{E} = \int p(x)xdx$) and μ_X, μ_Y are the expectations of random variable X and Y respectively. From equation (2.7) we note that correlation is a symmetric quantity with a range of $[-1, 1]$, where values 1 and -1 represent the perfect positive and negative linear correlation (dependency)

between the two random variables, exact value 0 represents the case of no linear correlation, and other values indicate the strength of linear dependency. However, one can not infer the independence of variables directly by observing $\rho_{X,Y} = 0$ because it only reflects a linear relationship. A typical example is $Y = X^2$, where X was a probability distribution symmetric about 0. Apparently X and Y are dependent through the square operator; however, correlation gives the value of exact 0. Four cases of relations are plotted and evaluated by Pearson's correlation coefficient in Figure 2.5. Correlation is good at capturing purely linear dependency (panel (a) and (b)), or not capturing any relation when the random variables are independent (panel (c)), but it has the potentials of misinterpretation in cases of more general nonlinear dependency (panel (d)).

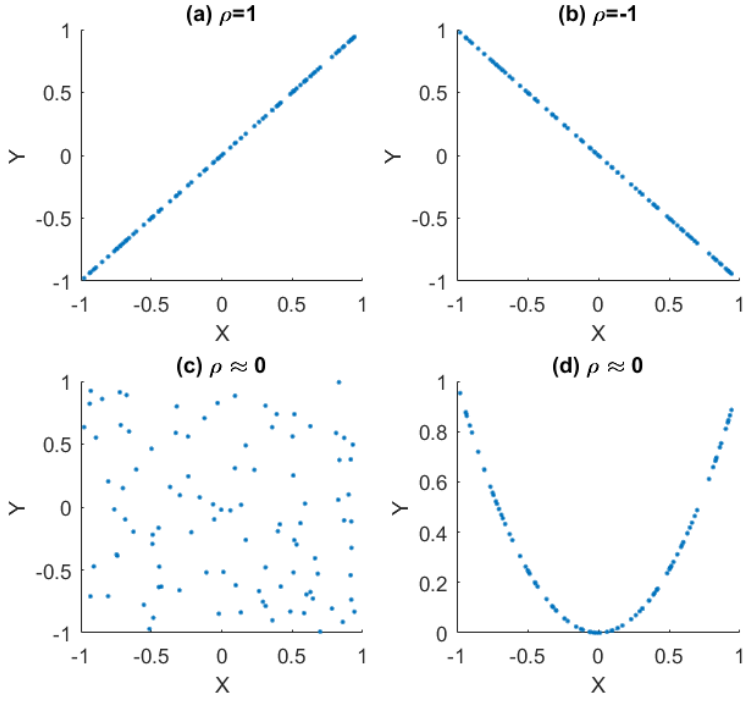

Figure 2.5: Examples of Pearson's correlation coefficients evaluating dependency between X and Y: (a) positive correlation $Y = X$, (b) negative correlation $Y = -X$, (c) independent X and Y, (d) linearly uncorrelated but nonlinear–dependent case $Y = X^2$.

Correspondingly, for two signals in the time domain $x(n)$ and $y(n)$, the Magnitude–Squared Coherence (MSC) is a frequency–dependent real function [37] defined as the *cross–spectral density* $P_{XY}(f)$ between $x(n)$ and $y(n)$ normalized by the product of the *auto–spectral densities* $P_{XX}(f)$ and $P_{YY}(f)$ that quantifies the linear dependency of the two signals at frequency f in equation (2.8).

$$C_{XY}(f) = \frac{|P_{XY}(f)|^2}{P_{XX}(f)P_{YY}(f)} \tag{2.8}$$

The MSC in equation (2.8) could be derived as equation (2.9)

$$C_{XY}(f) = \frac{\left|\mathbf{E}[X(f)Y^*(f)]\right|^2}{\mathbf{E}\left[|X(f)|^2\right]\mathbf{E}\left[|Y(f)|^2\right]} \tag{2.9}$$

and estimated by splitting the original signals into n_d segments and estimating the average power spectra from these segments (i.e., $x_i(n), i = 1, 2, ..., n_d$). With respective $X_i(f)$ as [38]:

$$\hat{C}_{XY}(f) = \frac{\left| \sum_{i=1}^{n_d} X_i(f) Y_i^*(f) \right|^2}{\sum_{i=1}^{n_d} |X_i(f)|^2 \sum_{i=1}^{n_d} |Y_i(f)|^2}. \tag{2.10}$$

Due to its simplicity in estimation, MSC is one of the most commonly used measures of dependency in research fields with oscillatory–rich signals, e.g., meteorology [39, 40], oceanology [41], and neuroscience [42, 43, 44, 45]. MSC is with a range of $[0, 1]$, taking value 0 when $x(n)$ and $y(n)$ are uncorrelated at frequency f and 1 when they hold a perfect linear relation. Similar to correlation, when the relation at a given frequency is nonlinear, MSC may produce misleading results. An example of MSC estimated from two periodic discrete signals contaminated with additive noise is shown in Figure 2.6. Panels (a) and (c) display $x(n) = \sin(f_1 n) + \sin(f_2 n) + e_1(n)$ and $y(n) = \sin^2(f_1 n) + \sin(f_2 n) + e_2(n)$ in the time domain, where $f_1 = 2$ Hz, $f_2 = 18$ Hz and $e(n)$ is Gaussian white noise. Panels (b) and (d) show their corresponding power spectra. $x(n)$ and $y(n)$ containing two frequency components respectively, including a nonlinear (square) operator of f_1 and a common frequency component f_2. In panel (e), coherence estimation exhibits single extreme value (equal to 1) around f_2 but gives no clue of the relation at frequency f_1. MSC has also been extended to Partial Coherence to study multivariate time series [46] and combined with vector autoregressive modeling and developed into Partial Directed Coherence to detect direct dynamic multivariate process relationships [47, 48].

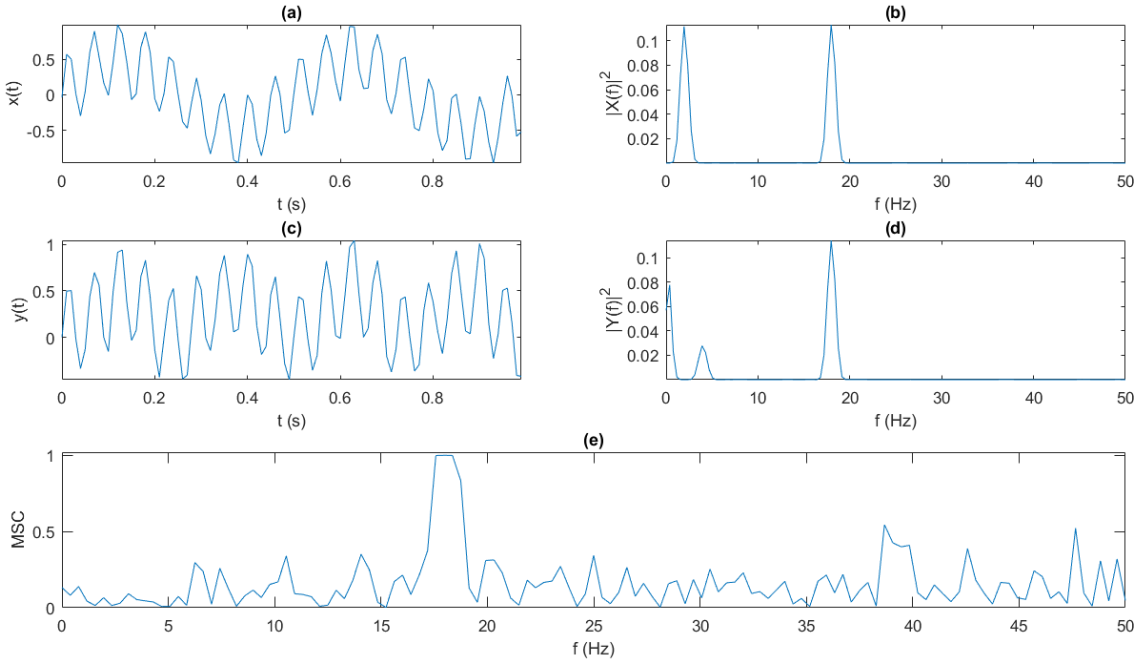

Figure 2.6: An example of MSC: (a)–(b) sample series $x(n)$ and its power spectrum, (c)–(d) sample series $y(n)$ and its power spectrum, (e) MSC estimation between $x(n)$ and $y(n)$ (see text for details).

2.4 Information Theory

The history of Information Theory stems from an American mathematician, Claude Shannon [49], while he was working on communication theory and cryptography during World War II for the U.S. government. As a fundamental work, Shannon defined two important quantities: *information entropy* and MI (although without coining the name). Information entropy $H(X)$ (commonly called Shannon entropy) is "a measure of information, choice and uncertainty". In pursuing some ideal properties described in his original paper (Part I Section 6) [49], *information* was defined as the logarithm of the reciprocal of the probability mass function values, and entropy as the

average of information (equation (2.11)):

$$H(X) = \mathbf{E}\Big[\log \frac{1}{p_X(x)}\Big] = \sum_x p_X(x) \log \frac{1}{p_X(x)}. \tag{2.11}$$

Shannon entropy has units of *bits* or *nats* depending on the base of the logarithm function (2 or e). Similar to equation (2.11) for single variable, entropy for joint random variables is *joint entropy* $H(X,Y) = -\mathbf{E}\big[\log p_{XY}(x,y)\big]$, and entropy for the case of conditional probability mass functions is *conditional entropy* $H(X|Y) = -\mathbf{E}\big[\log p_{X|Y}(x|y)\big]$. Shannon entropy holds some nice properties i.e., non–negativity, reducing by value when conditioning on another random variable, and reaching its maximum value for the uniform distribution. Due to the product identity of the logarithmic function in equation (2.11), entropy of joint random variables can be derived from a chain rule that connects the marginal entropy $H(X)$ or $H(Y)$, the conditional entropy $H(X|Y)$ or $H(Y|X)$, and the joint entropy $H(X,Y)$ in the form of equation (2.12).

$$H(X,Y) = H(X) + H(Y|X) = H(Y) + H(X|Y) \tag{2.12}$$

Shannon entropy is widely employed to assist clustering biological microarray data [50] and to identify electrophysiological signal patterns [51].

The mathematical formula of MI, $I(X;Y)$, was initially developed to study the channel capacity in a communication system, and then for guiding the development of multiple compression techniques.

$$I(X;Y) = \mathbf{E}\Big[\log \frac{p_{XY}(x,y)}{p_X(x)p_Y(y)}\Big] = \sum_{x,y} p_{XY}(x,y) \log \frac{p_{XY}(x,y)}{p_X(x)p_Y(y)} \tag{2.13}$$

As explained in the Venn diagram in Figure 2.7, MI represents the shared information between two random variables X and Y, and can be written as

$$\begin{aligned} I(X;Y) &= H(X) + H(Y) - H(X,Y) \\ I(X;Y) &= H(X) - H(X|Y). \end{aligned} \tag{2.14}$$

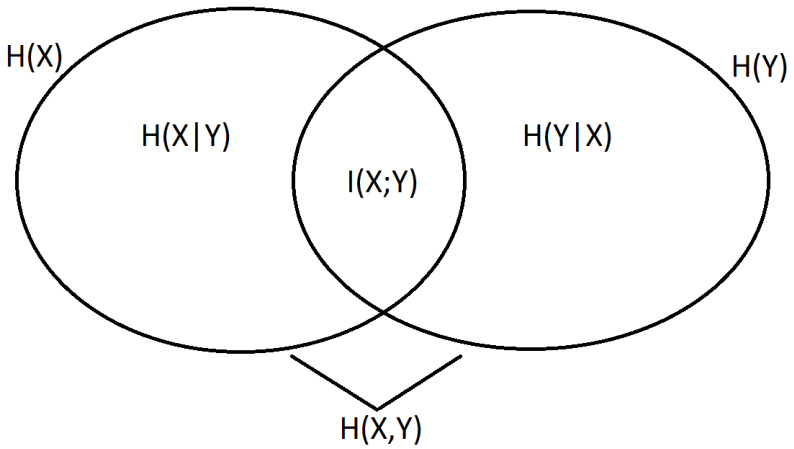

Figure 2.7: Venn diagram representing the relation between variable X and Y in terms of entropy $H(X)$, $H(Y)$, conditional entropy $H(X|Y)$, $H(Y|X)$, joint entropy $H(X,Y)$, and MI $I(X;Y)$.

MI is closely related to another quantity from statistics, the *Kullback–Leibler (KL) divergence*. Concerning statistical discrimination, American mathematician Kullback and cryptanalyst Leibler proposed KL divergence as a "measure of the distance or divergence between statistical populations" (probability distributions with the same support x) and denoted as $D_{KL}(P||Q)$ [52].

$$D_{KL}(P||Q) = \sum_{x} p(x) \log \frac{p(x)}{q(x)} \tag{2.15}$$

This quantity is also used in information theory and coined as relative entropy. We note that relative entropy is a non–negative, asymmetric quantity, it is only zero when the two distributions are exactly the same, i.e., $p(x) = q(x)$. MI can be interpreted in terms of KL divergence. If we consider to replace $p(x)$ in equation (2.15) with the joint probability mass function $p_{XY}(x, y)$, and $q(x)$ with the product of the corresponding marginal probabilities $p_X(x)p_Y(y)$, then MI is acquired. In consideration of the divergence/similarity perspective from relative entropy applied to the two distributions $p_{XY}(x, y)$ and $p_X(x)p_Y(y)$, MI could be interpreted as the similarity between the real joint probability distribution and an "imagined" joint distribution under the assumption of independence between the random variables X and Y. High MI values indicate X and Y are more dependent, low MI values imply they are less dependent, and exact zero means the random variables are independent.

There are multiple estimation methods for MI from sample data. The naïve solution is to approximate the marginal and joint probability distribution functions through binning [53], or kernel density estimation [54], and plug the empirical probability functions into equation (2.13). A resubstitution method was proposed based on the averaging definition of MI and generalized to the empirical mean across samples [55]. Sample–spacing estimate and nearest–neighbor distance are also advanced approaches [55, 56, 57]

MI could also be generalized to multivariate random variables and be derived from chain rules by expanding the logarithm function [58, 59]. Bioinformaticians found use of MI in gene expression to detect relationships between two or more variables [60, 61, 62, 56], and MI variants have been shown to be able to characterize the

complexity and the information transmission between cortical areas in patients with Alzheimer's disease [63] and schizophrenia [64].

Although the initial applications of entropy were mostly within the discrete case, Shannon also extended the concept of entropy for continuous distributions informally (differential entropy). Unlike probability mass functions (pmf) in the definition of Shannon entropy, probability density functions (pdf) are used in differential entropy. *Differential entropy* and mutual information for continuous random variables are discussed in detail in Chapter 3.

2.5 Brain and Emotions

Research on understanding brain and emotion processes was initiated by physiologists. German anatomist Brodmann first studied animal brains and inferred distinct anatomical brain regions. Through experiments, Brodmann Areas 39 and 47 in the parietal and frontal cortices were reported to be associated with functionalities like attention and emotion regulation [24]. From another point of view, psychological models were proposed from environmental psychology to quantitatively describe and measure emotions. Among the work in this direction, the most prevalent theory and the most practical one is Russell's circumplex model of affective states [4]. Russell proposed one dimension to represent the level of pleasure or unpleasure of one's feeling (*valence* scale), and a second dimension (*arousal scale*) that depicts the level of alertness involved in the emotion process. Most human emotions can be mapped in this model at distinct locations (see Figure 2.8). Under this construction, *serene* and *happy* are with the same scale of positive valence but with high and low states of

arousal respectively, so are negative valence related emotions, e.g., *upset* and *sad*. A third dimension (dominance scale) was added into this circumplex model afterward and formed the Pleasure–Arousal–Dominance (PAD) emotional state model by Mehrabian [65].

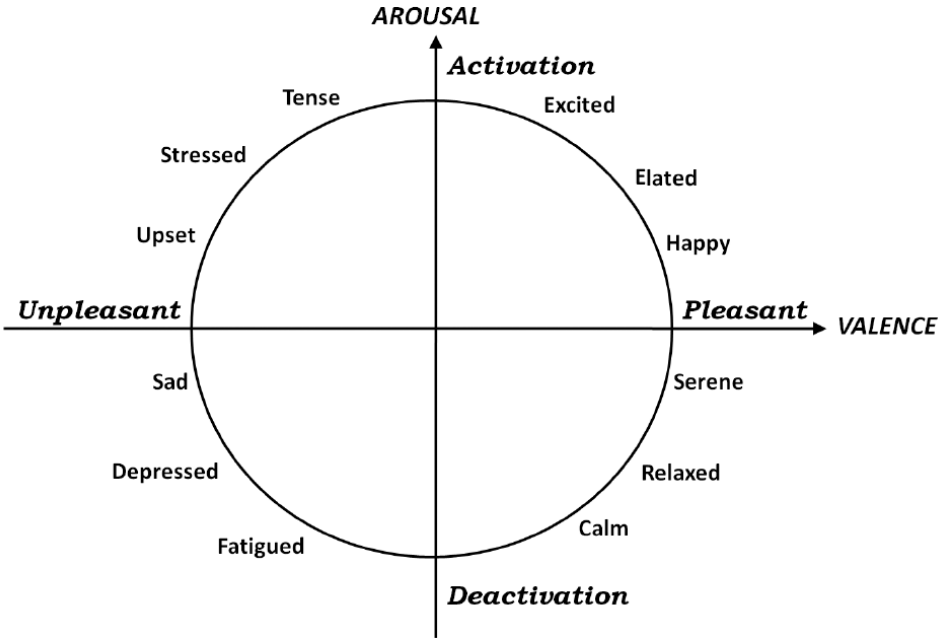

Figure 2.8: Circumplex model of affective states [4]. Emotions are mapped into this space according to numeric quantification along the valence and arousal dimensions.

Following the psychological emotion model, computational neuroscientists found their way of making contributions to emotion recognition and understanding of brain functional connectivity in processing emotions by quantitative analysis of brain data (EEG, MEG, and fMRI). Some early work on building emotion identification systems pointed out certain brain locations to work with, e.g., frontal lobe [66]. Regarding measures for EEG–based emotion recognition, fractal dimensions [67], spectral power, coherence, and MI estimation based on amplitude modulation envelopes [68] have

been applied. Asymmetry in hemispheres has been observed [68] and even employed to develop features to detect valence or arousal states [69]. Among frequency bands, γ band is paid special attention in processing emotion stimuli [70]. Group neural firing related to an event (i.e., event–related desynchronization or event–related synchronization) in the γ band of MEG was reported in a study of the emotion of fear and then generalized to consciousness [71, 72]. Some interesting findings about emotion processing and brain functional connectivity include emotional arousal induced by music by covariance maps of spectral power from EEG revealed a right–frontal suppression of lower α–band activity during high arousal [73]; emotional arousal generated higher influence in the right hemisphere than the left hemisphere, while the occipital cortex is involved more than the occipito–parietal region in processing arousal [74]; for valence, left frontal cortical activity is higher than the right no matter the positive or negative strength of valence [75]; negative valence causes more power over the left temporal region compared to the right, and laterality shift for positive valence [70]; another work on fMRI claimed that sound–processing and speech–comprehension network is more involved in high arousal state, whereas circuitries supporting emotional and self–referential processing are more involved with negative valence [76]. In addition, statistically separable bodily sensations have been shown to be associated with different emotions both in different culture populations and in certain age groups [77, 78], and the emotional significance of visual stimuli can modulate the perceptual encoding in the visual cortex [79].

2.6 Dependency in Biological Systems

Statistical dependency measures introduced in Section 2.3 (correlation and coherence) and 2.4 (MI) have been heavily employed in studies of biological systems [21, 80].

Correlation has been applied to several problems. For example, a negative correlated relationship has been shown between parietal and frontal cortices in α band power [31], and the properties of EEG and heart rate variability strongly correlate with sleep states [81]. Also, correlation has been widely employed in multivariate EEG studies to assess seizure dynamics for epilepsy patients [82]. Coherence has been used to quantify various relations, including the interaction between motor cortex measured with MEG, and hand muscles measured with EMG, during precision grip tasks [45]. The relationship between brain regional fMRI or EEG time series in studies of brain functional connectivity networks [83, 42], and the relationship between local field potentials and simultaneous EEG at thalamocortical θ band in Parkinson's disease patients [44] were investigated through coherence. Variants developed from coherence include imaginary part of coherency [84] and partial directed coherence in testing directed influences among neural signals and in determining neural structure [47, 48]. These are popular measures in the context of brain interaction research, due to the insensitivity in capturing false connectivity arising from volume conduction [84] and the reflection of a frequency–domain representation of causality [47, 48].

MI as a general statistical dependency measure has been applied to the time domain to study brain dynamics, e.g., EEG patterns in patients with Alzheimer's disease [63, 14, 15], in patients with schizophrenia [64], and to support feature extraction

from heart rate variability in classifying patients after acute myocardial infarction [21]. It has also been used as an evaluation metric on EEG features post–processing for estimation of brain affective states [68]. Brain functional connectivity has been explored by time–frequency based MI from EEG and MEG during motor real and imaginary tasks [85, 86, 87]. Furthermore, mutual information was used to detect the association between high γ and θ oscillations in the human neocortex [80].

CHAPTER 3

METHODS

The measure of MI is considered as a reliable metric of the statistical dependency of two random variables [62, 88, 9]. Our aim is to derive appropriate formulations of MI between two signals as functions of frequency, using the representation of the signals in the frequency domain. The core idea of our approach is that the observed time series values in the time domain are less informative than the spectral characteristics we observe in the frequency domain (magnitude and phase).

3.1 Mutual Information

In Section 2.4, we discussed Shannon entropy and mutual information for discrete random variables. Since the spectral characteristics we are working with are continuous random variables, this section will focus on differential entropy and the corresponding MI concepts and estimation.

Similar to Shannon entropy for a discrete random variable as in equation (2.11), differential entropy, $h(X)$, for a continuous random variable X with pdf $p_X(x)$ is defined as the expectation of an analogous "information" quantity:

$$h(X) = \mathbf{E}\Big[\log \frac{1}{p_X(x)}\Big] = \int_x p_X(x) \log \frac{1}{p_X(x)} dx. \tag{3.1}$$

The main difference is that instead of the sum in equation (2.11), differential entropy uses integration since $p_X(x)$ is a continuous function. Therefore, the differential entropy for joint random variables X and Y is

$$h(X,Y) = \mathbf{E}\Big[\log \frac{1}{p_{XY}(x,y)}\Big] = \int_{x,y} p_{XY}(x,y) \log \frac{1}{p_{XY}(x,y)} dxdy, \tag{3.2}$$

and when X is conditioned on Y the differential entropy of X is

$$h(X|Y) = \mathbf{E}\Big[\log \frac{1}{p_{X|Y}(x|y)}\Big] = \int_{x,y} p_{XY}(x,y) \log \frac{1}{p_{X|Y}(x|y)} dxdy. \tag{3.3}$$

Differential entropy does not always hold the non–negativity property compared with Shannon entropy. This is because the pdf for a continuous random variable $p_X(x)$ has a constant area under the curve $\int_x p_X(x)dx = 1$, but the function values can exceed 1. However, differential entropy and Shannon entropy share most of the other properties, e.g., conditioning reduces its value ($h(X) \geqslant h(X|Y)$) and chain rule relation is valid ($h(X,Y) = h(X) + h(X|Y)$).

The mutual information for continuous random variables X and Y with marginal pdfs $p_X(x), p_Y(y)$ and joint pdf $p_{XY}(x,y)$ is defined as:

$$I(X;Y) = \mathbf{E}\Big[\log \frac{p_{XY}(x,y)}{p_X(x)p_Y(y)}\Big] = \int_{x,y} p_{XY}(x,y) \log \frac{p_{XY}(x,y)}{p_X(x)p_Y(y)} dxdy. \tag{3.4}$$

The interpretation is the same as in the case of discrete random variables. Continuous MI takes high values when X and Y are more dependent, low values when they are less dependent, and zero when they are independent. Continuous MI is a non–negative quantity and is a limit case of the discrete MI [59]. Equations (2.14) still hold for

continuous MI as:

$$I(X;Y) = h(X) + h(Y) - h(X,Y),$$
$$I(X;Y) = h(X) - h(X|Y). \tag{3.5}$$

An estimate of continuous MI from sample data is derived from its "expectation" definition in equation (3.4) and coined as "resubstitution" method described by equation (3.6).

$$I(X;Y) \approx \frac{1}{n}\sum_{i=1}^{n} \log \frac{p_{XY}(x_i, y_i)}{p_X(x_i)p_Y(y_i)}, \tag{3.6}$$

where $(x_i, y_i), i = 1, ..., n$ denote a sample data set, $p_X(x_i)$, $p_Y(y_i)$ and $p_{XY}(x_i, y_i)$ are the marginal and joint pdf evaluations at (x_i, y_i), and n is sufficiently large. Equation (3.6) aims to approximate the expectation operator with the sample average derived from the observed data.

3.2 Kernel Density Estimation

The goal of density estimation is to take a finite sample of data and to make inferences about the underlying pdf. A simple solution is the *histogram* which assigns data to bins by value and counts the number of samples per bin. The histogram provides a discretized version of the pdf from data due to the binning procedure (in essence a pmf), but it requires proper selection of the number or size of bins. In contrast, *kernel density estimate* (KDE) is able to provide an estimate of continuous pdf. In KDE for the 1–dimension case (one random variable X), the contribution of each data point is smoothed out from a single point to an interval around it. Aggregating the individual contributions together gives an overall form of the density function. Also known as *empirical probability density function* [89], the kernel estimator

of $p_X(x)$ for a sample of M points $x_i, i = 1, 2, ...M$ is of the form [90]

$$\hat{p}_X(x) = \frac{1}{M} \sum_{i=1}^{M} K_{\mathbf{H}}(x - x_i) \tag{3.7}$$

where $K_{\mathbf{H}}$ is itself a probability density, called a kernel function with variance controlled by a smoothing parameter $\mathbf{H}$ called the bandwidth. Usually, a symmetric function with mean 0 is adopted as $K_{\mathbf{H}}$, and it is generally agreed that the exact shape (i.e., the function) is less important compared with the smoothing parameter $\mathbf{H}$ [89, 90, 91]. This means different types of kernel functions can produce similar density function estimates with proper selection of bandwidth. This nonparametric density estimation approach can be generalized to multivariate probability density estimation by generalizing equation (3.7) to higher dimensions with multivariate kernel functions [91].

The concept of density estimation is defined for variables with support (range of values) of the whole real line ($x \in \mathbf{R}$), but can be adapted to data of different types. The natural domain of a 1–dimension density may not be the whole real line but an interval bounded on one or both sides [91]. However, by construction, the kernel functions centered on the observations which are very close to the boundary have leakage to the unsupported region. Bowman and Azzalini suggest two ways to solve this problem: one is to transform the bound–support variable to a new variable with unbounded support (e.g., through logarithmic transform), the other is to carefully modify the kernel functions near the boundaries [90].

A particular type of bounded–support data is circular or directional data. One may consider circular data as angular measurements that can be mapped on

the circumference of a unit circle. This type of data has been studied in different disciplines, e.g., wind direction in environmental sciences [92]. One distinctive feature of circular data is that the values are restricted in a range (e.g., $[0, 2\pi]$ its period), and the end point coincide with the beginning point. In *Directional statistics*, circular probability distributions (e.g., von Mises circular distribution, etc. [93]) form a natural collection of kernel functions when constructing a density estimate for circular data. Alternatively, a similar result can be achieved by another method called "circular padding" that wraps the data around the boundaries [91]. In this approach, the data are replicated over the adjoining ranges to account for the circularity in the contribution of each observation [90]. Sub–sections 3.2.1–3.2.3 focus on 2–dimension KDE for different types of support.

3.2.1 Planar Density

Conventional KDE to estimate the joint pdf of X, Y defined on unbounded support based on a set containing M samples $(x_i, y_i), i = 1, 2, ..., M$ is given by equation (3.8)

$$\hat{p}_{XY}(x, y) = \frac{1}{M} \sum_{i=1}^{M} K_{\mathbf{H}}(x - x_i, y - y_i), \tag{3.8}$$

where $K_{\mathbf{H}}(x, y)$ is the 2–dimension *Gaussian* kernel function in the form of equation (3.9) with the bandwidth matrix $\mathbf{H}$ in formula (3.10).

$$K_{\mathbf{H}}(x, y) = \frac{1}{2\pi} |\mathbf{H}|^{-\frac{1}{2}} e^{-\frac{1}{2}[x\, y]\mathbf{H}^{-1}[x\, y]^T} \tag{3.9}$$

$$\mathbf{H} = \begin{bmatrix} H_{xx}^2 & 0 \\ 0 & H_{yy}^2 \end{bmatrix} \tag{3.10}$$

Equation (3.8) states for any point denoted by (x, y) on the continuous plane, its pdf is contributed by the averaged effect from all the available sample data points (x_i, y_i). Equations (3.9) and (3.10) together indicate that the kernel functions for each sample data point are of a constant size, and their shape is defined by the longitude/latitude bandwidths (H_{xx} and H_{yy}) only. The diagonal elements of $\mathbf{H}$ can be calculated based on Silverman's rule with the median absolute deviation (mad) of the random variable normalized by the z–score of 50% of the standard normal distribution (approximately 0.6745) as:

$$H_{xx} = M^{-\frac{1}{6}}\hat{\sigma_x} = M^{-\frac{1}{6}}\frac{1}{0.6745}\text{median}\Big\{\big|x_i - \text{median}\{x_i\}\big|\Big\}, \tag{3.11}$$

and similarly for H_{yy}.

3.2.2 Toroidal Density

If both X and Y are circular random variables with a periodic support, their joint distribution is identified as a toroidal distribution [94]. Herein, a modified density estimation strategy is considered for this case. First, along the meridian and equator directions, the torus model is unfolded into a rectangular plane and then a circular padding technique is performed along these two directions to compensate for the effect of samples close to the boundaries. A conventional planar kernel density estimate is applied to the padded plane with Silverman′s rule applied to circular dispersions $\hat{\sigma}_x^c$ as [93]:

$$H_{xx} = M^{-\frac{1}{6}}\hat{\sigma}_x^c = M^{-\frac{1}{6}}\sqrt{2\Big[1 - \Big|\frac{1}{M}\sum_{i=1}^{M} e^{jx_i}\Big|\Big]}, \tag{3.12}$$

and H_{yy} similarly. Finally, the density function over only the original range is selected as the toroidal density function estimate.

3.2.3 Cylindrical Density

For mixed type random variables (i.e., one is non–bounded random variable and the other has a circular distribution), these two dimensions naturally form a cylindrical object. Therefore a circular padding is performed along the dimension of the circular variable only. In this case, the cylinder model is unfolded and turned into a rectangular plane and the padding procedure forms a head and tail connection of three identical rectangular planes along the circular variable dimension. Equations (3.11) and (3.12) are combined and applied to the 2–dimension kernel bandwidth in this case.

3.3 Estimation of Spectral Characteristics

In power spectrum estimation the accuracy of the power distribution is essential; however, problems like *spectral leakage* in the estimation make it difficult. Spectral leakage describes a phenomenon that the power at an intrinsic frequency (in the original signal) not only appears at its actual location in the estimated spectrum but also appears (repeatedly) at other frequencies and influences the global view. There are two aspects of leakage sources, specifically: one is leakage at nearby frequencies due to the sharp truncation at the end of the time–domain finite length signal, and the other is distant frequency leakage stemming from the sampling procedure from the continuous signal. For the first type, since the periodogram from a truncated time series of length N could be considered as a same–length rectangular window tapered

(multiplied) time series undergoing DFT, an alternative window with an arch shape that gradually suppresses the signal values from the middle to the endpoints is able to reduce the truncation effect and lead to a more accurate local frequency estimation. A commonly used window function in analysis of biological signals is the Hamming window given by:

$$\omega_H(n) = 0.54 - 0.46\cos\Big(\frac{2\pi n}{N-1}\Big), n = 1, 2, ..., N. \tag{3.13}$$

Each value of the original signal $x(n)$ is multiplied by $\omega_H(n)$ prior to the estimation of DFT.

For the second type of frequency leakage, the only thing we can do is to strictly follow the Nyquist theorem, which requires the sampling frequency to be at least double the highest frequency component of interest. This restriction limits the frequency activities we can study from available biological recordings.

An example of usage of a Hamming window v.s. no windowing is shown in Figure 3.1. Panel (a) displays a 4–sec EEG time series in the time domain preprocessed by a 0.5–45 Hz fifth–order Butterworth bandpass filter. The same signal tapered by a same duration Hamming window is shown in panel (b). Signal amplitude in the first and the last second are suppressed and the endpoints of the modified signal approach zero value. Although both the magnitude estimated through DFT show a decreasing trend from low frequency to high frequency in panels (c) and (d), the Hamming window modified signal in panel (d) is with less local fluctuations across the spectrum. Phase plots from the original time series and from the modified series are also shown in panels (e) and (f).

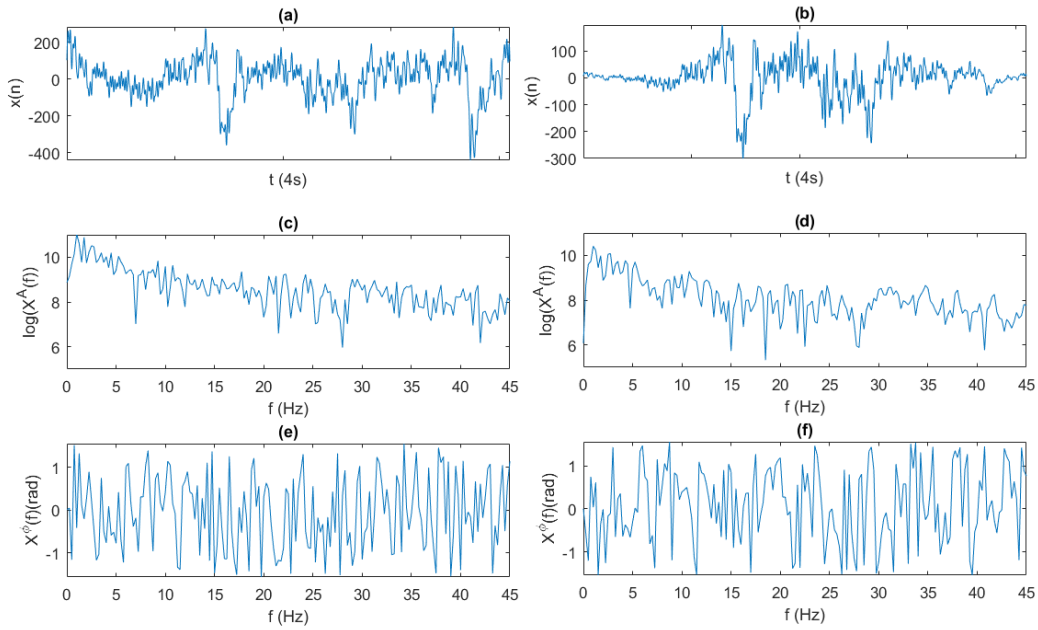

Figure 3.1: Comparison of nonparametric power spectrum estimation methods: (a) original 4–sec 0.5–45 Hz bandpass filtered EEG time series in the time domain, (b) the EEG signal tapered by a Hamming window, (c) classic magnitude plot in logarithmic–scale through DFT, (d) Hamming window modified magnitude plot in logarithmic–scale, (e) phase plot of the original signal, and (f) phase plot of the tapered signal.

Furthermore, statisticians, e.g., Bartlett and Welch, came up with the ideas of splitting–averaging and even overlapping to further reduce the power spectrum variance [95, 96]. Splitting the time–domain signal into segments reduces the number of sample points, and this decreases the resolution in the frequency representation.

3.4 Mutual Information in the Frequency Domain

Biological signals can be viewed as nonstationary stochastic time series [97, 98], however a short duration of the biological recordings can be considered as wide–sense–stationary (WSS) time series. Given two time series $x(n)$ and $y(n)$ with

spectral characteristics $X^A(f)$, $Y^A(f)$, $X^\phi(f)$ and $Y^\phi(f)$ (equations (2.2) and (2.3)), continuous MI in the frequency domain can be defined with respect to these spectral characteristics. For the case of magnitudes $X^A(f)$ and $Y^A(f)$, the MI is:

$$I_{XY}^{AA}(f) = \mathbf{E}\Big[\log \frac{p\big(X^A(f), Y^A(f)\big)}{p\big(X^A(f)\big)p\big(Y^A(f)\big)}\Big], \tag{3.14}$$

where $p\big(X^A(f), Y^A(f)\big)$, $p\big(X^A(f)\big)$ and $p\big(Y^A(f)\big)$ are the joint and marginal pdfs of $X^A(f)$ and $Y^A(f)$. Similarly, we can define MI between phases

$$I_{XY}^{\phi\phi}(f) = \mathbf{E}\Big[\log \frac{p\big(X^\phi(f), Y^\phi(f)\big)}{p\big(X^\phi(f)\big)p\big(Y^\phi(f)\big)}\Big] \tag{3.15}$$

and between magnitude and phase

$$I_{XY}^{A\phi}(f) = \mathbf{E}\Big[\log \frac{p\big(X^A(f), Y^\phi(f)\big)}{p\big(X^A(f)\big)p\big(Y^\phi(f)\big)}\Big]. \tag{3.16}$$

To estimate the pdf, we employ a segmentation and KDE approach. First, time series $x(n)$ is segmented into M non–overlapping sample series of length N; next, the individual mean is subtracted from each of the segments to obtain a zero–mean sample series $x_j(n), n = 1, 2, ..., N$ and $j = 1, 2, ..., M$ that is then multiplied by a Hamming window. Accordingly, magnitude and phase are estimated from each of the Hamming window tapered series $x'_j(n) = x_j(n)\omega_H(n)$; thus, per pair of time series $x'_j(n), y'_j(n)$, we acquire $X_j^A(f)$, $X_j^\phi(f)$, $Y_j^A(f)$, and $Y_j^\phi(f)$ in the frequency domain. These spectral characteristics from the sample series are then used in the density estimation. In the case of magnitude coupling in formula (3.14), a conventional planar kernel density estimation is implemented using Gaussian kernels with a diagonal bandwidth matrix to acquire $\hat{p}\big(X^A(f), Y^A(f)\big)$ from samples $X_j^A(f)$ and $Y_j^A(f)$. Because of the non–negativity of the magnitudes, a logarithmic transformation is used

prior to the kernel density estimation to compensate for the use of the unbounded Gaussian kernels [90]. We note that the MI values are invariant to strictly monotonic and differentiable transformation of the random variables ($X^A(f)$ and $Y^A(f)$), so this transformation does not affect the value of $I_{XY}^{AA}(f)$ [58, 56].

The phases $X^\phi(f)$ and $Y^\phi(f)$ are continuous circular variables due to their periodicity (i.e., the value $-\frac{\pi}{2}$ is equivalent to $\frac{\pi}{2}$), and they individually follow circular pdfs $p\big(X^\phi(f)\big)$ and $p\big(Y^\phi(f)\big)$, while they jointly follow a toroidal pdf $p\big(X^\phi(f), Y^\phi(f)\big)$ [94]. Circular and toroidal KDE with padding, as detailed in Section 3.2.2, are employed accordingly. For the joint density of magnitude and phase $p_{XY}\big(X^A(f), Y^\phi(f)\big)$, a combination of log–transform and circular padding on magnitude and phase respectively is used as explained in Section 3.2.3.

After obtaining the sample estimates of the pdfs $\hat{p}(\cdot)$, the MI values per frequency are estimated with the "resubstitution" method in Section 3.1. Therefore, for the case of magnitudes of $x(n)$ and $y(n)$ corresponding to the same frequency f, the dependency can be estimated as:

$$\hat{I}_{XY}^{AA}(f) = \frac{1}{M}\sum_{j=1}^{M} \log \frac{\hat{p}_{XY}\big(X_j^A(f), Y_j^A(f)\big)}{\hat{p}_X\big(X_j^A(f)\big)\hat{p}_Y\big(Y_j^A(f)\big)}. \tag{3.17}$$

Similarly, for phases or combined magnitude and phase, the MIs can be obtained by

$$\hat{I}_{XY}^{\phi\phi}(f) = \frac{1}{M}\sum_{j=1}^{M} \log \frac{\hat{p}_{XY}\big(X_j^\phi(f), Y_j^\phi(f)\big)}{\hat{p}_X\big(X_j^\phi(f)\big)\hat{p}_Y\big(Y_j^\phi(f)\big)} \tag{3.18}$$

$$\hat{I}_{XY}^{A\phi}(f) = \frac{1}{M}\sum_{j=1}^{M} \log \frac{\hat{p}_{XY}\big(X_j^A(f), Y_j^\phi(f)\big)}{\hat{p}_X\big(X_j^A(f)\big)\hat{p}_Y\big(Y_j^\phi(f)\big)} \tag{3.19}$$

3.5 Data and Materials

We employ simulated data to examine the capability of our approach in capturing general dependency relations between two time series. Thus, the models for the simulated data are nonlinear and, moreover, the strength of dependency between the time series is controllable through a coupling parameter. In following these criteria, three nonlinear chaotic systems are selected for study: the Lorenz system, a bidirectionally coupled Lorenz system and unidirectionally coupled Mackey–Glass equations. We additionally employ the developed method on a dataset of EEG recordings for the study of emotional response with respect to interactions in the brain.

3.5.1 Simulated Time Series

In this sub–section, we provide the equations for the nonlinear chaotic systems and sample time series in the time domain. We also provide the power spectral densities for the time series that we use to test our methodology. Chaotic systems often have broadband power spectra with superimposed peaks [99]. For the systems under consideration, we investigate how the major frequency components change with respect to increased coupling strength. Information derived from this investigation is employed to assist the interpretation of the dependency measures results in Section 4.1.

Data from Lorenz System

The Lorenz system in equation (3.20) is a deterministic chaotic system that models the forced dissipative hydrodynamic flow [100].

$$\begin{aligned} \dot{x} &= 10(y - x) \\ \dot{y} &= x(28 - z) - y \\ \dot{z} &= xy - \frac{8}{3}z. \end{aligned} \tag{3.20}$$

Sun et al. [101] reported a "primary frequency" only observable in the z variable of the system at 1.3 Hz. Although the dynamic system involves all three variables simultaneously, the magnitude spectrum of x or y does not show this frequency explicitly. In addition, a secondary frequency is also observed through the power spectrum of the z variable around 1.5 Hz that holds a lower peak [102]. For this frequency, the x variable shows a notch behavior (see Figure 3.2).

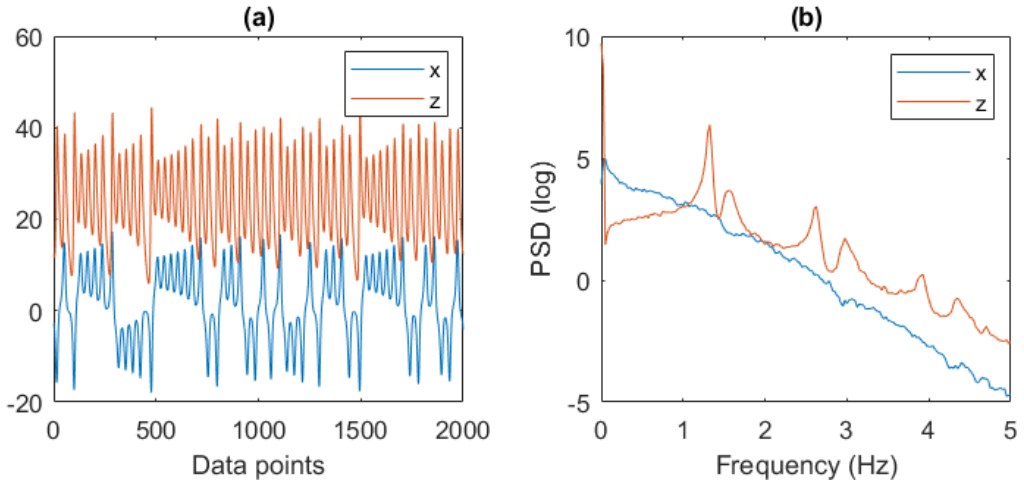

Figure 3.2: (a) $2,000$–length realization of x and z variables from the Lorenz system (equation (3.20)) plotted in the time domain and (b) their log–magnitude spectra through Welch's method.

Data from Bidirectionally Coupled Lorenz System

A bidirectionally coupled Lorenz system (equations (3.21)) was derived from originally coupled Lorenz systems to study measures of synchronization in coupled model systems [103]:

$$
\begin{aligned}
\dot{x_1} &= 10(y_1 - x_1) \\
\dot{y_1} &= x_1(28 - z_1) - y_1 \\
\dot{z_1} &= x_1 y_1 - \frac{8}{3} z_1 + c(z_2 - z_1) \\
\dot{x_2} &= 10(y_2 - x_2) \\
\dot{y_2} &= x_2(48 - z_2) - y_2 \\
\dot{z_2} &= x_2 y_2 - \frac{8}{3} z_2 + c(z_1 - z_2),
\end{aligned}
\tag{3.21}
$$

where the coupling strength c is varied from 0 to 2 in steps of 0.1 corresponding to the system transitioning from the non–coupled state to a generalized synchronization state. Spectrum plots of z_1 and z_2 for the non–coupled ($c = 0$) and coupled cases ($c = 0.3$, 1.0 and 2.0) are shown in Figure 3.3. The magnitude spectrum of the uncoupled system (in panel (a)) provides the primary components of the two sub–systems ((1) and (2)) at 1.3 and 1.8 Hz respectively. Panels (b)–(d) show that as the coupling strength increases, for sub–system 1 the 1.3 Hz component is shortened, while the 1.8 Hz peak gradually increases and aligns with the same peak of sub–system 2, eventually both sub–systems form a bump at 1.8 Hz.

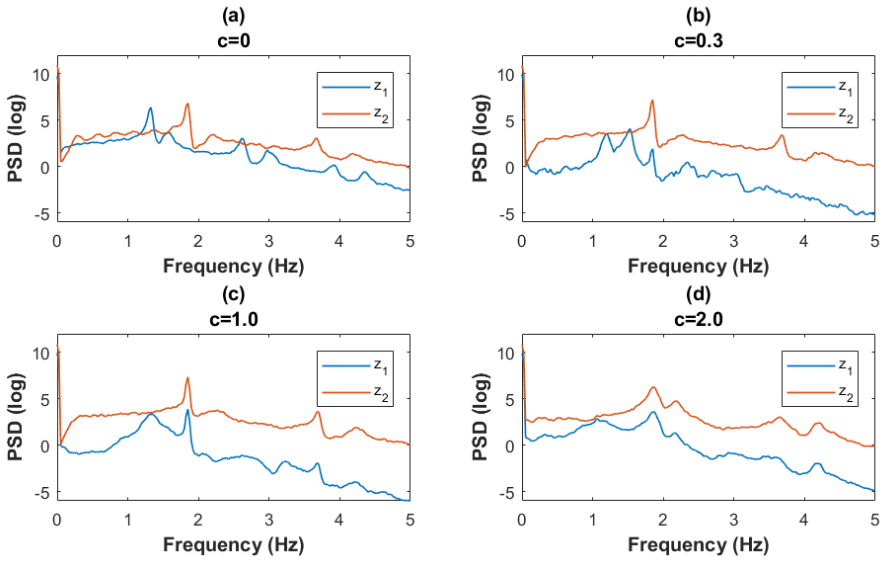

Figure 3.3: Log–magnitude spectra plots of the z_1 and z_2 variables from bidirectionally coupled Lorenz systems (equations (3.21)) with (a) $c = 0$, (b) $c = 0.3$ (c) $c = 1.0$ and (d) $c = 2.0$ through Welch's method.

Data from Unidirectionally Coupled Macky–Glass Equations

The unidirectionally coupled Mackey–Glass system (equations (3.22)) [104, 105] is based on a first–order nonlinear differential–delay equation describing physiological control systems for "normal and pathological function" [106].

$$\begin{aligned} \dot{x}(t) &= 0.2\frac{x(t-\tau_1)}{1+x(t-\tau_1)^{10}} - 0.1x(t) \\ \dot{y}(t) &= 0.205\frac{y(t-\tau_2)}{1+y(t-\tau_2)^{10}} - 0.1y(t) + c\frac{x(t-\tau_1)}{1+x(t-\tau_1)^{10}} \end{aligned} \tag{3.22}$$

where parameters τ_1 and τ_2 are 17 or 100, and the coupling strength c varies from 0 to 0.5 with step size 0.05.

When $\tau_1 = \tau_2 = 17$, uncoupled sample time series and magnitude spectra of x and y for $c = 0$, $c = 0.2$ and $c = 0.4$ are shown in Figure 3.4. Although x and y are

nearly identical in equations (3.22) when there is no coupling, their time domain plots seem in similar patterns (panel (a)), but the magnitude spectra in panel (b) do not superimpose each other. We can clearly observe peaks at 0.02 Hz and its harmonics appearing in both signals, and as the coupling strength increases the height of the peaks increases in panels (c) and (d).

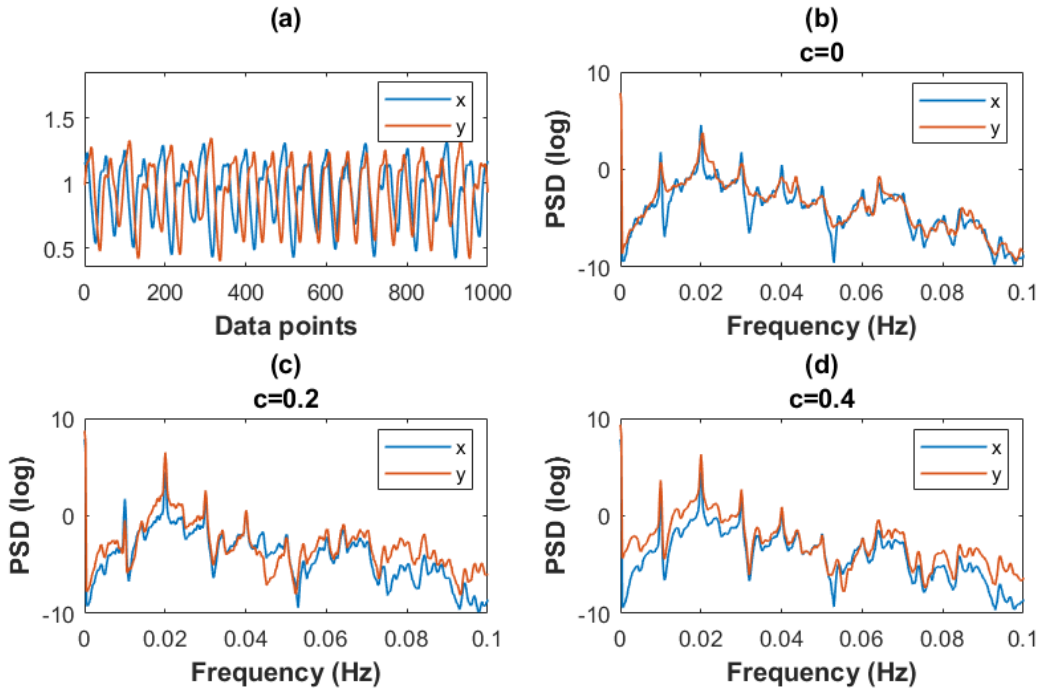

Figure 3.4: (a) Sample series plot of x and y from the uncoupled Mackey–Glass equations (3.22) ($c = 0$) $\tau_1 = \tau_2 = 17$, (b) their log–magnitude spectra plots, (c) log–magnitude spectra with coupling strength $c = 0.2$ and (d) with coupling strength $c = 0.4$.

For $\tau_1 = 17$ and $\tau_2 = 100$, uncoupled sample time series and magnitude spectra of x and y for $c = 0$, $c = 0.2$ and $c = 0.4$ are shown in Figure 3.5. Although both the x and y series fluctuate rapidly in the time domain (panel (a)), the spectrum of x contains a major component at 0.02 Hz and its harmonic frequencies while the y

variable exhibits cyclical "bumps" under a gradually dropping trend (panel (b)). As the coupling strength increases (panels (c) and (d)), the cyclical aspect in y is blurred and transformed to align with the x variable's profile.

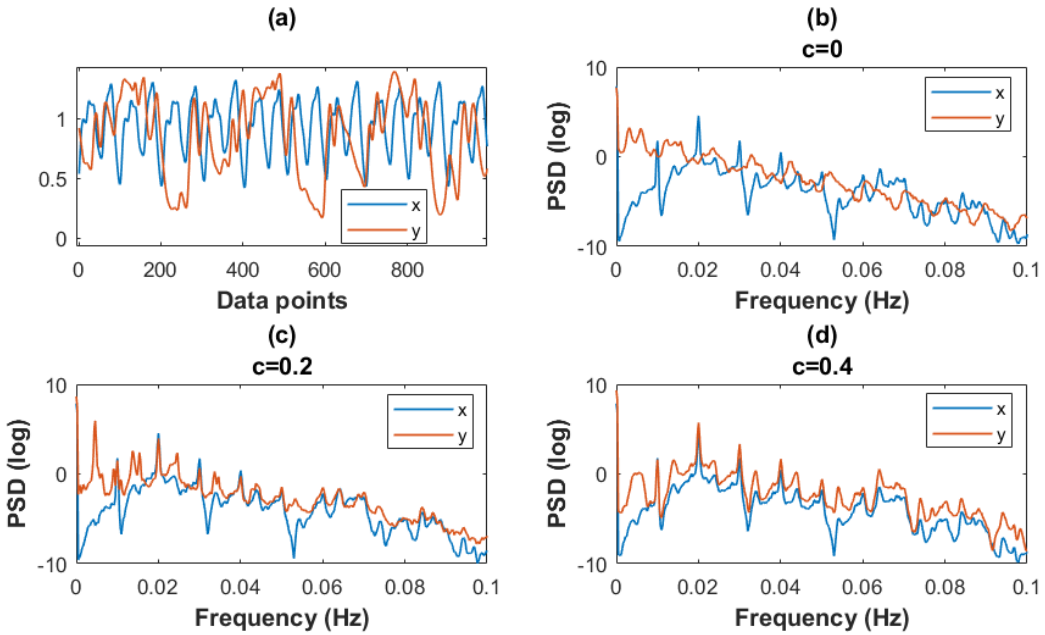

Figure 3.5: (a) Sample series plot of x and y from the uncoupled Mackey–Glass equations (3.22) ($c = 0$) $\tau_1 = 17$ and $\tau_2 = 100$, (b) their log–magnitude spectra plots, (c) log–magnitude spectra with coupling strength $c = 0.2$ and (d) with coupling strength $c = 0.4$.

The reverse direction coupling case ($\tau_1 = 100$, $\tau_2 = 17$) is shown in Figure 3.6. Panels (a) and (b) display the uncoupled signals in time and magnitude domain, so these two subplots are in the same pattern but in reverse color representation with Figure 3.5 panels (a) and (b). However, the passive subsystem contains the 0.02 Hz component with the new configuration, so the spectrum of y contains a major component at 0.02 Hz and its harmonics, while the x variable exhibits a cyclical

pattern (panel (b)). As the coupling strength increases, the profile of the passive subsystem is reshaped and aligned with the x variable's profile (panels (c) and (d)).

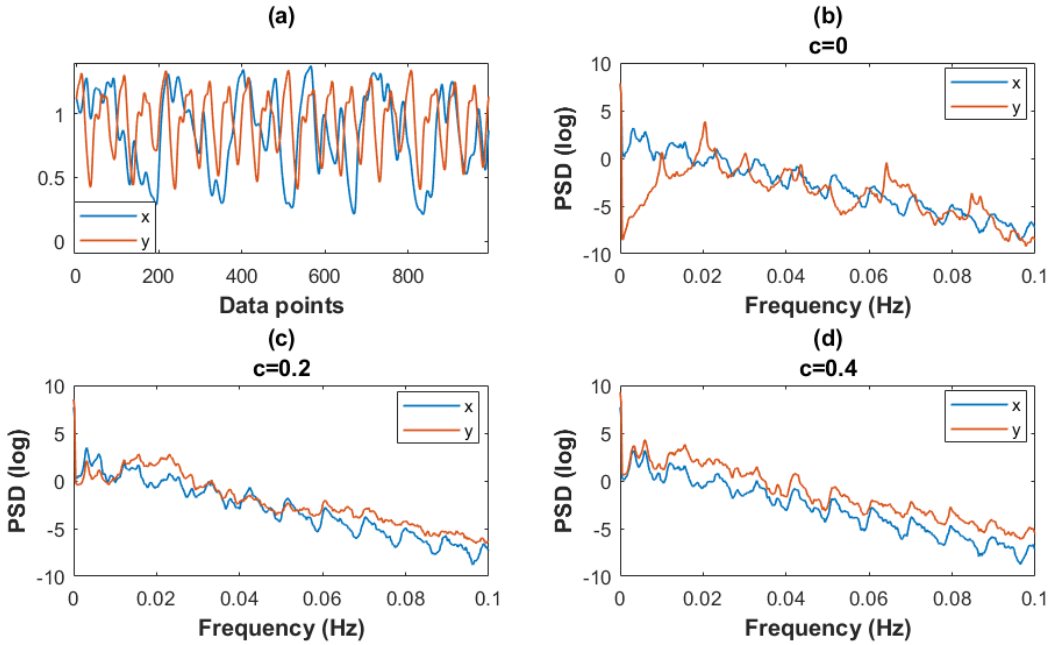

Figure 3.6: (a) Sample series plot of x and y from the uncoupled Mackey–Glass equations (3.22) ($c = 0$) $\tau_1 = 100$ and $\tau_2 = 17$, (b) their log–magnitude spectra plots, (c) log–magnitude spectra with coupling strength $c = 0.2$ and (d) with coupling strength $c = 0.4$.

The last system is when $\tau_1 = \tau_2 = 100$. Uncoupled sample time series and magnitude spectra of x and y for $c = 0$, $c = 0.2$ and $c = 0.4$ are shown in Figure 3.7. Although the time domain sample series are different between x and y in panel (a), their magnitude spectra are almost identical holding a series of gradual decreasing bumps (panel (b)). Per this uni–directionally coupled system, as the coupling strength grows in this system, the driving signal remains the same, while y from the passive system changes in shape and slowly boosts as higher arches per bump cycle (panels (c) and (d)).

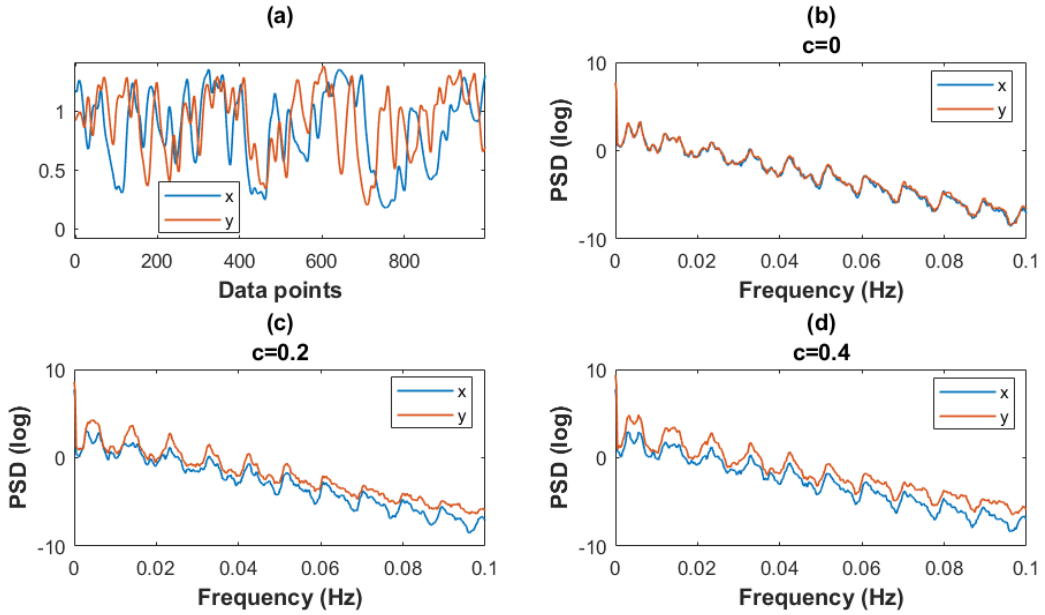

Figure 3.7: (a) Sample series plot of x and y from the uncoupled Mackey–Glass equations (3.22) ($c = 0$) $\tau_1 = 100$ and $\tau_2 = 100$, (b) their log–magnitude spectra plots, (c) log–magnitude spectra with coupling strength $c = 0.2$ and (d) with coupling strength $c = 0.4$.

In the simulations, time series of length $400,000$ for the first two systems (Lorenz) were generated with an integration step of 0.02. The $400,000$ observations were further segmented into $M = 200$ sample series containing $N = 2,000$ observations in each segment for the estimation of MIs. Time series from Mackey–Glass system were generated with an integration step of 1 and segmented into $M = 200$ sample series with $N = 1,000$ observations each. For all three coupled nonlinear system simulations, 100 replicates of time series were generated with random initial conditions and the average MIs are presented.

3.5.2 Emotional Behavior Electrophysiological Data

The DEAP database is a publicly available dataset for the study of human affective states [5] under Russell's emotional state model [4]. This response to emotional stimuli experiment was designed to provide 32 participants with the same 40 trials of one–minute–long music video clips, to record their instantaneous physiological signals (EEG and peripheral nervous system signals) as well as frontal face video, and to collect their self–assessment rating scores per trial. Among the 40 channels of physiological signals, 32 channels are EEG recordings and they were collected under a modified 10—10 montage shown in Figure 3.8. Per this EEG montage arrangement, the nine electrodes covering the frontal lobe from front to central part are Fp1, Fp2, AF3, AF4, F3, F4, F7, F8 and Fz; the three electrodes covering the central part of brain are C3, C4, and Cz, and the neighbor electrodes to the frontal are FC1, FC2, FC5, and FC6, and to the parietal lobe are CP1, CP2, CP5, and CP6. The left and right temporal lobes are represented by T7 and T8, respectively. The parietal lobe is covered mainly by five electrodes: P3, P4, P7, P9 and Pz, while the occipital lobe has O1, O2 and Oz; however, these two lobes share two electrodes, PO3 and PO4, along their boundary. The music video clips were selected to evenly represent low/high values in the valence–arousal space [5] and with the "maximum emotional content" [5]. The partial dataset employed for our analysis includes EEG recordings for the last 30 seconds of each trial and subjective ratings on the two model dimensions (i.e., valence and arousal). The 32–channel EEG recordings underwent integrated preprocessing, including EOG artifacts removal, common reference averaging, 4–45Hz band–pass filtering, and down–sampling to 128Hz.

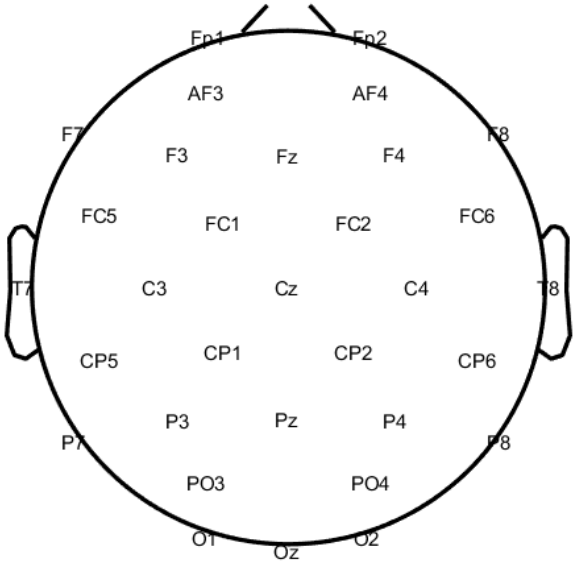

Figure 3.8: Top view of the modified 10–10 montage that DEAP dataset applied [5].

CHAPTER 4

RESULTS

The methodology described in Chapter 3 is tested on simulated data and real–world biological signals using in–house built algorithms with Python programming language (*Python 2.7.12*) and its scientific computing modules (i.e., *Numpy 0.13.0* and *Scipy 0.19.0*), as well as Matlab v*R2017a* with *academic license*.

4.1 Results on Artificial Data

4.1.1 Lorenz

The MI in the frequency domain measures (equations (3.17)–(3.19)) along with the conventional measure of MSC from equation (2.10) for x and z variables of the Lorenz system equations (3.20) were estimated. For the estimation of coherence, Welch's method was used with a Hamming window of length $N = 2,000$ and without overlapping, for consistency with the MI estimation procedures. The results are shown in Figures 4.1 and 4.2. C_{XZ} and I_{XZ}^{AA} (Figure 4.1, panels (a) and (b) respectively), except for the close to 0 Hz frequency component, both show a lower peak at 1.3 Hz and relatively higher second peak at 1.5 Hz. However, C_{XZ} values exhibit high variability at other frequencies while I_{XZ}^{AA} values remain consistently smaller for frequencies different from 0 Hz, the primary frequency at 1.3 Hz and the secondary frequency at 1.5 Hz of the system. Additionally, the overall range of C_{XZ} values is close to 0

indicating that coherence cannot adequately capture the nonlinear interaction between the two variables.

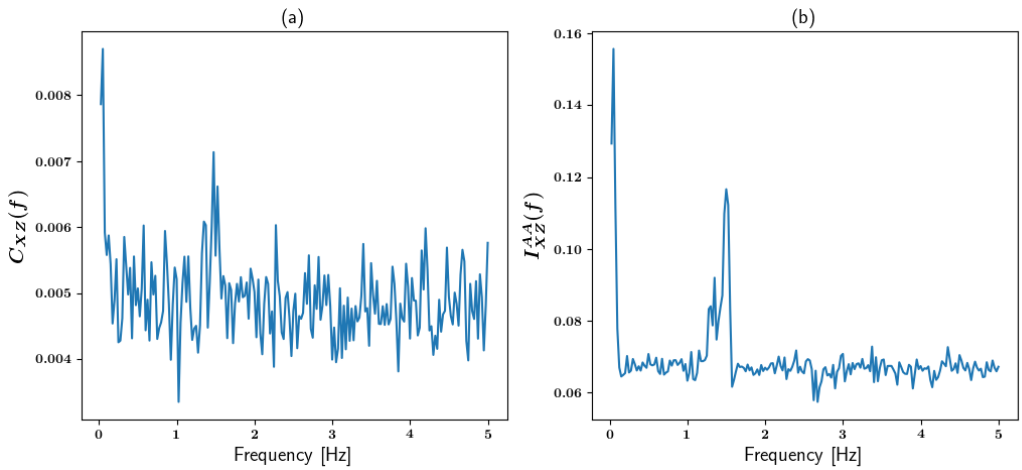

Figure 4.1: (a) MSC plot and (b) MI of magnitudes plot for x and z variables.

The other three MI measures are shown in Figure 4.2. Panel 4.2 (a) presents the dependency between phases of the x and z variables ($I^{\phi\phi}_{XZ}$) and it shows a clear peak at 1.3 Hz, which is the primary frequency of the system, along with a secondary peak at 1.5 Hz. This is the opposite of what was observed for the MI between magnitudes (Figure 4.1 (b)). Panels 4.2 (b) and (c) show the magnitude–phase interactions: $I^{A\phi}_{XZ}$ exhibits no clear peak at the primary or secondary frequencies (or any other frequency), while $I^{\phi A}_{XZ}$ has a single dominant peak at 1.3 Hz. This implies that the phase of the x variable of the Lorenz system interacts with z in a modulatory fashion to produce the 1.3 Hz activity, while the 1.5 Hz activity involves x and z without a similar feature. We note that all four MI measures capture and showcase different and distinct aspects of the interactions in the system.

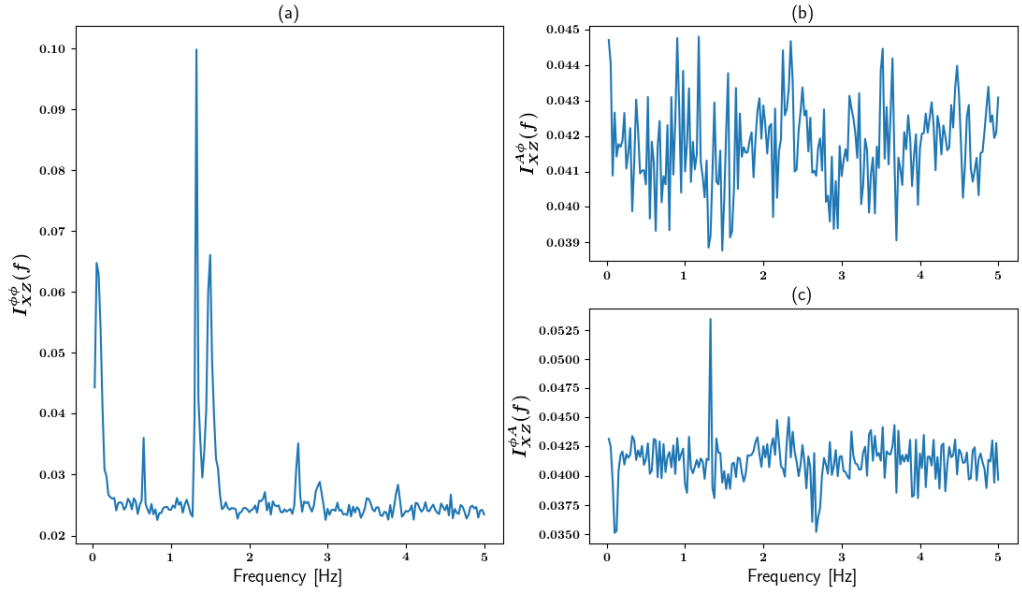

Figure 4.2: MI of (a) phases, (b) magnitude–phase and (c) phase–magnitude plots for x and z variables.

4.1.2 Bidirectionally coupled Lorenz

The z_1 and z_2 variables from the bidirectionally coupled Lorenz systems for a range of values of the coupling parameter were examined by means of MSC and the four MI measures and plotted in Figure 4.3. Panels (a)–(d) present pseudocolor intensity plots of the MI measure for the different spectral characteristics under the same scale, while panel (e) presents the MSC measure. For all plots the x–axis is the frequency, the y–axis is the coupling strength and the colors represent the value of the measure (warm colors corresponding to high values and cold colors to low values). We observe that $I^{AA}_{Z_1Z_2}$ and $I^{\phi\phi}_{Z_1Z_2}$ both exhibit high values starting from $c = 0.3$ at 1.8 Hz (the primary frequency of the second sub–system), with $I^{AA}_{Z_1Z_2}$ taking slightly higher values than $I^{\phi\phi}_{Z_1Z_2}$. Two clusters of relatively high values (approximately half of the

maximum values) are seen in the frequency ranges 0.7 to 1.5 (a range that includes the primary frequency of the first sub–system), and 2.0 to 2.3 Hz starting at $c = 0.3$ and fading away after $c = 1.2$ and $c = 0.6$ respectively. The two magnitude–phase measures ($I^{A\phi}_{Z_1Z_2}$ and $I^{\phi A}_{Z_1Z_2}$) exhibit extremely low values for all coupling parameters and all frequencies. Compared with $I^{AA}_{Z_1Z_2}$ and $I^{\phi\phi}_{Z_1Z_2}$, $C_{Z_1Z_2}$ exhibits its maximum values along the 1.8 Hz frequency region, and the two clusters are slightly shifted to higher coupling strengths with high values (close to the maximum of 1). Overall, $I^{AA}_{Z_1Z_2}$ and $I^{\phi\phi}_{Z_1Z_2}$ clearly detect the interaction between the two systems in the Z dimension and the frequency of this interaction occurs at 1.8 Hz, while MSC provides high values for a large range of frequencies, indicative of its inability to accurately identify the interactions as the nonlinear coupling strength increases.

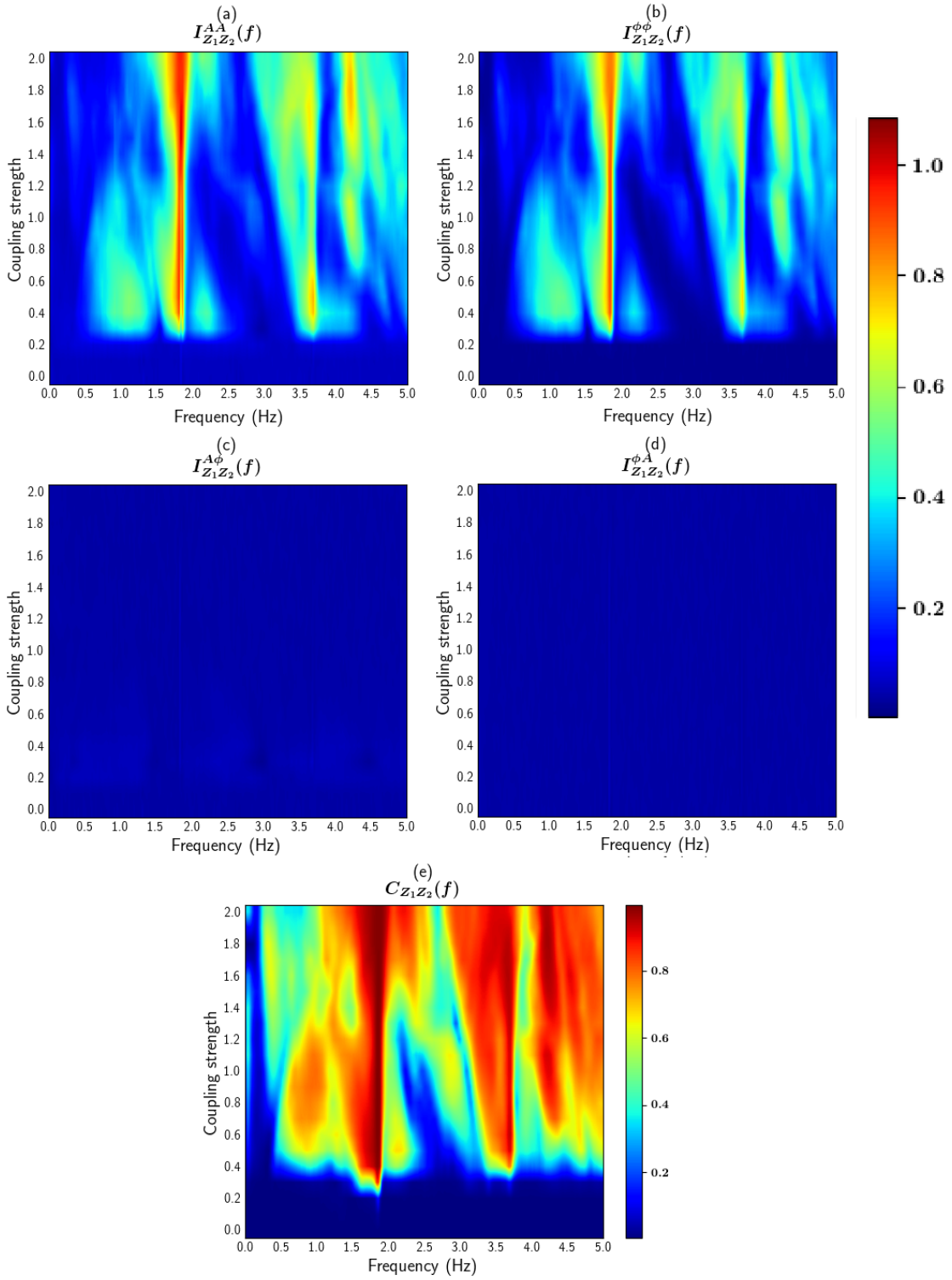

Figure 4.3: Comparison of measures from z_1 and z_2 of the bidirectionally coupled Lorenz system: (a) MI of magnitudes, (b) of phases, (c) of magnitude–phase, (d) of phase–magnitude and (e) MSC.

Figure 4.4 presents selected cases of $C_{Z_1Z_2}$, $I^{AA}_{Z_1Z_2}$ and $I^{\phi\phi}_{Z_1Z_2}$ for specific coupling strengths ($c = 0.3$, $c = 1.0$ and $c = 2.0$). For the case of small coupling strength (panels (a)–(c)) $C_{Z_1Z_2}$ only captures the interaction at 1.5 and 1.8 Hz taking values close to the maximum, while $I^{AA}_{Z_1Z_2}$ and $I^{\phi\phi}_{Z_1Z_2}$ also capture the interaction below 1.5 Hz and above 2.0 Hz. As the coupling strength increases to $c = 1.0$ (panels (d)–(f)) and $c = 2.0$ (panels (g)–(i)), $C_{Z_1Z_2}$ takes high values for most of the frequencies, while $I^{AA}_{Z_1Z_2}$ and $I^{\phi\phi}_{Z_1Z_2}$ give prominence to the 1.8 Hz frequency components, and the 0.7 to 1.5 Hz "bump" gradually vanishes.

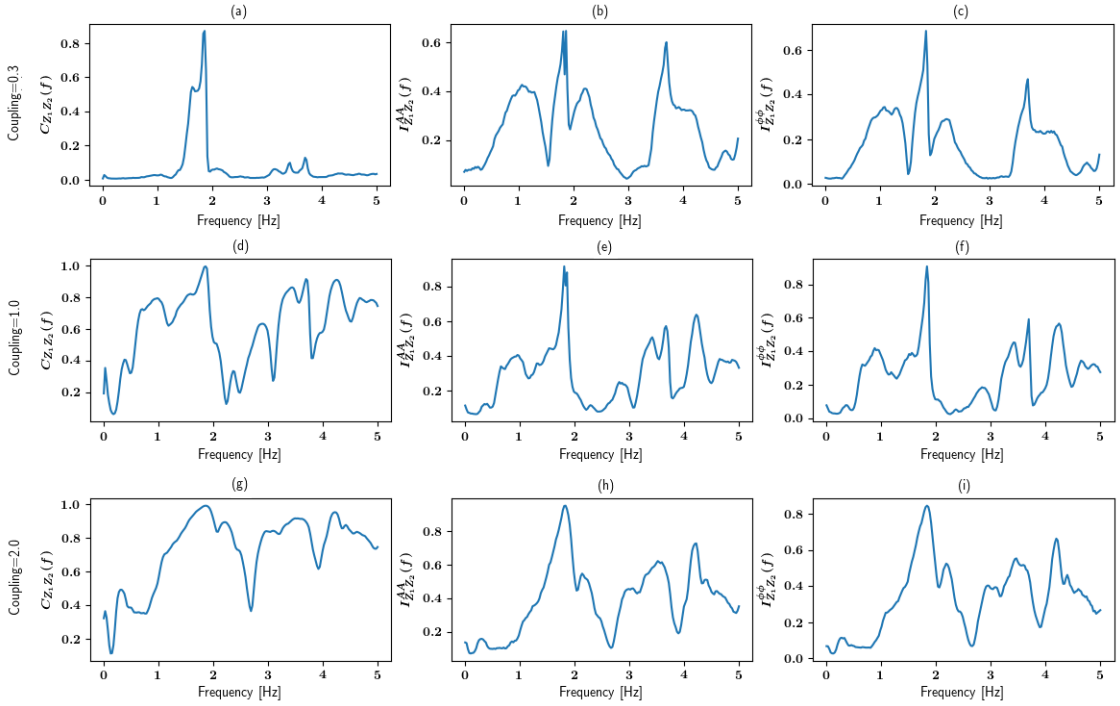

Figure 4.4: MSC (left column), MI of magnitudes (middle column) and MI of phases (right column) plots for z_1 and z_2 variables from the bidirectionally coupled Lorenz system with coupling strength $c = 0.3$ in (a)–(c), $c = 1.0$ in (d)–(f) and $c = 2.0$ in (g)–(i).

4.1.3 Unidirectionally coupled Mackey–Glass

Figures 4.5, 4.7 and 4.9, and 4.11 present the results of the analysis of the four cases of the coupled Mackey–Glass equations. Measures $I_{XY}^{A\phi}$ and $I_{XY}^{\phi A}$ show extremely low values for all coupling parameters and all frequencies, similarly to the case of the bidirectional coupled Lorenz systems, so we omit presentation of results from them.

In the first case of x driving y with both sub–systems having the same parameter ($\tau_1 = \tau_2 = 17$) in Figure 4.5, I_{XY}^{AA} in panel (a) captures the coupling beyond $c = 0.05$ for most of the frequency components, and as the coupling increases most of the frequencies exhibit gradual increases in value as well. I_{XY}^{AA} around 0.067 Hz is slightly more dominant across all frequencies. However, the frequency band 0.05 Hz to 0.06 Hz has a major drop between coupling strength $c = 0.25$ and 0.45. $I_{XY}^{\phi\phi}$ in panel (b) gives values lower than I_{XY}^{AA} for the same frequencies. Additionally, it also shows coupling at 0.01 Hz and 0.02 Hz when $c = 0.05$ (the smallest coupling strength). C_{XY} in panel (c) exhibits its maximum value of 1 for almost all frequencies.

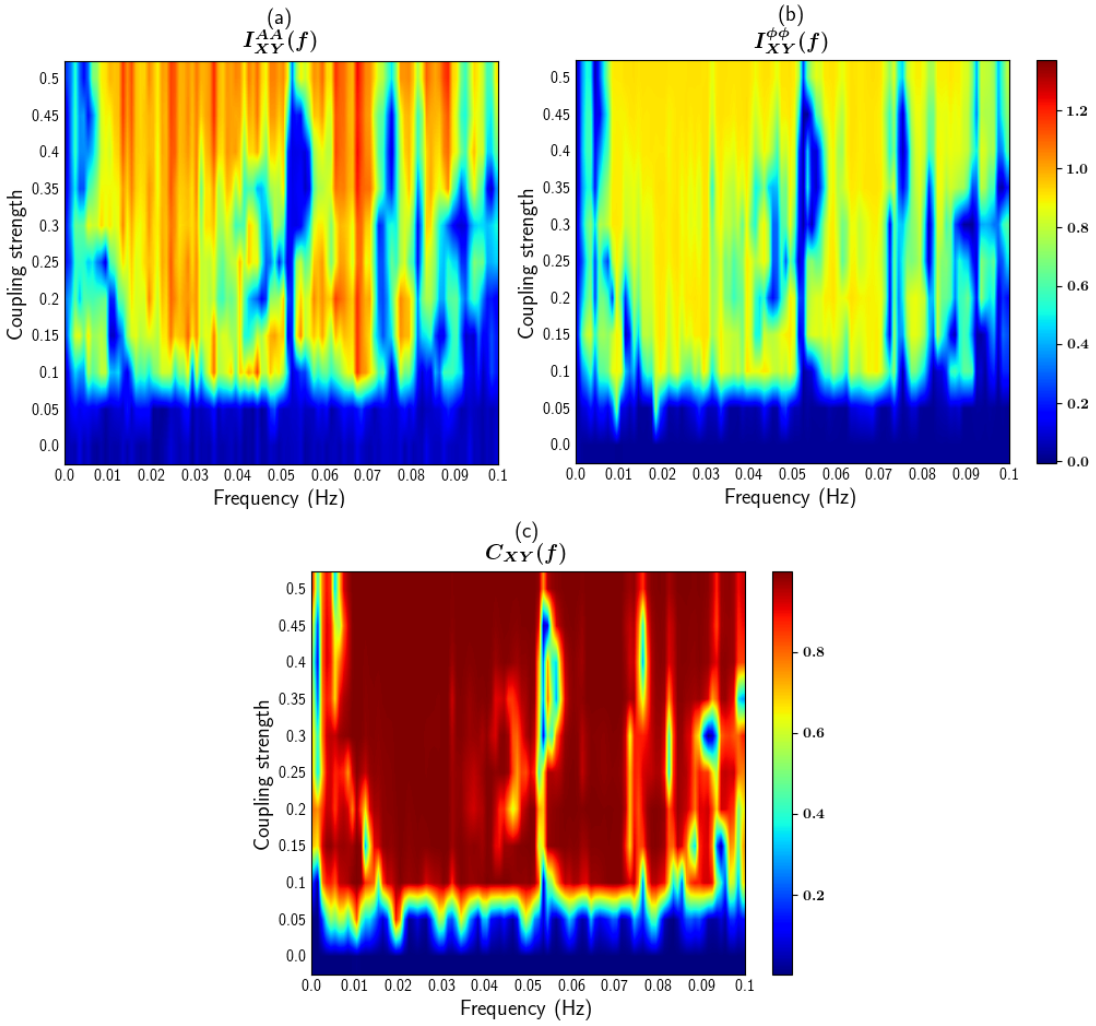

Figure 4.5: Comparison of measures from x and y of the unidirectionally coupled Mackey–Glass equations (x with $\tau_1 = 17$ drives y with $\tau_2 = 17$): (a) MI of magnitudes, (b) MI of phases, and (c) MSC.

Figure 4.6 compares the three measures as functions of the coupling strength $c \in [0, 0.5]$ at 0.051 Hz and 0.067 Hz. Panels (a)–(c) showcase the C_{XY}, I_{XY}^{AA} and $I_{XY}^{\phi\phi}$ at 0.051 Hz: we observe C_{XY} quickly jumps to the maximum value after coupling is introduced ($c = 0.1$); while I_{XY}^{AA} and $I_{XY}^{\phi\phi}$ both exhibit local peaks at $c = 0.1$ and $c = 0.2$, then monotonically increase until the maximum value of coupling strength

($c = 0.5$). In the case of $f = 0.067$ Hz, all three measures behave similarly, with a major increase at $c = 0.1$ and remaining high afterward.

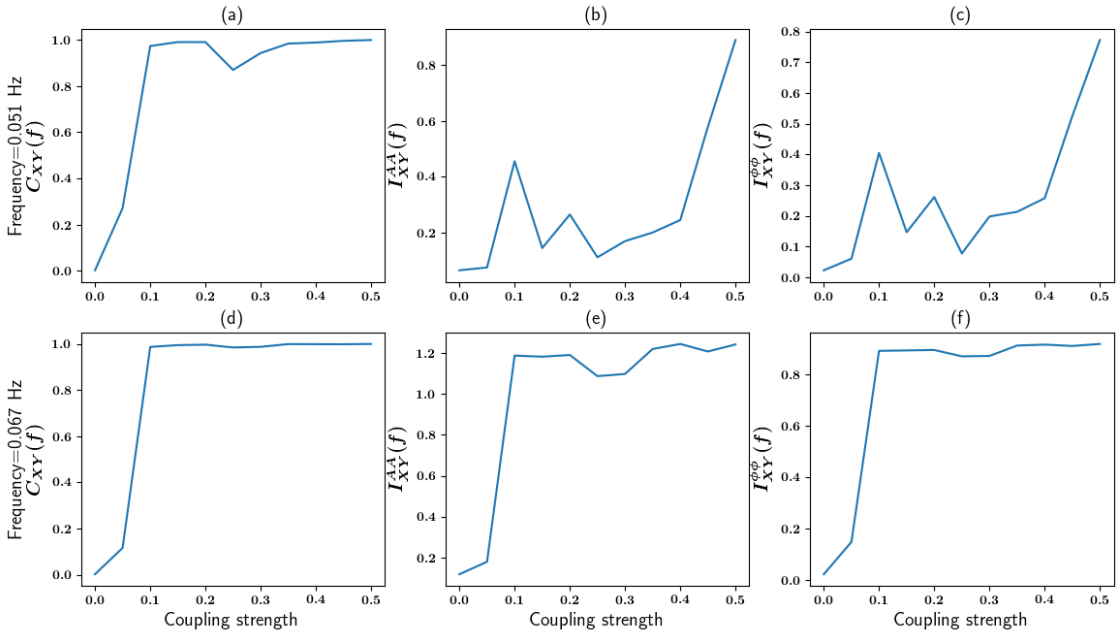

Figure 4.6: Comparison of MSC (left column), MI of magnitudes (middle column) and MI of phases (right column) between the unidirectionally coupled Mackey–Glass equations (x and y both with $\tau_1 = \tau_2 = 17$) as a function of coupling strength, for frequency $f = 0.051$ Hz in (a)–(c) and $f = 0.067$ Hz in (d)–(f).

In the case of x with $\tau_1 = 17$ driving y with $\tau_2 = 100$ in Figure 4.7, I^{AA}_{XY} in panel (a) exhibits a gradual increase at multiple frequencies with no discernible pattern as the coupling strength increases. The MI values spread over the whole frequency range as coupling increases. The main observation is the MI around 0.067 Hz that is slightly more dominant. $I^{\phi\phi}_{XY}$ in panel (b) behaves similarly but lacks the 0.067 Hz dominant values and takes high values at 0.02 Hz even for the smallest coupling value ($c = 0.05$). C_{XY} in panel (c) takes its maximum value for almost all frequencies after coupling $c = 0.3$ with no specific frequency exhibiting something of interest.

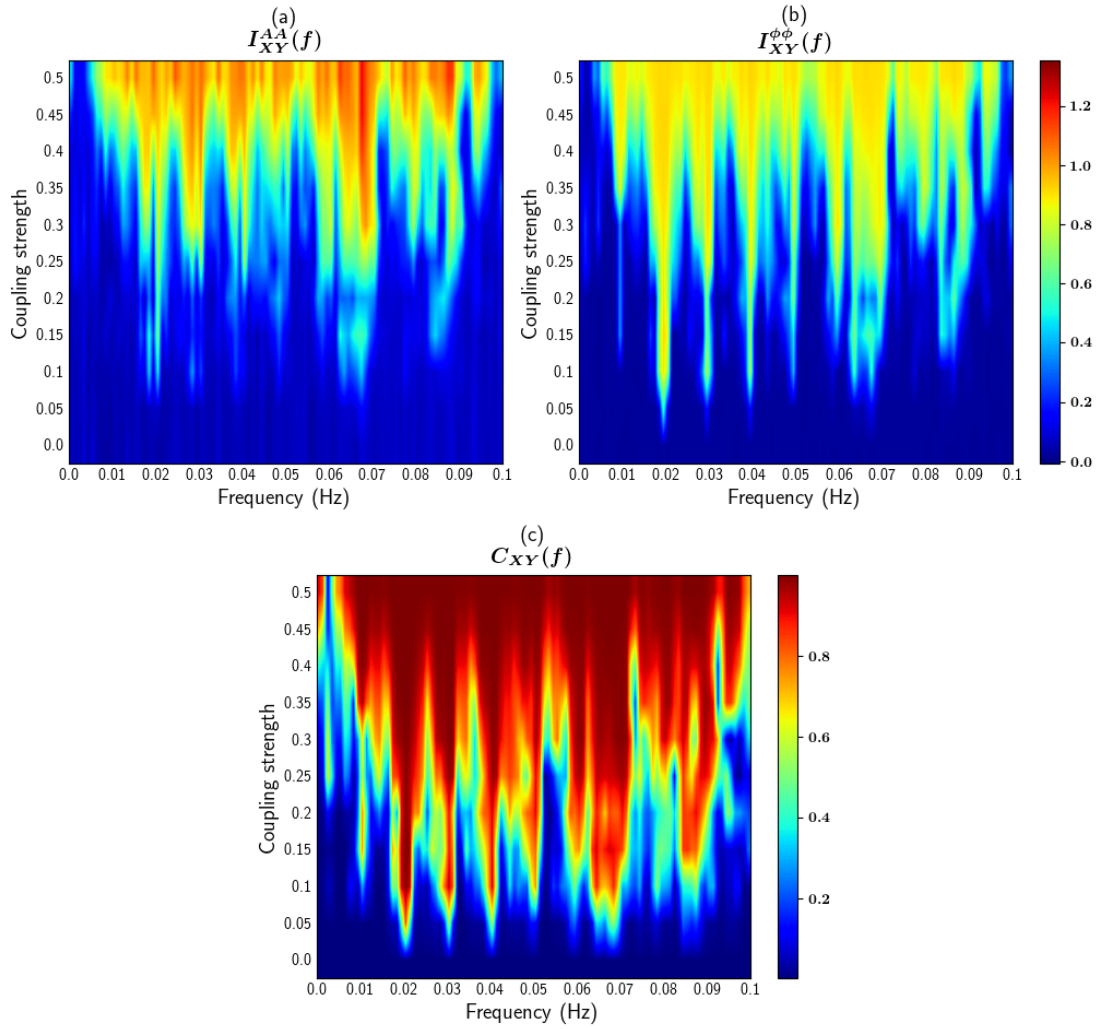

Figure 4.7: Comparison of measures from x and y of the unidirectionally coupled Mackey–Glass equations (x with $\tau_1 = 17$ drives y with $\tau_2 = 100$): (a) MI of magnitudes, (b) MI of phases, and (c) MSC.

Figure 4.8 shows the three measures for two selected frequencies, $f_1 = 0.02$ Hz and $f_2 = 0.067$ Hz. In the first case (top row), C_{XY} quickly jumps to its maximum value when $c = 0.05$ and retains the same value for increasing coupling strengths in panel (a), I^{AA}_{XY} shows a gradual rise as coupling strength increases in panel (b) and $I^{\phi\phi}_{XY}$ also exhibits a plateau–like shape after $c = 0.1$ in panel (c). In the second

case (bottom row), I_{XY}^{AA} and $I_{XY}^{\phi\phi}$ correctly identify the gradually increasing coupling between the x and y variables in panels (e) and (f).

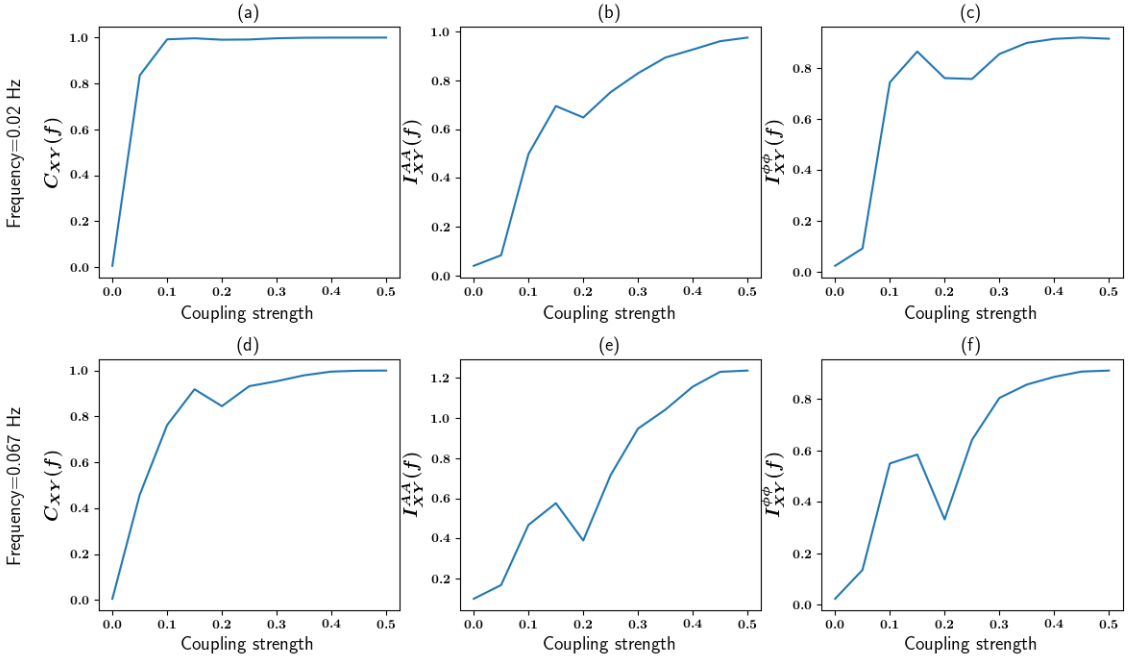

Figure 4.8: Comparison of MSC (left column), MI of magnitudes (middle column) and MI of phases (right column) between the unidirectionally coupled Mackey–Glass equations (x with $\tau_1 = 17$ drives y with $\tau_2 = 100$) as a function of coupling strength, for frequency $f = 0.02$ Hz in (a)–(c) and $f = 0.067$ Hz in (d)–(f).

The case of the passive subsystem specified by $\tau_2 = 17$ and the driving subsystem being with $\tau_2 = 100$, MI and coherence measures are displayed in Figure 4.9. I_{XY}^{AA} in panel (a) exhibits the same gradual increase at multiple frequencies as the coupling strength increases. The affected frequency components hold almost equal distances between them, and the lowest coupling parameters that causes measure increase at these frequencies show a linear increasing trend. The highest I_{XY}^{AA} appears around 0.006 Hz. Meanwhile, $I_{XY}^{\phi\phi}$ in panel (b) behaves similarly but all values are lower than the corresponding I_{XY}^{AA} values in panel (a). C_{XY} in panel (c) takes its

maximum value for quite a few frequencies after coupling $c = 0.3$ with no specific frequency exhibiting something of interest.

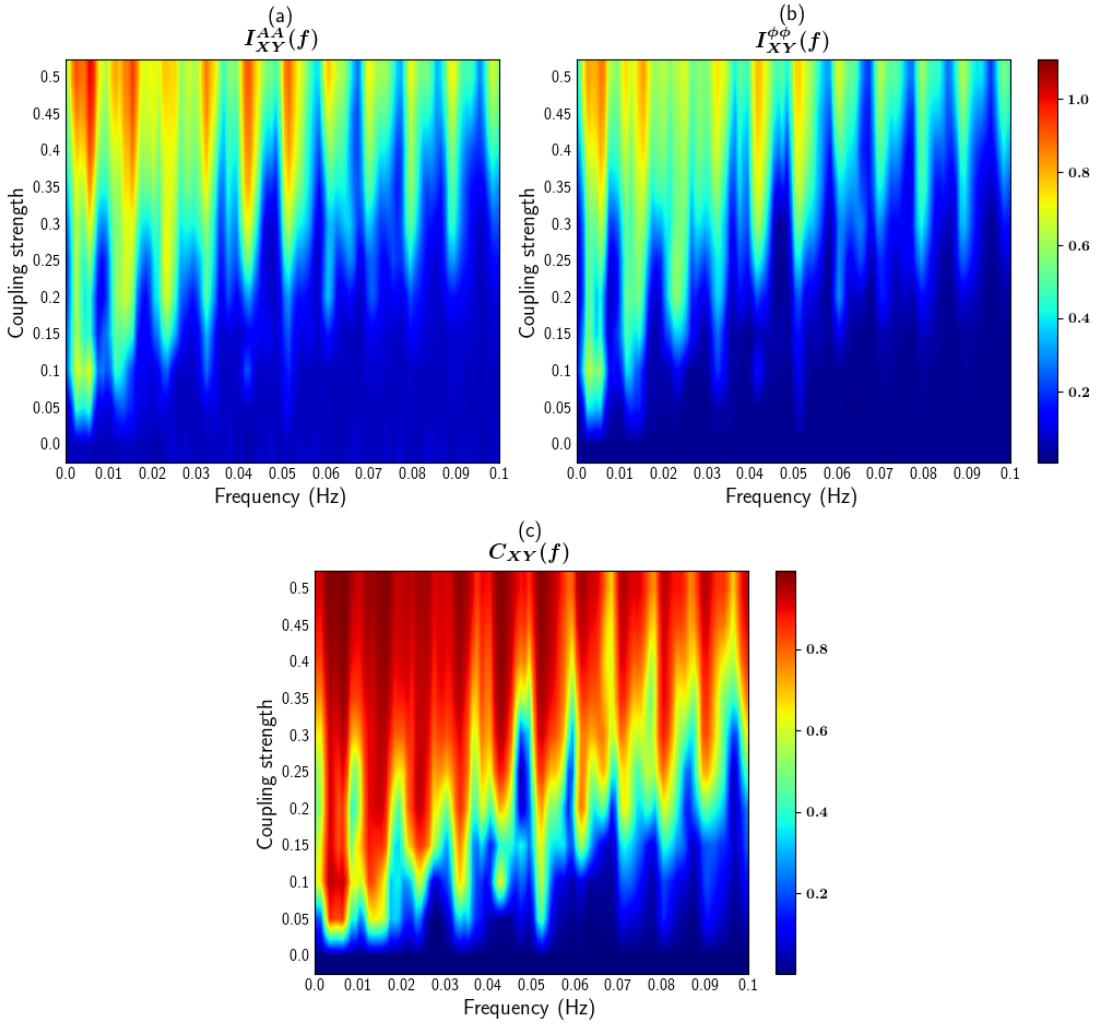

Figure 4.9: Comparison of measures from x and y of the unidirectionally coupled Mackey–Glass equations (x with $\tau_1 = 100$ drives y with $\tau_2 = 17$): (a) MI of magnitudes, (b) MI of phases, and (c) MSC.

For selected frequencies of 0.006 Hz and 0.052 Hz, the three measures are shown in Figure 4.10. Panels (a)–(c) show individual local peaks at $c = 0.1$, but C_{XY} has this peak value close to its maximum and remains high for the ensuing coupling

parameters, while I^{AA}_{XY} and $I^{\phi\phi}_{XY}$ display this peak with value no more than half of their maximum values at $c = 0.5$. The second case in panels (d)–(f) also shows the difference between MSC and MI measures, C_{XY} exhibits a concave shape while MI measures show a sigmoid shape (convex first and then concave).

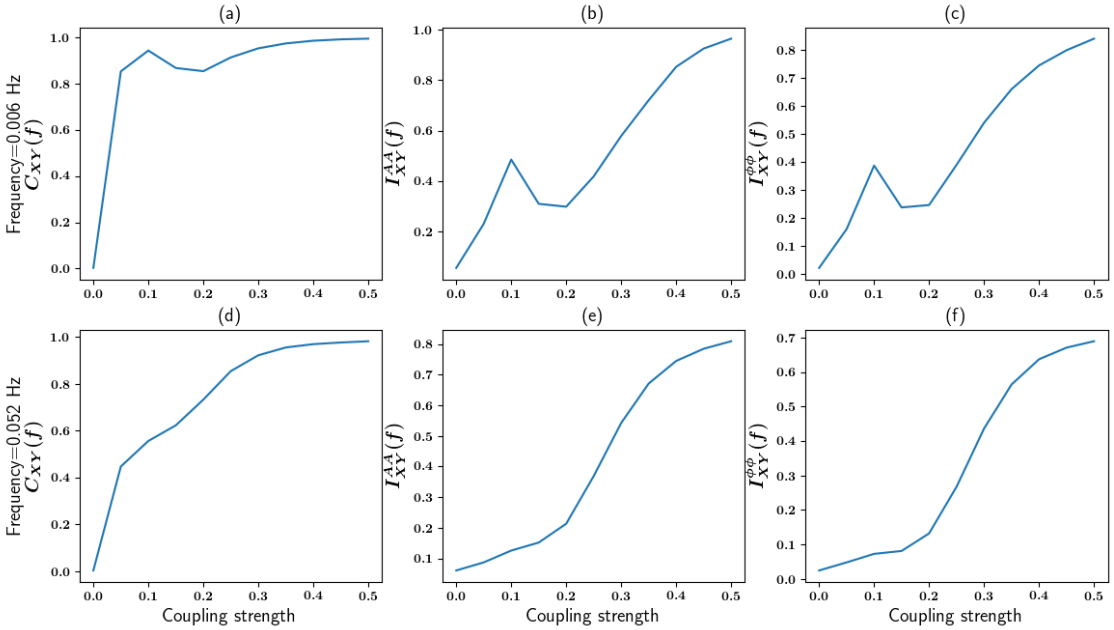

Figure 4.10: Comparison of MSC (left column), MI of magnitudes (middle column) and MI of phases (right column) between the unidirectionally coupled Mackey–Glass equations (x with $\tau_1 = 100$ drives y with $\tau_2 = 17$) as a function of coupling strength, for frequency $f = 0.006$ Hz in (a)–(c) and $f = 0.052$ Hz in (d)–(f).

When the passive subsystem and the driving subsystem are both specified with $\tau = 100$, the comparison of I^{AA}_{XY}, $I^{\phi\phi}_{XY}$ and C_{XY} are displayed in Figure 4.11. I^{AA}_{XY} in panel (a) exhibits the same gradual increase at multiple frequencies as the coupling strength increases. The affected frequency components hold almost equal distances between them, and the coupling across these frequencies seems to appear for the same coupling parameter $c = 0.2$. Regarding the intensity of I^{AA}_{XY}, high intensity tends

to appear in the lower frequencies (below 0.06 Hz). $I_{XY}^{\phi\phi}$ in panel (b) again exhibits similar behavior but measure values are lower than the corresponding I_{XY}^{AA} values in panel (a). C_{XY} in panel (c) takes its maximum value for the majority of the same frequencies as the MI measures after coupling $c = 0.2$, however the initiating coupling strength reduces to $c = 0.05$.

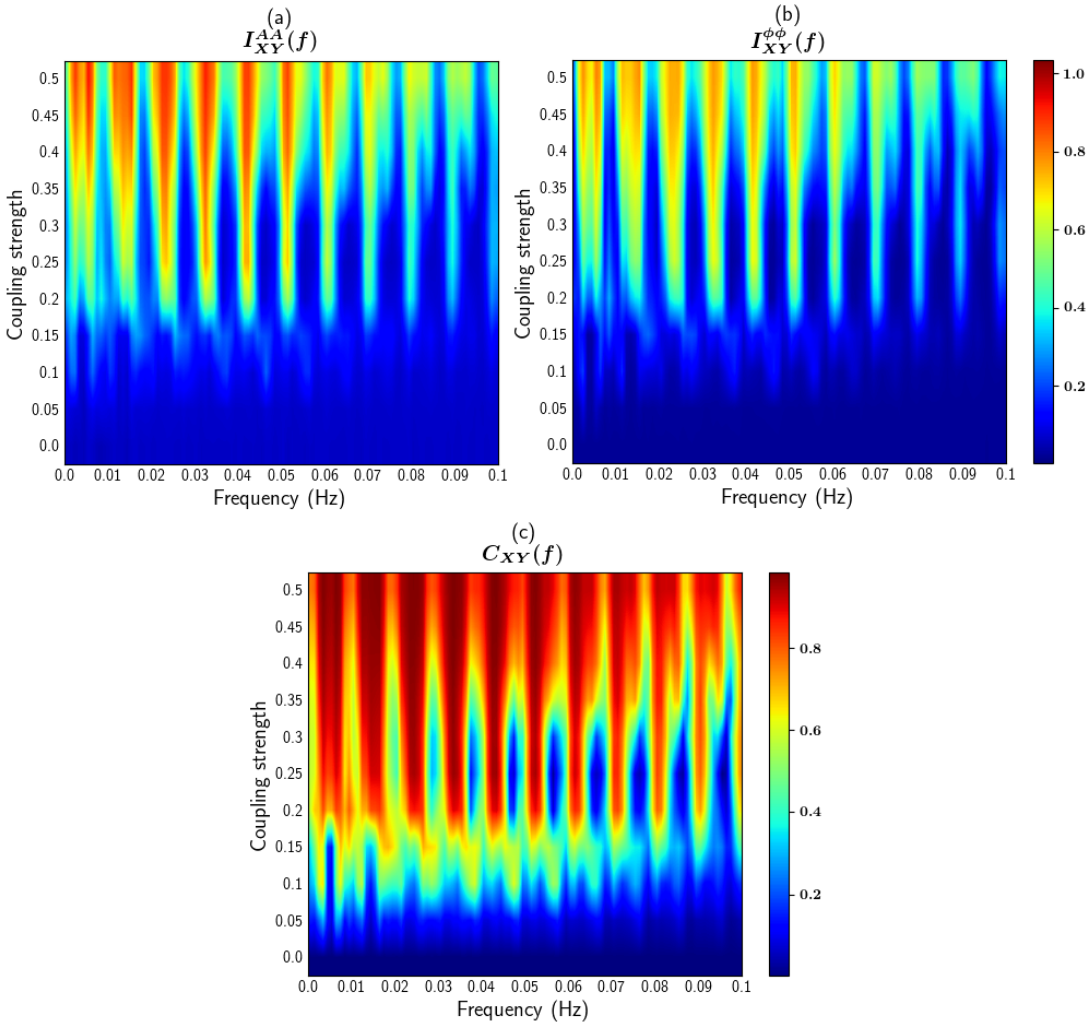

Figure 4.11: Comparison of measures from x and y of the unidirectionally coupled Mackey–Glass equations (x with $\tau_1 = 100$ drives y with $\tau_2 = 100$): (a) MI of magnitudes, (b) MI of phases, and (c) MSC.

Measure values for frequencies 0.006 Hz and 0.035 Hz are compared in Figure 4.12. In panel (a), C_{XY} exhibits monotonic increasing trend with plateau beyond $c = 0.3$. For the same data, I^{AA}_{XY} in panel (b) and $I^{\phi\phi}_{XY}$ in panel (c) increase almost linearly as coupling strength grows. In the second case ($f = 0.035$ Hz), I^{AA}_{XY} and $I^{\phi\phi}_{XY}$ in panels (e) and (f) again show individual peaks at $c = 0.15$, and after $c = 0.3$ linear increase, while the local peak for C_{XY} appears at $c = 0.3$, taking a value close to the maximum, and remaining relatively constant for the rest of the coupling strengths.

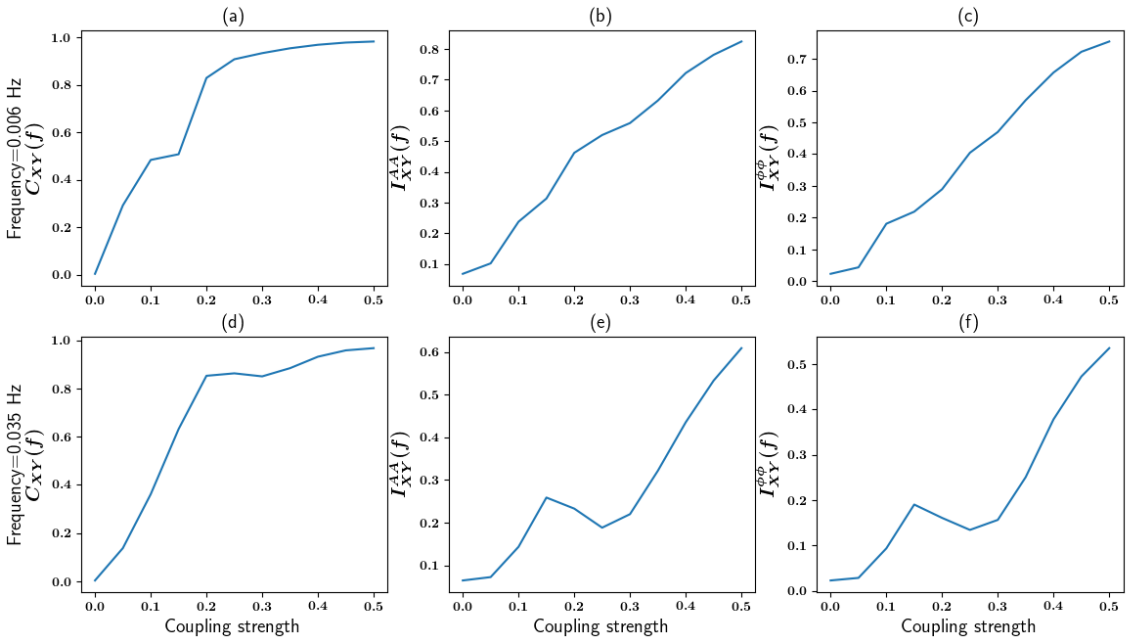

Figure 4.12: Comparison of MSC (left column), MI of magnitudes (middle column) and MI of phases (right column) between the unidirectionally coupled Mackey–Glass equations (x and y both with $\tau_1 = \tau_2 = 100$) as a function of coupling strength, for frequency $f = 0.006$ Hz in (a)–(c) and $f = 0.035$ Hz in (d)–(f).

4.2 Results on Real EEG Data

The EEG data from experimental trials of the DEAP database were divided into two groups per affective dimension (i.e., positive or negative valence, and high

and low arousal) by the median rating score per subject. This division resulted in $M = 633/629$ in number segments for valence and $M = 625/625$ for arousal. The EEG data from the second half duration of each trial (30 seconds) for all subjects and trials were used, in accordance to Koelstra et al. [5]. The frequency domain MI measures were estimated separately for positive/negative or high/low affective states and for every pair of channels (496 pairs in total).

For each 30 seconds segment and each EEG channel, a Hamming window was applied to the data and DFT was performed. Then the magnitude and phase per frequency were extracted. Finally, the MI measures in the frequency domain were estimated from the M in number segments that correspondent to each state. Figure 4.13 presents $I_{XY}^{AA}(f)$ and $I_{XY}^{\phi\phi}(f)$ between two selected EEG channel pairs, Oz–FC6 and P3–F8, for positive and negative states of valence. In panel (a), we observe a notable difference between the state of positive valence (blue line) and that of negative (orange line) for the EEG channel pair Oz–FC6. This difference appears at higher frequencies and it is more prominent for $I_{XY}^{AA}(f)$ than $I_{XY}^{\phi\phi}(f)$. For the second EEG channel pair, P3–F8, shown in panel (c) and (d), no such difference is observed.

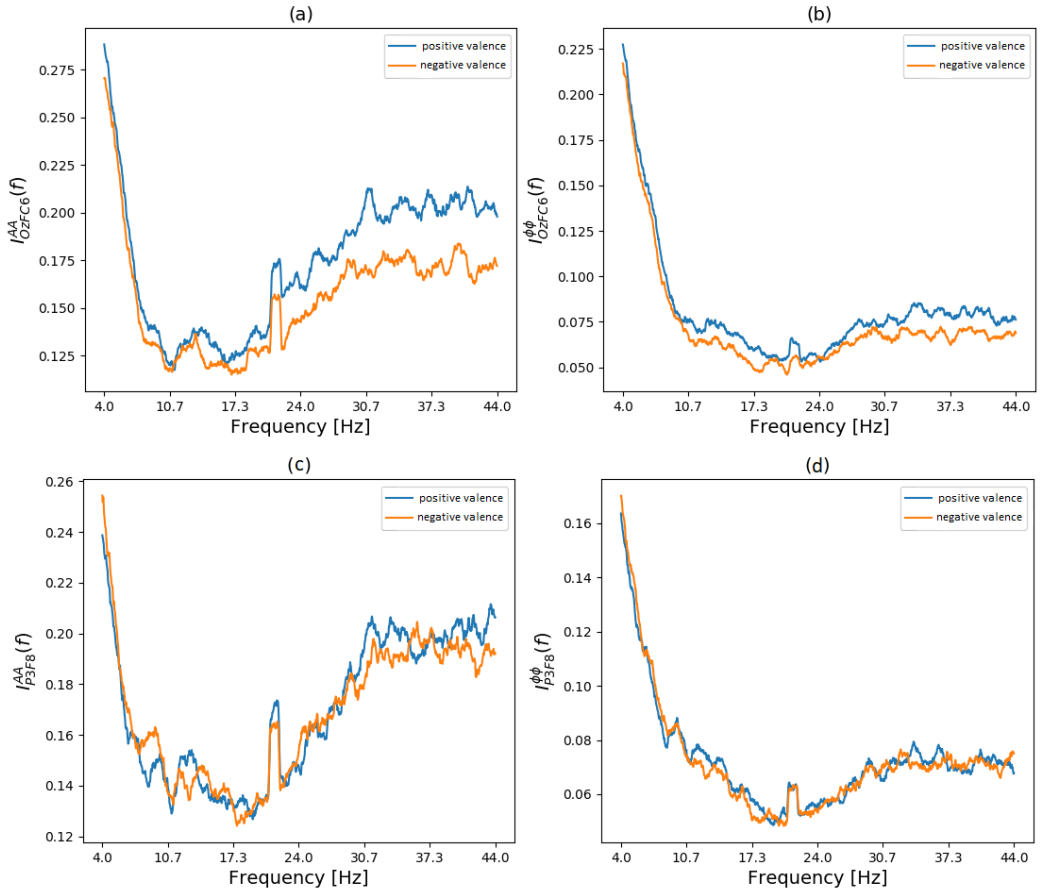

Figure 4.13: Negative/positive valence state plots of (a) $I^{AA}_{XY}(f)$ and (b) $I^{\phi\phi}_{XY}(f)$ for EEG channel pair Oz–FC6, (c) $I^{AA}_{XY}(f)$ and (d) $I^{\phi\phi}_{XY}(f)$ for EEG channel pair (P3–F8).

On the other hand, for the case of arousal, $I^{AA}_{XY}(f)$ and $I^{\phi\phi}_{XY}(f)$ from the same channel pairs are shown in Figure 4.14. $I^{AA}_{XY}(f)$ in panels (a) and (c) separates high arousal from low arousal more clearly than $I^{\phi\phi}_{XY}(f)$ in panels (b) and (d) for both pairs. Channel wise, low/high arousal are more separable in P3–F8 pair (panels (c) and (d)) than in Oz–FC6 (panels (a) and (b)).

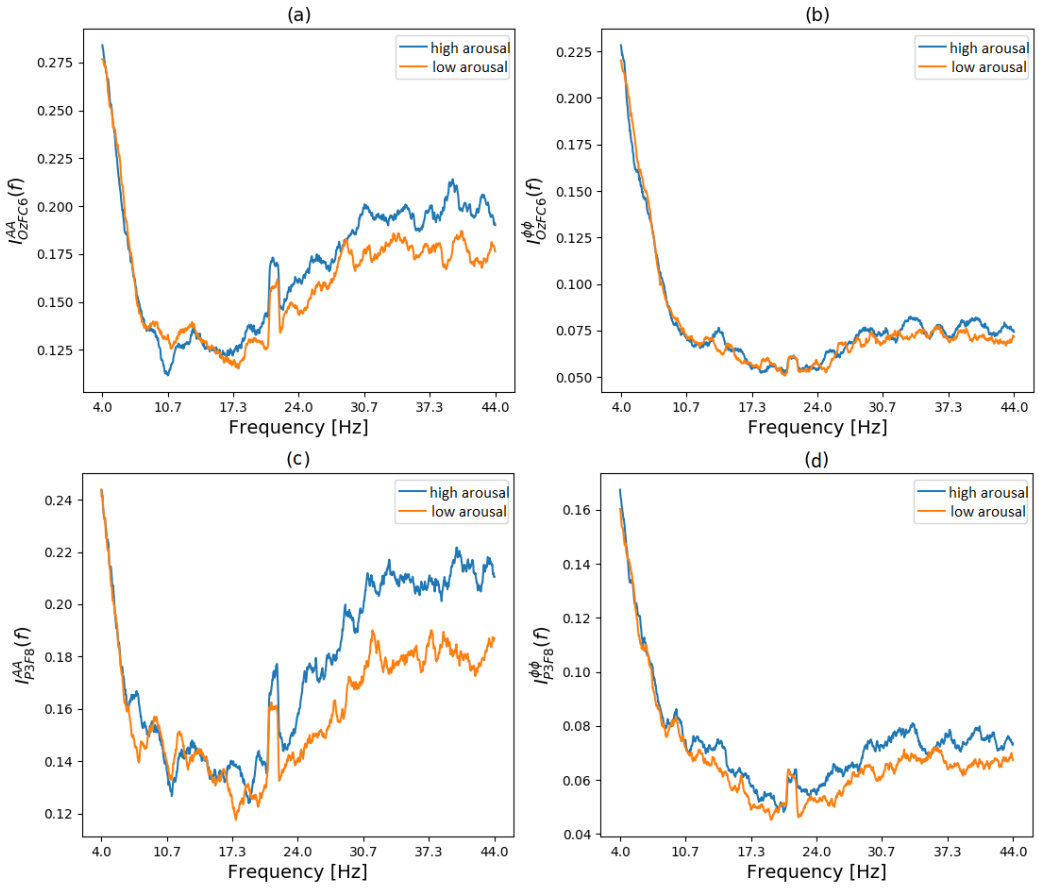

Figure 4.14: Low/high arousal state plots of (a) $I^{AA}_{XY}(f)$ and (b) $I^{\phi\phi}_{XY}(f)$ for EEG channel pair Oz–FC6, (c) $I^{AA}_{XY}(f)$ and (d) $I^{\phi\phi}_{XY}(f)$ for EEG channel pair (P3–F8).

The entire measure plots for $I^{AA}_{XY}(f)$, the case of valence on all (496) channel pairs are provided in Appendix A.

To summarize the information provided by the 496 MI measures estimated from the 32 channels, we sum the measure values that are associated with the same channel i to obtain an aggregate measure of its overall dependency to the others and we define the cumulative MI in terms of magnitudes with respect to channel i as $SI^{AA}_i(f) = \sum_j I^{AA}_{ij}(f)$. To investigate the quantitative difference between the

positive/high and the negative/low states with respect to both brain regions and frequencies, we further subtract the SI_i of negative/low state from the positive/high state and we denote it as DSI_i. Figures 4.15–4.18 present this quantity, specifically $DSI_i^{AA}(f)$ and $DSI_i^{\phi\phi}(f)$, across channels (vertical axis) and frequencies (horizontal axis) for the cases of valence and arousal. We note that due to the pre–processing of the data, only the frequencies ranging from 4 to 44 Hz are used. In Figure 4.15, the $DSI_i^{AA}(f)$ for positive/negative valence vary between -0.504 and 0.878, with the most significant differences appearing in Oz and Pz (occipital and parietal lobes) at frequencies above 30 Hz, as well as a smaller difference in Fp1 (left frontal lobe), again at high frequencies.

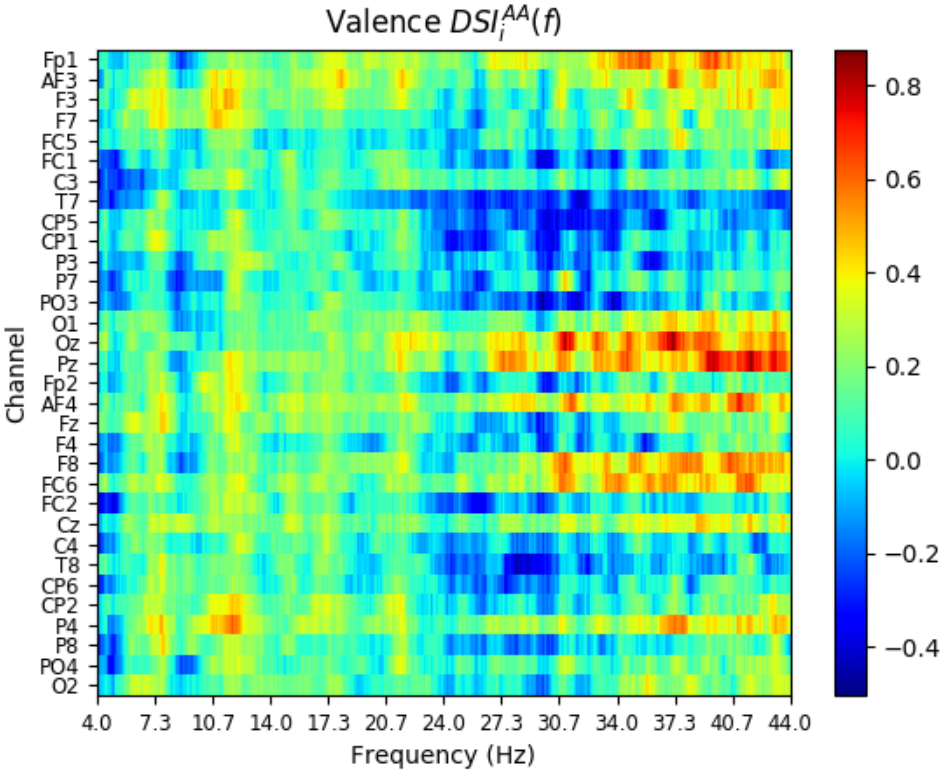

Figure 4.15: $DSI_i^{AA}(f)$ for different channels (vertical axis) and frequencies (horizontal axis) for the case of valence. For visualization purposes, a moving average filter of length 30 is applied on the horizontal axis.

$DSI_i^{\phi\phi}(f)$ measure for valence is shown in Figure 4.16. The highest (difference) values between positive/negative states repeatedly appear in channels Oz and Pz beyond 24 Hz, and channel T8 stands out with a comparable range but negative values at the same frequencies. This means while the overall $I^{\phi\phi}(f)$ for channels Oz and Pz are higher in positive valence compared with negative valence, the overall $I^{\phi\phi}(f)$ for channel T8 holds the opposite patterns in difference between positive and negative states of valence.

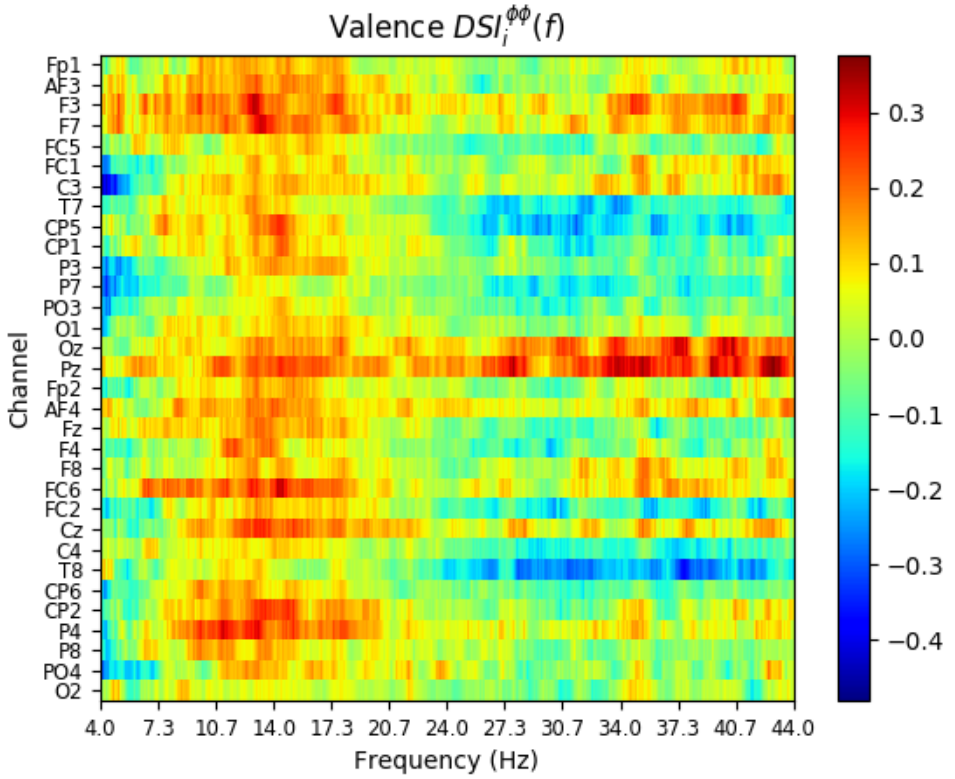

Figure 4.16: $DSI_i^{\phi\phi}(f)$ for different channels (vertical axis) and frequencies (horizontal axis) for the case of valence. For visualization purposes, a moving average filter of length 30 is applied on the horizontal axis.

In Figure 4.17, the difference between high/low arousal per channel ($DSI_i^{AA}(f)$) is presented across all frequencies. Among them, channels P3 and F8 both show relatively high values beyond 30 Hz. However, channel T7 holds negative high values (in deep blue color) at very low frequencies (slightly above 4 Hz). Similarly with the interpretation to channel T8 in Figure 4.16, channel T7 exhibits overall higher values ($I^{AA}(f)$) for low arousal state than the high arousal state.

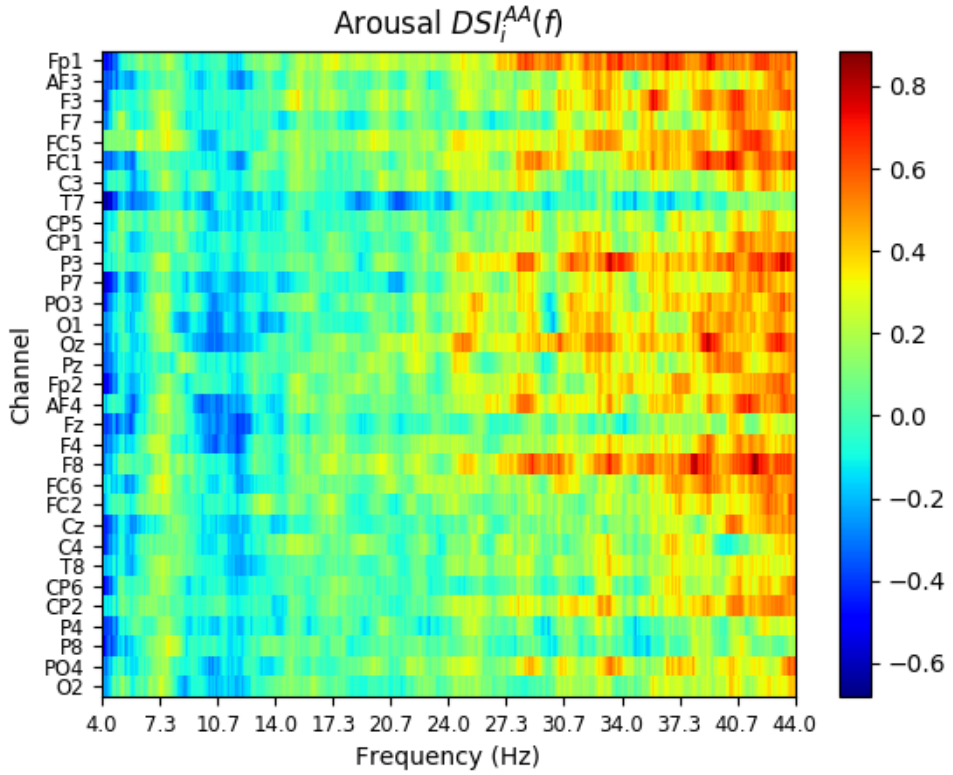

Figure 4.17: $DSI_i^{AA}(f)$ for different channels (vertical axis) and frequencies (horizontal axis) for the case of arousal. For visualization purposes, a moving average filter of length 30 is applied on the horizontal axis.

The measure $DSI_i^{\phi\phi}(f)$ for the dimension of arousal is presented in Figure 4.18. Additional channels i.e., F3, F4, and CP2 above 30 Hz, behave similarly with P3 and F8 in representing the positive difference from high arousal state to low arousal state. Channel AF4 at around 6 Hz is similar to T7 at a lower frequency in showing the negative difference from high arousal state to low arousal state.

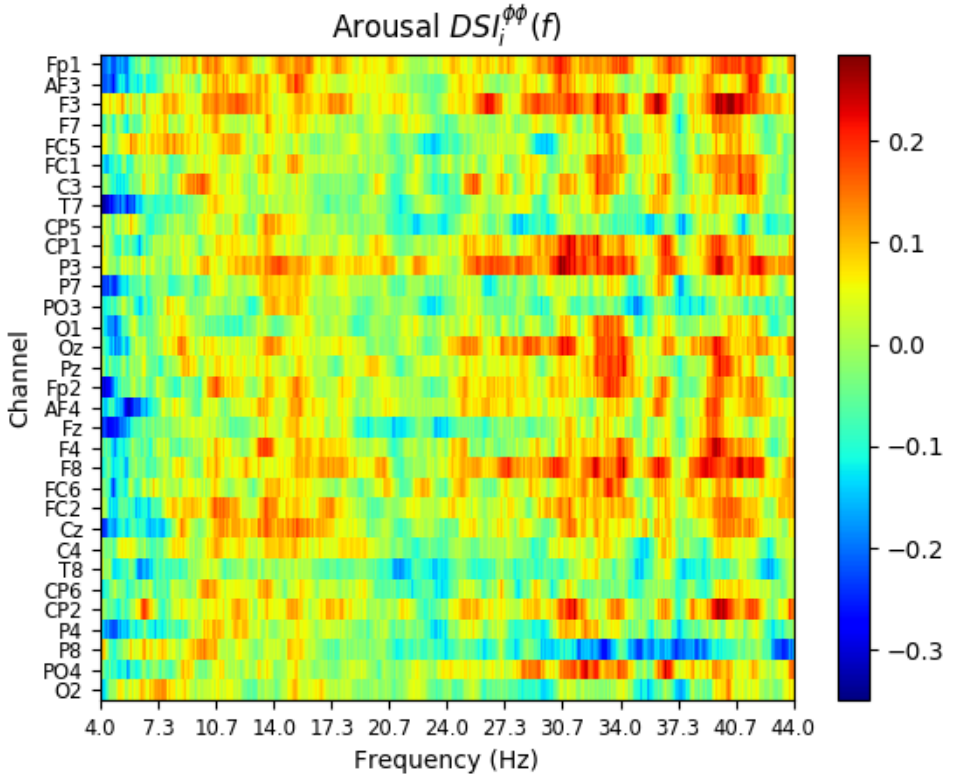

Figure 4.18: $DSI_i^{\phi\phi}(f)$ for different channels (vertical axis) and frequencies (horizontal axis) for the case of arousal. For visualization purposes, a moving average filter of length 30 is applied on the horizontal axis.

Plots with respect to $DSI_i^{A\phi}(f)$ and $DSI_i^{\phi A}(f)$ are listed in Appendix B due to the much smaller ranges for the corresponding measure values compared with $DSI_i^{AA}(f)$ and $DSI_i^{\phi\phi}(f)$, and the fact that they do not provide any useful information.

The estimates of $DSI_i^{AA}(f)$ and $DSI_i^{\phi\phi}(f)$ are averaged across the traditional brain frequency bands, i.e., θ, α, β and low γ (limited by data as 30–45 Hz), and presented through brain topographic plots in Figure 4.19. The measures $DSI_i^{A\phi}(f)$ and $DSI_i^{\phi A}(f)$ do not showcase anything interesting (as in the cases of the artificial

data from coupled systems), so we omit their presentation. Panel (a) shows the results for the valence dimension. DSI_i^{AA} shows that channels Pz and Oz in the low γ band exhibit the highest difference between positive and negative valence with values 0.5183 and 0.510 respectively, followed by channels F8, FC6, Fp1, and AF4. $DSI_i^{\phi\phi}(f)$ exhibits similar behavior at the low γ band, but with MI values being in general much smaller than those of DSI_i^{AA}. For the case of high vs. low arousal (panel (b)) DSI_i^{AA} shows the major differences in the low γ band at Fp1, F8, and P3 with values 0.563, 0.547 and 0.504, followed by FC1, F3, and FC5. $DSI_i^{\phi\phi}$ again exhibits much smaller values, with similar patterns as DSI_i^{AA} at the low γ band.

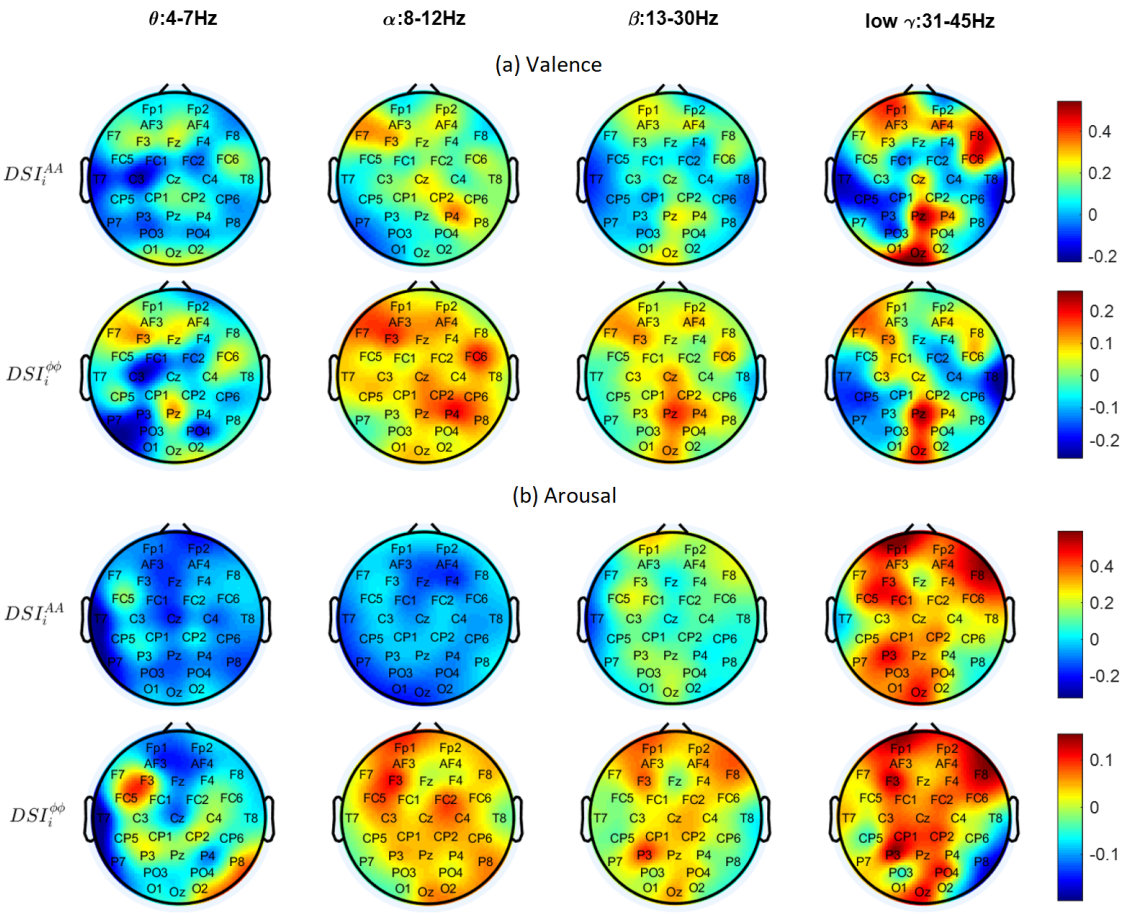

Figure 4.19: Topographic maps of $DSI_i^{AA}(f)$ and $DSI_i^{\phi\phi}(f)$, averaged for each frequency band, as indicated on the top of the figure for (a) valence and (b) arousal.

In summary, the difference between positive and negative valence and high and low arousal are mostly observed with respect to magnitude MIs in the midline occipital and parietal lobes, and bilaterally in the frontal lobe, at high frequencies and are distinct between the two emotional dimensions. Physiological aspects of these observations are further discussed in the next section.

CHAPTER 5

DISCUSSION AND CONCLUSIONS

5.1 Evaluation of the Developed Methodology

Our results from the simulated data showed that frequency–based MI performs better than the linear and traditionally used measure of Coherence. For the Lorenz system, two out of four measures ($I_{XY}^{\phi\phi}(f)$ and $I_{XY}^{\phi A}(f)$) emphasized the nonlinear dependency between x and z at the primary frequency component, while the linear measure ($C_{XY}(f)$) failed. In the bidirectionally coupled Lorenz systems case, both $I_{XY}^{AA}(f)$ and $I_{XY}^{\phi\phi}(f)$ showed an increasing dependency relation at 1.8 Hz (the primary frequency of the second subsystem) as the coupling parameter increased. $C_{XY}(f)$ was much less specific in capturing these phenomena, taking high values for much wider frequency regions around the primary frequency and over the whole frequency range. In the last model (coupled Mackey–Glass equations) with 4 sets of parameters, the developed measures were able to track the increase of dependency at certain frequencies as the coupling parameter increased, while coherence again performed poorly, rising rapidly and remaining on a plateau, ultimately failing to accurately capture the underlying changes in the system.

Overall, the developed measures were able to correctly identify the interactions in the systems and localize them in the frequency domain. A limitation of our

methodology is the data volume requirement. This type of nonparametric analysis needs enough data to accurately obtain the spectral characteristics and provide a good estimate of their density functions. This means that the individual segments of the time series should be sufficiently long, and that the number of segments should be sufficiently large. Although the kernel density estimates we employed are considered efficient for Gaussian data, in practice and due to non–Gaussianity of the spectral characteristics, alternative methods (e.g., nearest neighbor density estimates) may allow for smaller number of segments, thus decreasing the data requirements.

Apart from the first test–case of simulated data (single Lorenz system), the combined magnitude–phase MI measure ($I_{XY}^{A\phi}(f)$ and $I_{XY}^{\phi A}(f)$) did not show anything interesting or promising. Most probably this is due to lack of any such interactions in the coupled systems that were tested. The way the coupling is introduced in these systems is a simple additive term, which we expect to have a higher impact in the magnitude of the time series but not necessarily on the phases. More complicated coupling schemes can induce magnitude–phase interactions that would be able to be captured by these measures. Another possible explanation is the magnitude–phase interactions are cross–frequency in nature. This explanation is further corroborated by the current trend in neurosience of cross–frequency phase–magnitude coupling in the brain [107, 80, 108], and the fact that nonlinear interactions have the potential to create new frequencies [109, 110].

5.2 Affective States Analysis

In affective state research, brain regions from the frontal lobes [111], parietal lobes [68], and from the temporal lobes [112] have been previously reported to be related to emotional response. Application of the developed methodology on the emotional behavior EEG dataset revealed that positive valance and high arousal is associated with increased connectivity in specific regions of the frontal, occipital and parietal lobes. The involvement of the frontal lobe is in accordance to the known relation of this brain region to emotional processing [66]. Valance was associated with the right frontocentral and left prefrontal regions (electrodes F8 and Fp1 respectively), while for arousal involvement of these two regions was observed, as well as left frontocentral (electrode F3). The occipital lobe corresponds to the visual cortex, and it has been reported that emotional processing begins with vision [74], and that perceptual encoding in the visual cortex is modulated by the emotional significance of visual stimuli [79]. Given the setup of the experiment (visual stimuli in the form of videos), we believe that the involvement of the visual cortex reflects these underlying neuronal processes. Finally, the increased connectivity in the parietal cortex can be attributed again to the processing of visual stimuli, or to somatosensation, which is also believed to be related to emotional responses [76]. With respect to EEG frequency bands, the observed results were mostly confined to the γ band, which is associated with higher brain functions, and has been reported to be related to emotional responses [72, 71, 70]. In alignment with this, Jatupaiboon et al. also suggested that higher frequency bands (β and γ) provide higher accuracy in happiness detection tasks [112].

5.3 Conclusion

We developed a general method to measure dependencies between time series with respect to frequency, based on their spectral characteristics. The methodology is intuitively appropriate for time series generated from biological systems, whose outputs typically containing distinct frequency components.

The identification of dependency relations in a system can be used to detect the functional structures and interactions, and direct system–level simulations and modeling. The developed methodology expands on ideas of nonlinear dependency and interactions and provides a new way to quantify relations with respect to frequency, thus making it highly suitable for studying many and diverse systems in biomedical sciences.

5.4 Future Work

Our measures of Mutual Information in the frequency domain is currently focusing on two distinct components (two variables X and Y) of a biological system. To expand the study of the interaction to more components from the system at once, a similar methodology employing the multivariate version of mutual information (i.e., $I(X;Y;Z)$) can be developed with respect to frequency features. Additionally, conditional MI ($I(X;Y|Z)$) measures the association between X and Y when given the information of Z. This quantity once estimated can also reveal the relation among the multi–variables X, Y, and Z. Finally, these scalar variables can be replaced by a collection of variables (i.e., $\mathbf{X} = (X_1, X_2, ..., X_n)$) in order to investigate the interaction among clusters of system components.

Also, extension of the developed methodology to a cross–frequency implementation would be straightforward, with simple modification in the definition of the measures. Of course, this extension would be computationally expensive and complicated with respect to the analysis of the results, since the cross–frequency setup increases dimensionality. Nonetheless, such an extension of the current algorithm will complement the results reported herein and help further explain the underlying mechanisms for the cases we examine.

Finally, an interesting application of our methodology would be in the case of multimodal signals, i.e., signals that are obtained from different recording methods; they are very different in nature and/or represent different aspect of the activity of the system components (e.g., ECG–EEG or ECG–fMRI). Since our measures do not make any assumptions about the data and the relations between the systems' components but use the probability densities to quantify the interaction, we consider them highly suitable for the study of multimodal signals.

APPENDIX A

FIGURE SET 1

Supplement figures for $I_{XY}^{AA}(f)$ for valence dimension.

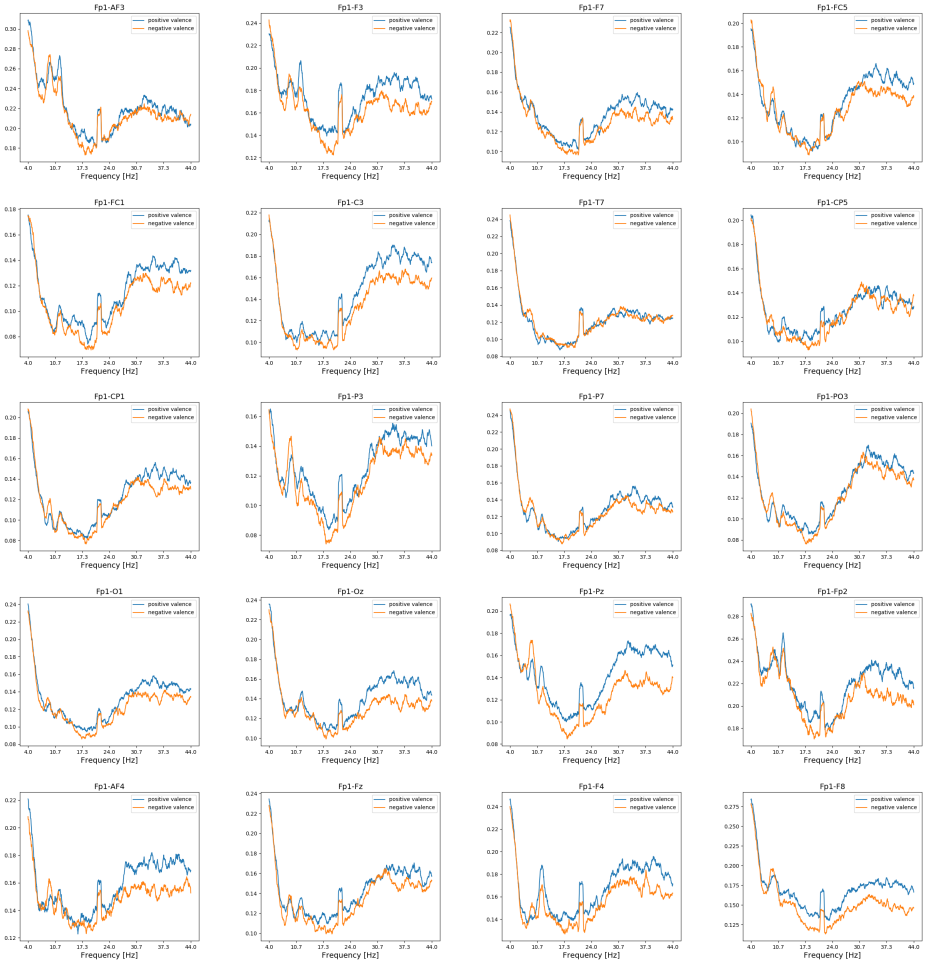

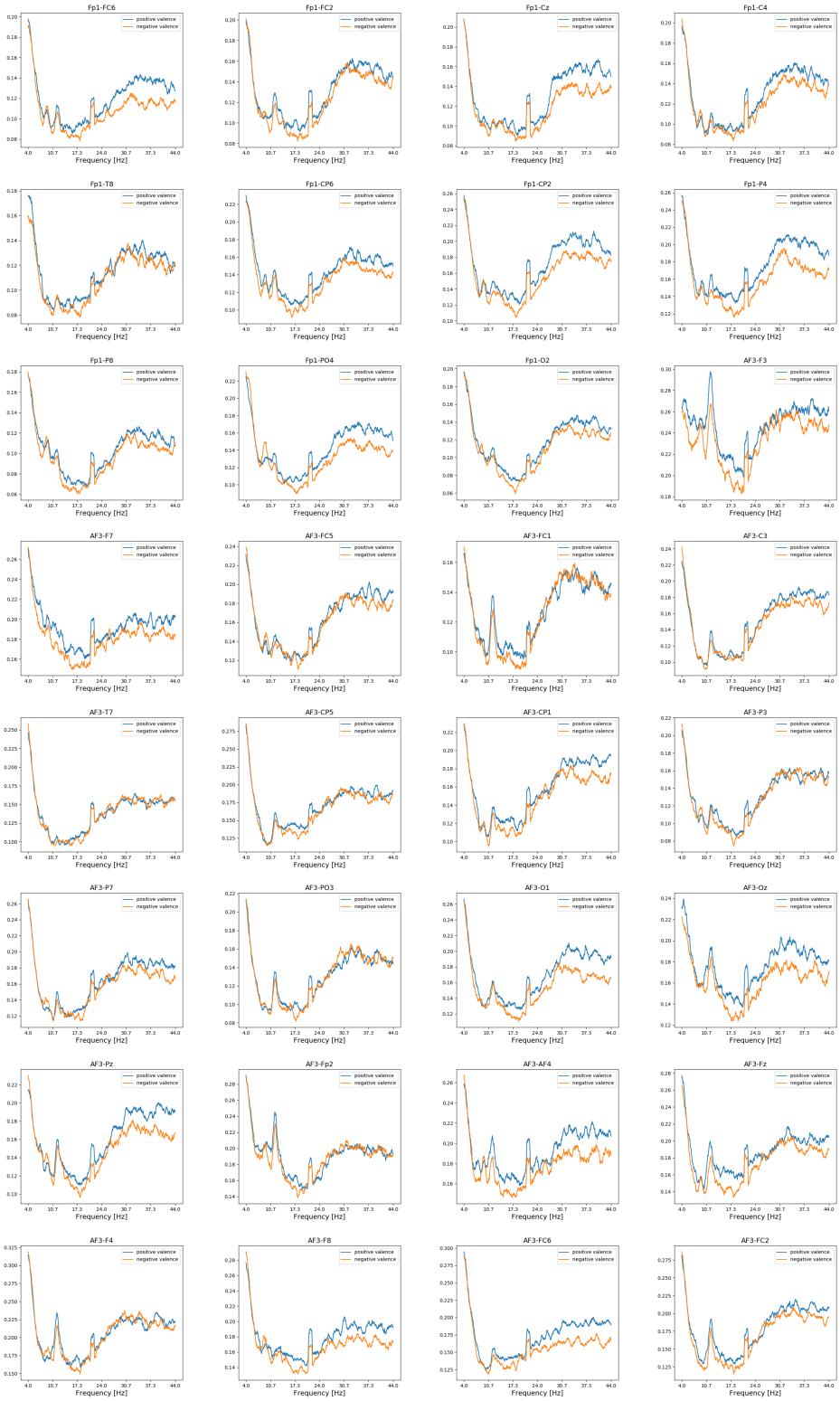
Fp1-FC6
Fp1-FC2
Fp1-Cz
Fp1-C4
Fp1-T8
Fp1-CP6
Fp1-CP2
Fp1-P4
Fp1-P8
Fp1-PO4
Fp1-O2
AF3-F3
AF3-F7
AF3-FC5
AF3-FC1
AF3-C3
AF3-T7
AF3-CP5
AF3-CP1
AF3-P3
AF3-P7
AF3-PO3
AF3-O1
AF3-Oz
AF3-Pz
AF3-Fp2
AF3-AF4
AF3-Fz
AF3-F4
AF3-F8
AF3-FC6
AF3-FC2
positive valence
negative valence
Frequency [Hz]

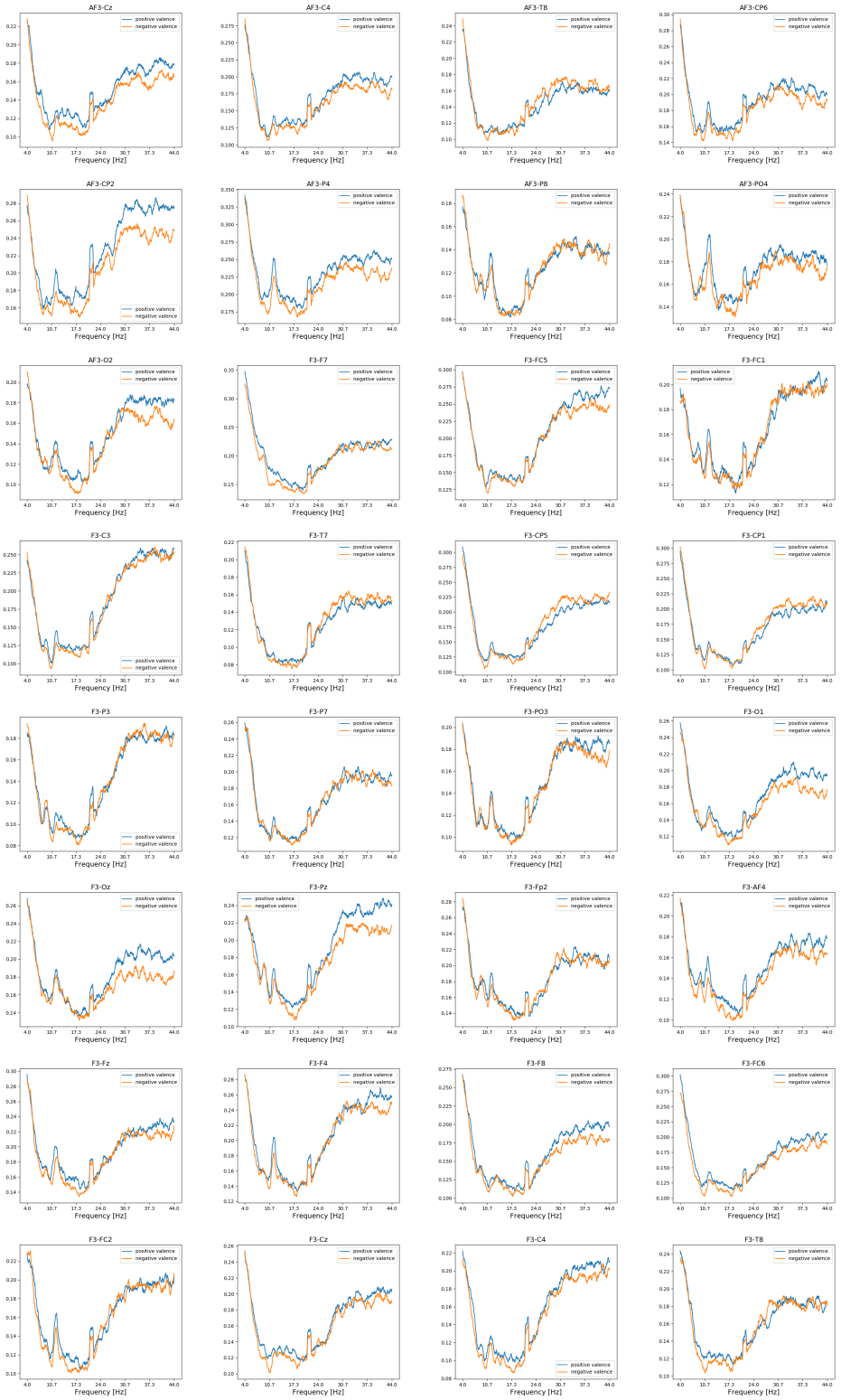
AF3-Cz
AF3-C4
AF3-T8
AF3-CP6
AF3-CP2
AF3-P4
AF3-P8
AF3-PO4
AF3-O2
F3-F7
F3-FC5
F3-FC1
F3-C3
F3-T7
F3-CP5
F3-CP1
F3-P3
F3-P7
F3-PO3
F3-O1
F3-Oz
F3-Pz
F3-Fp2
F3-AF4
F3-Fz
F3-F4
F3-F8
F3-FC6
F3-FC2
F3-Cz
F3-C4
F3-T8
positive valence
negative valence
Frequency [Hz]

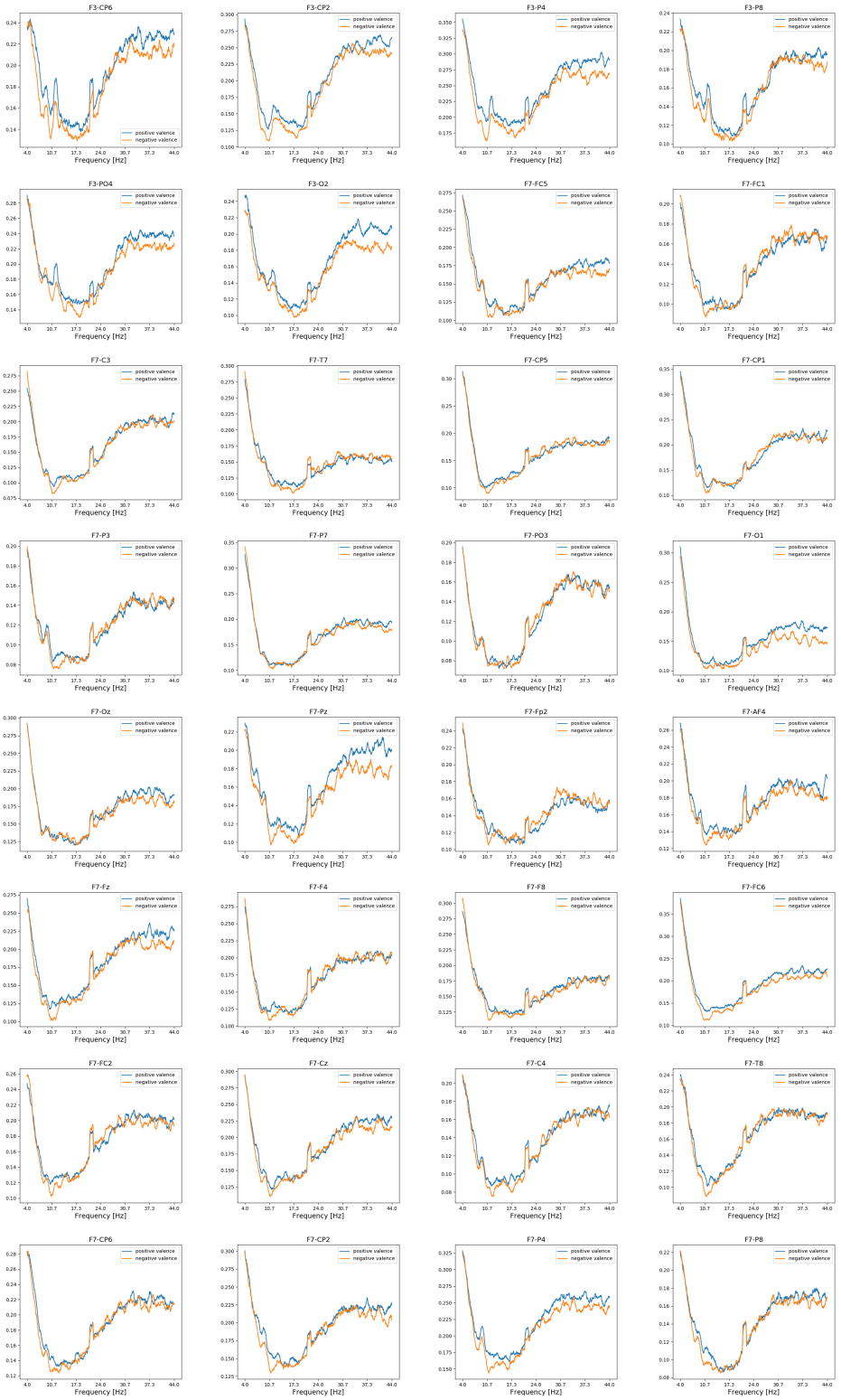
F3-CP6
F3-CP2
F3-P4
F3-P8
F3-PO4
F3-O2
F7-FC5
F7-FC1
F7-C3
F7-T7
F7-CP5
F7-CP1
F7-P3
F7-P7
F7-PO3
F7-O1
F7-Oz
F7-Pz
F7-Fp2
F7-AF4
F7-Fz
F7-F4
F7-F8
F7-FC6
F7-FC2
F7-Cz
F7-C4
F7-T8
F7-CP6
F7-CP2
F7-P4
F7-P8
positive valence
negative valence
Frequency [Hz]

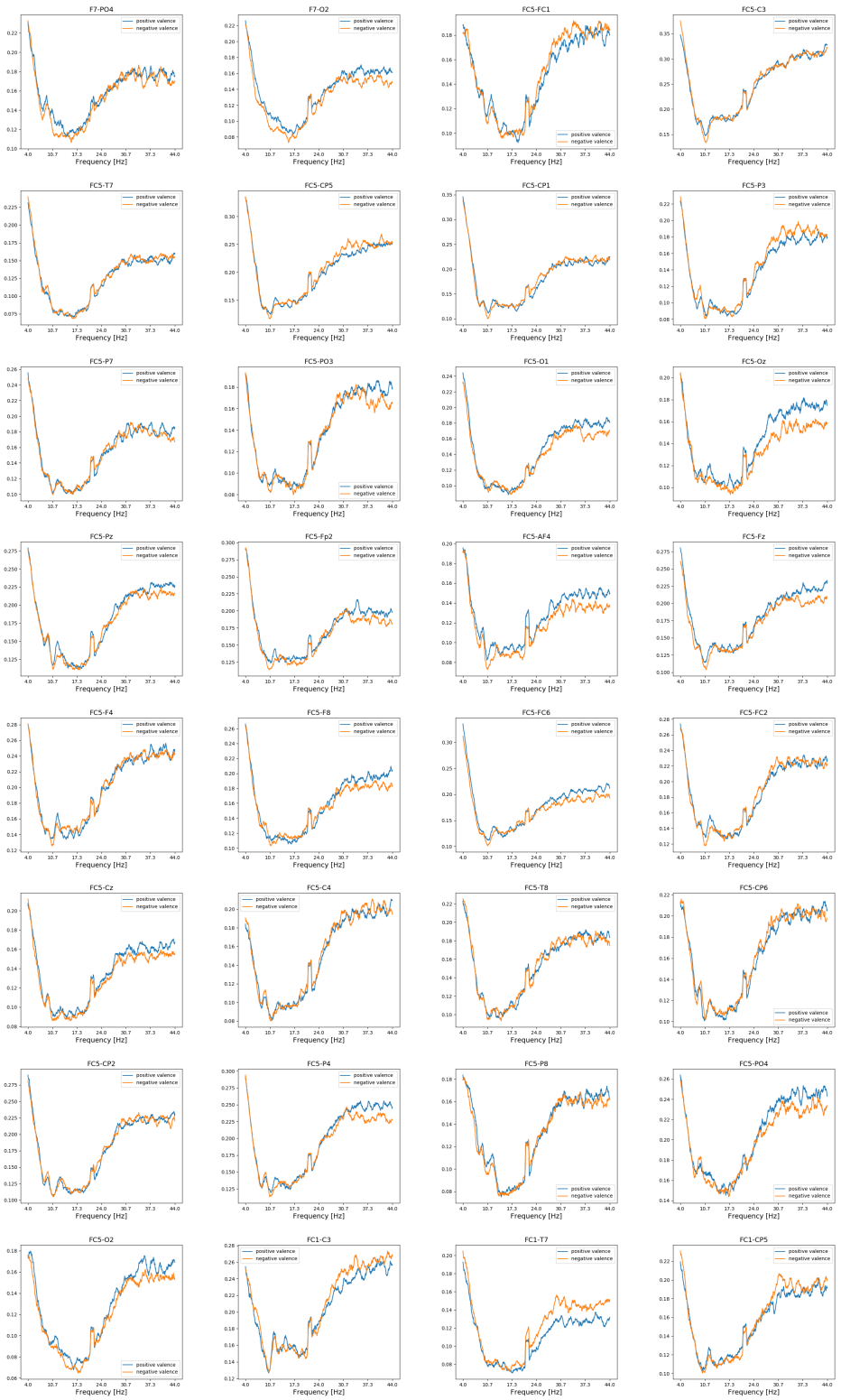
F7-PO4
F7-O2
FC5-FC1
FC5-C3
FC5-T7
FC5-CP5
FC5-CP1
FC5-P3
FC5-P7
FC5-PO3
FC5-O1
FC5-Oz
FC5-Pz
FC5-Fp2
FC5-AF4
FC5-Fz
FC5-F4
FC5-F8
FC5-FC6
FC5-FC2
FC5-Cz
FC5-C4
FC5-T8
FC5-CP6
FC5-CP2
FC5-P4
FC5-P8
FC5-PO4
FC5-O2
FC1-C3
FC1-T7
FC1-CP5
positive valence
negative valence
Frequency [Hz]

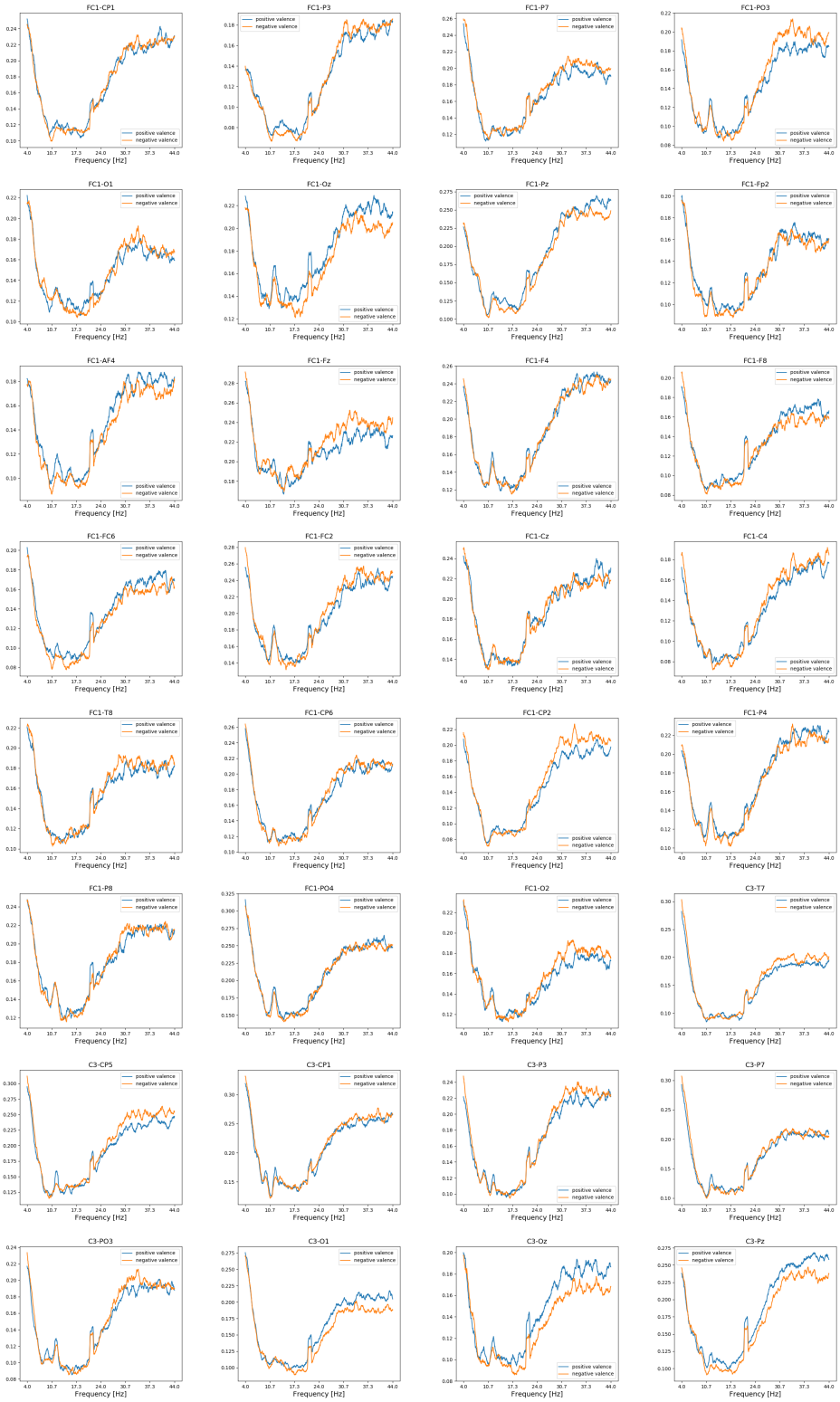
FC1-CP1
FC1-P3
FC1-P7
FC1-PO3
FC1-O1
FC1-Oz
FC1-Pz
FC1-Fp2
FC1-AF4
FC1-Fz
FC1-F4
FC1-F8
FC1-FC6
FC1-FC2
FC1-Cz
FC1-C4
FC1-T8
FC1-CP6
FC1-CP2
FC1-P4
FC1-P8
FC1-PO4
FC1-O2
C3-T7
C3-CP5
C3-CP1
C3-P3
C3-P7
C3-PO3
C3-O1
C3-Oz
C3-Pz
positive valence
negative valence
Frequency [Hz]

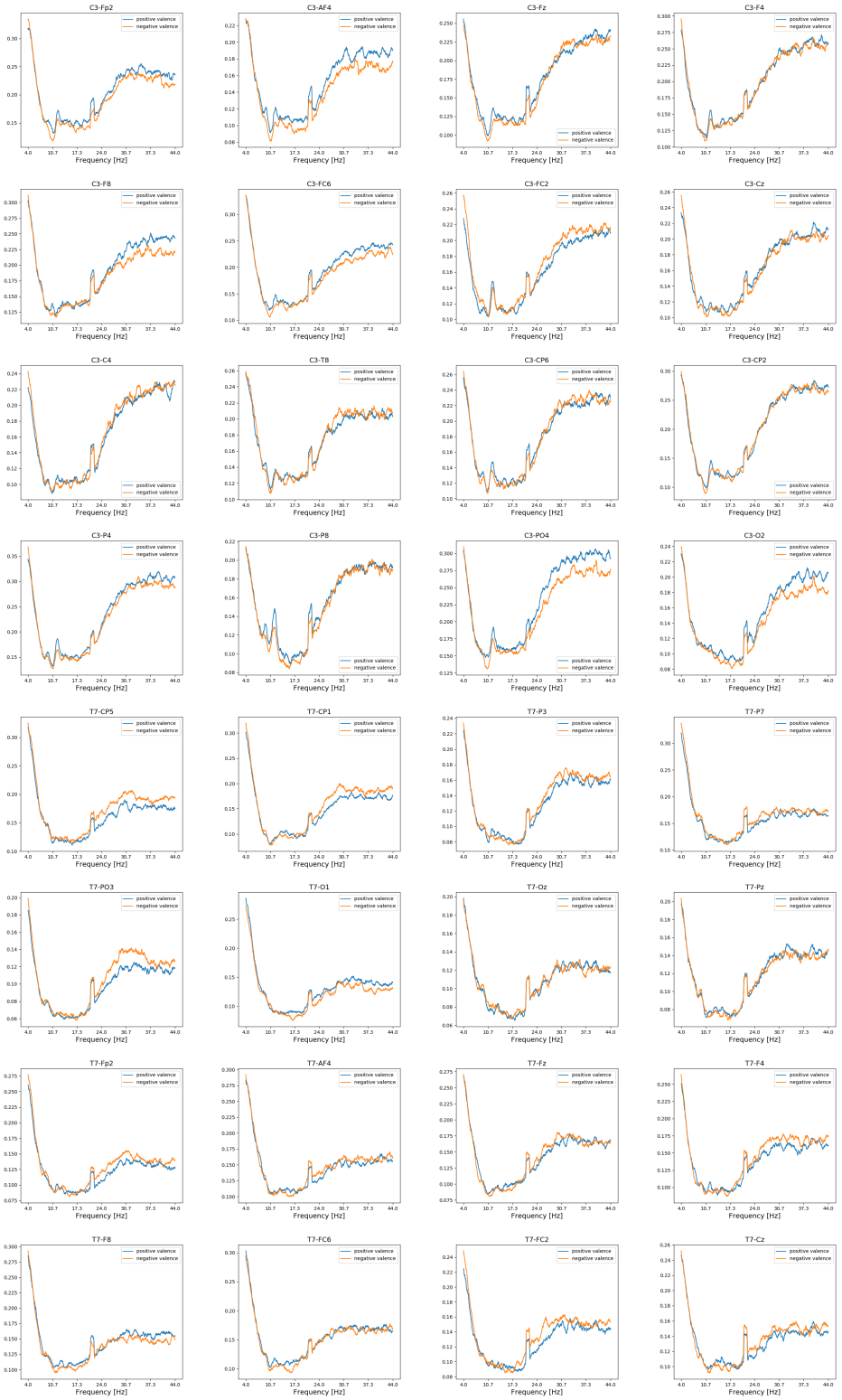
C3-Fp2
C3-AF4
C3-Fz
C3-F4
C3-F8
C3-FC6
C3-FC2
C3-Cz
C3-C4
C3-T8
C3-CP6
C3-CP2
C3-P4
C3-P8
C3-PO4
C3-O2
T7-CP5
T7-CP1
T7-P3
T7-P7
T7-PO3
T7-O1
T7-Oz
T7-Pz
T7-Fp2
T7-AF4
T7-Fz
T7-F4
T7-F8
T7-FC6
T7-FC2
T7-Cz
positive valence
negative valence
Frequency [Hz]

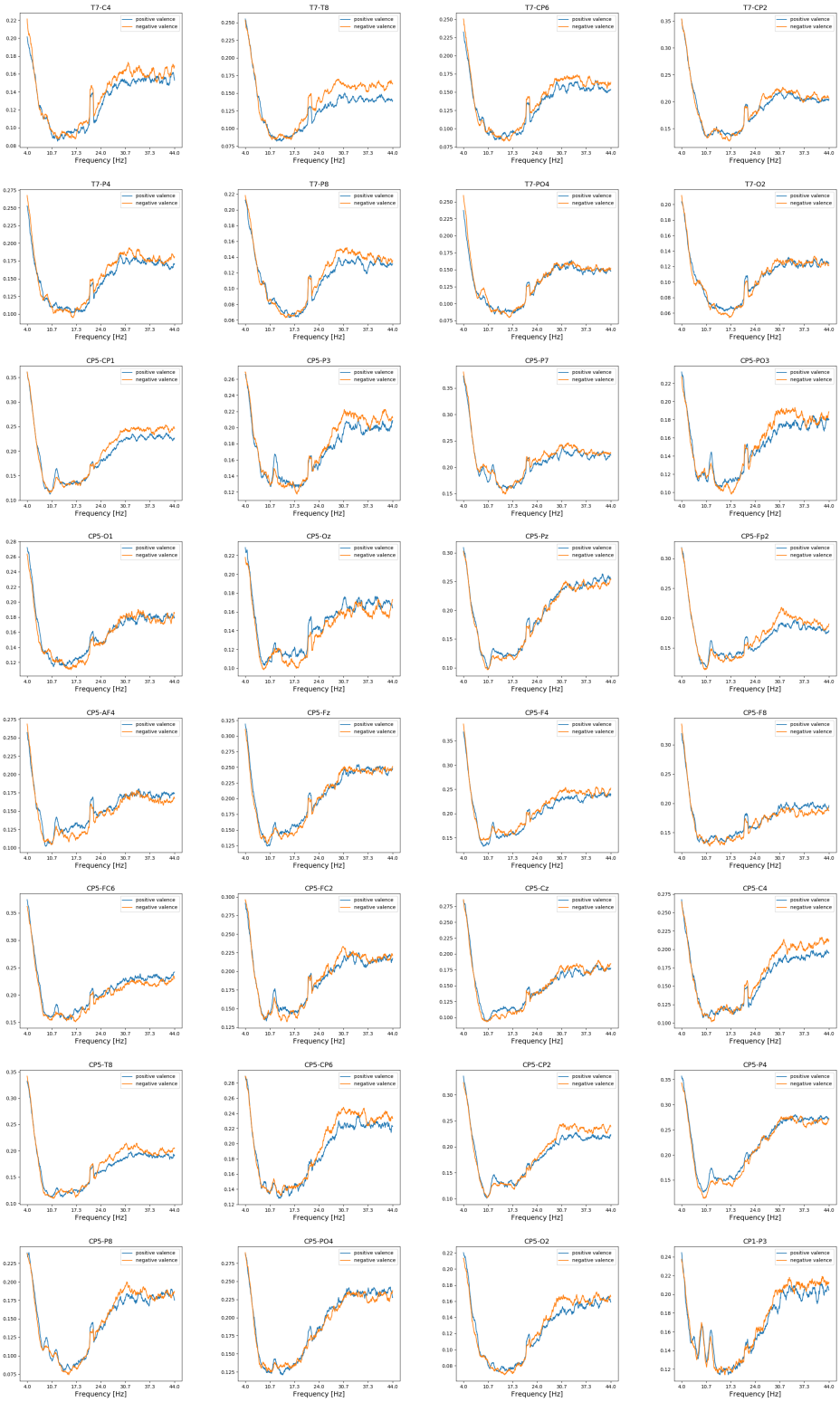
T7-C4
T7-T8
T7-CP6
T7-CP2
T7-P4
T7-P8
T7-PO4
T7-O2
CP5-CP1
CP5-P3
CP5-P7
CP5-PO3
CP5-O1
CP5-Oz
CP5-Pz
CP5-Fp2
CP5-AF4
CP5-Fz
CP5-F4
CP5-F8
CP5-FC6
CP5-FC2
CP5-Cz
CP5-C4
CP5-T8
CP5-CP6
CP5-CP2
CP5-P4
CP5-P8
CP5-PO4
CP5-O2
CP1-P3
positive valence
negative valence
Frequency [Hz]

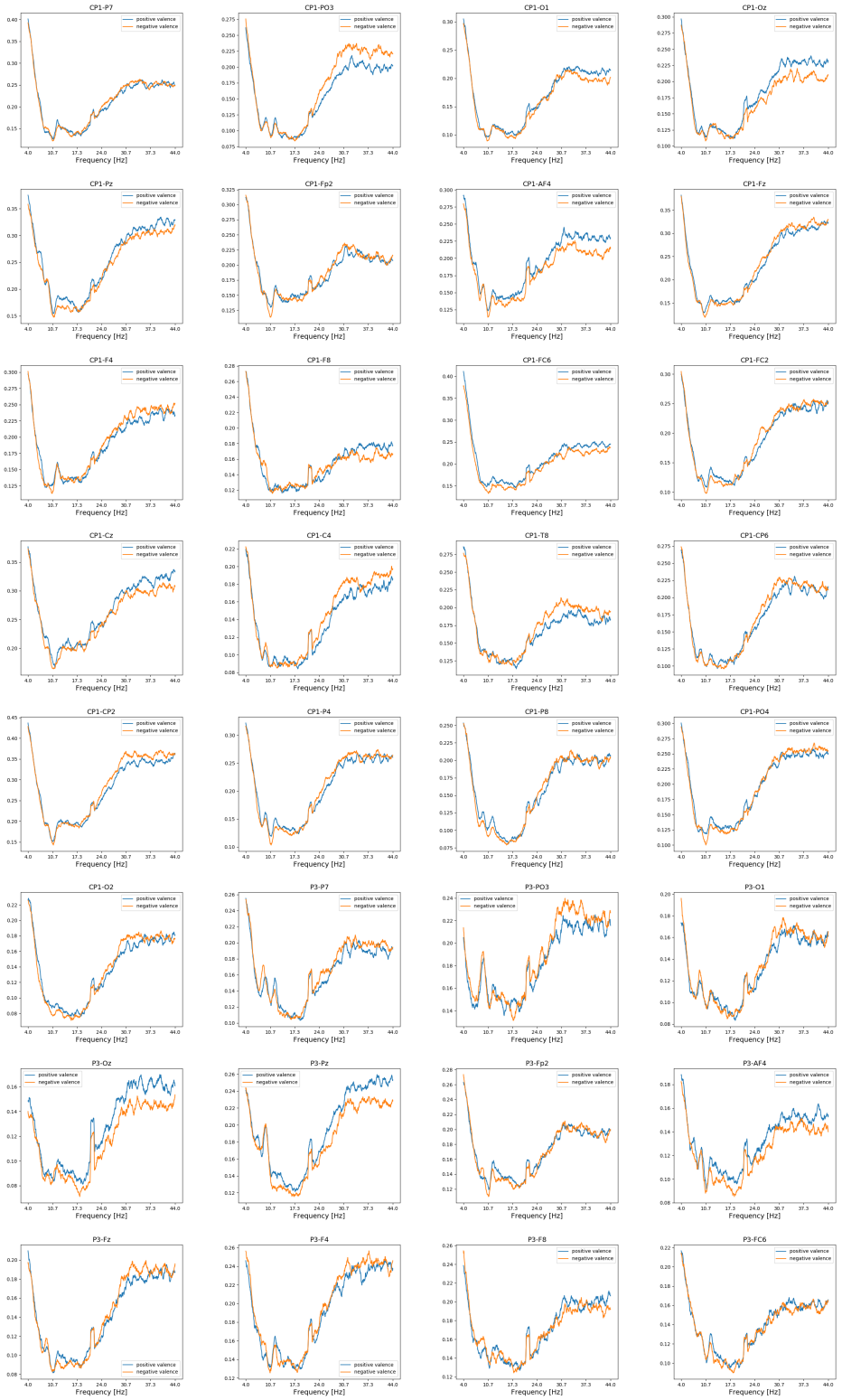
CP1-P7
CP1-PO3
CP1-O1
CP1-Oz
CP1-Pz
CP1-Fp2
CP1-AF4
CP1-Fz
CP1-F4
CP1-F8
CP1-FC6
CP1-FC2
CP1-Cz
CP1-C4
CP1-T8
CP1-CP6
CP1-CP2
CP1-P4
CP1-P8
CP1-PO4
CP1-O2
P3-P7
P3-PO3
P3-O1
P3-Oz
P3-Pz
P3-Fp2
P3-AF4
P3-Fz
P3-F4
P3-F8
P3-FC6
positive valence
negative valence
Frequency [Hz]

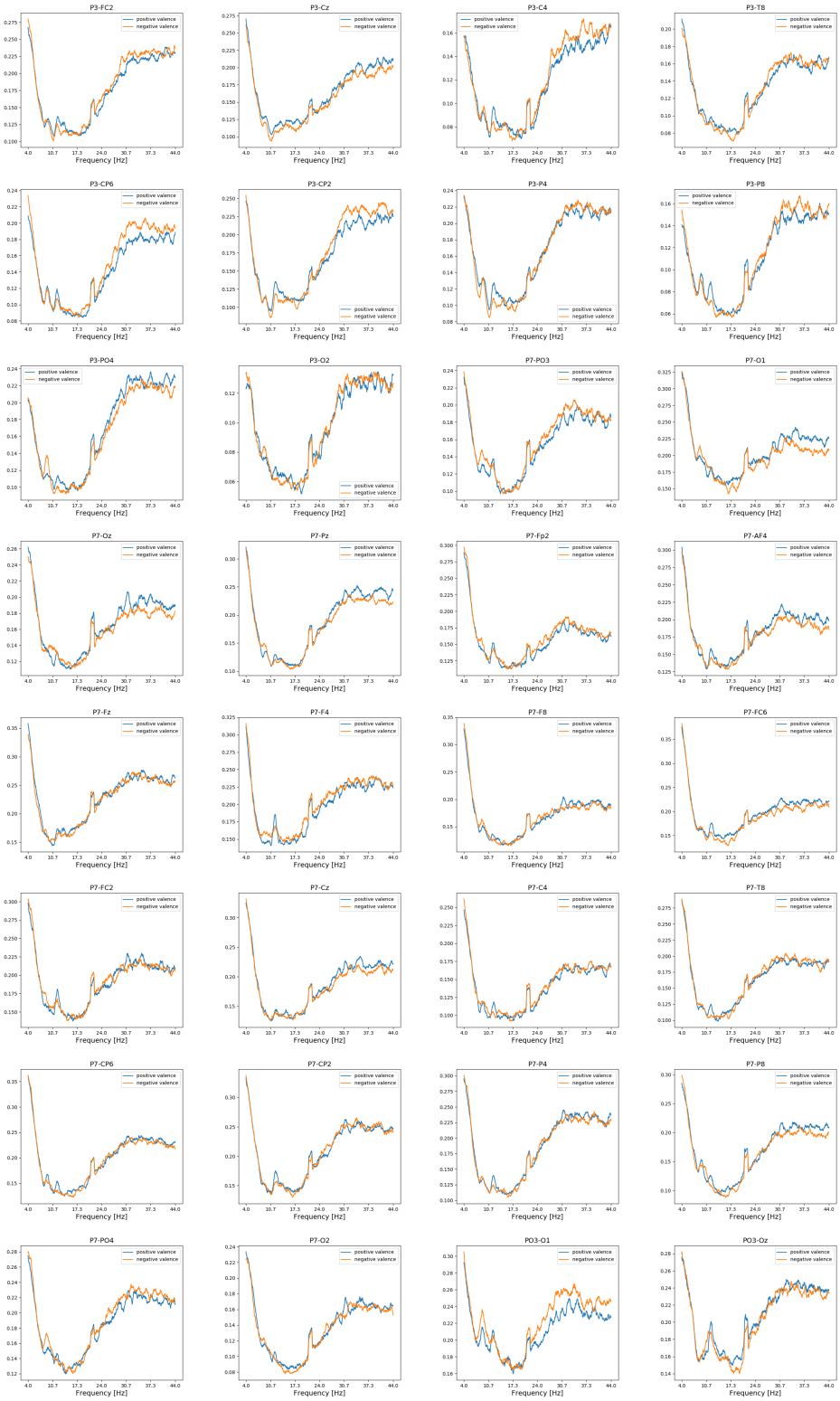
P3-FC2
P3-Cz
P3-C4
P3-T8
P3-CP6
P3-CP2
P3-P4
P3-P8
P3-PO4
P3-O2
P7-PO3
P7-O1
P7-Oz
P7-Pz
P7-Fp2
P7-AF4
P7-Fz
P7-F4
P7-F8
P7-FC6
P7-FC2
P7-Cz
P7-C4
P7-T8
P7-CP6
P7-CP2
P7-P4
P7-P8
P7-PO4
P7-O2
PO3-O1
PO3-Oz
positive valence
negative valence
Frequency [Hz]

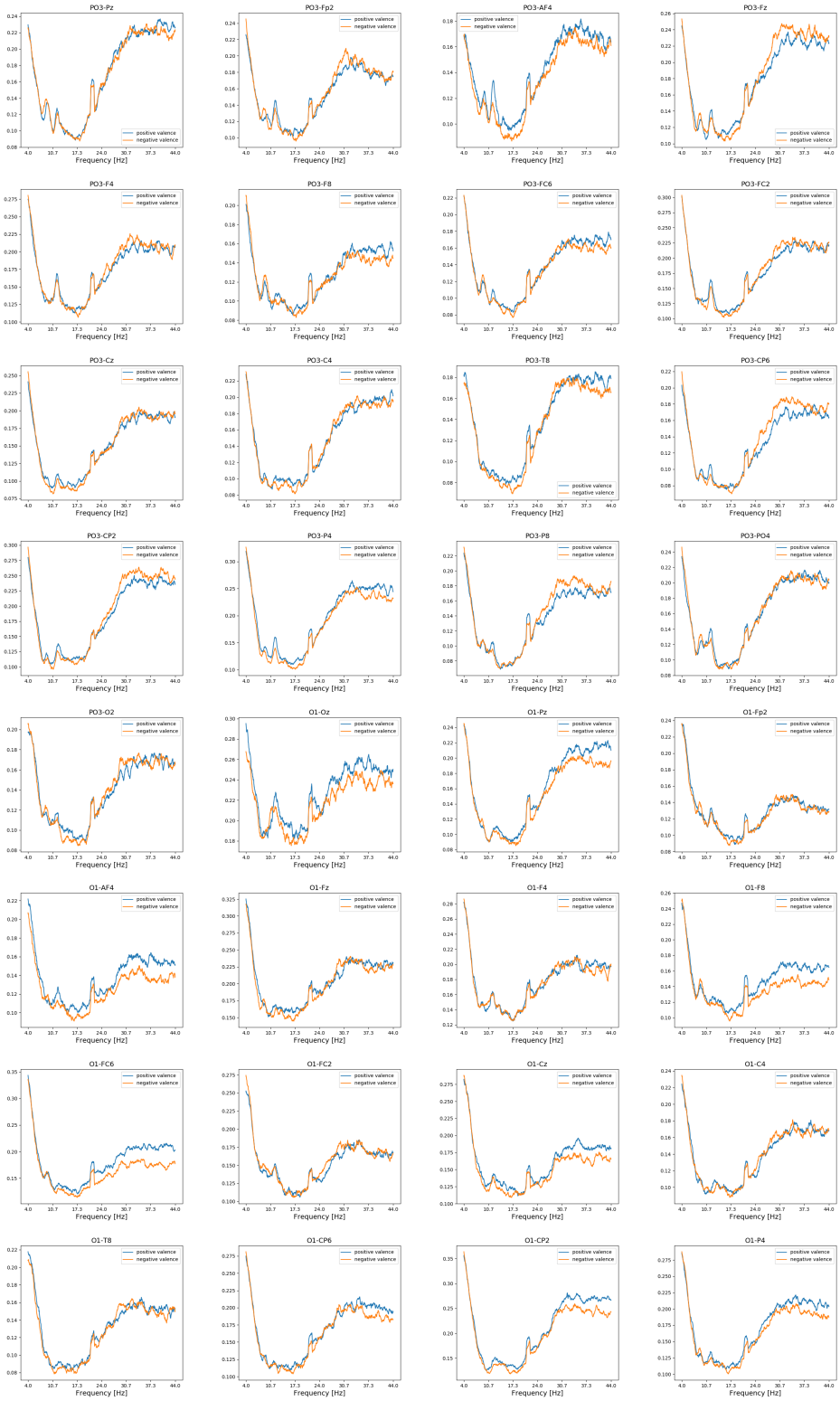
PO3-Pz
PO3-Fp2
PO3-AF4
PO3-Fz
PO3-F4
PO3-F8
PO3-FC6
PO3-FC2
PO3-Cz
PO3-C4
PO3-T8
PO3-CP6
PO3-CP2
PO3-P4
PO3-P8
PO3-PO4
PO3-O2
O1-Oz
O1-Pz
O1-Fp2
O1-AF4
O1-Fz
O1-F4
O1-F8
O1-FC6
O1-FC2
O1-Cz
O1-C4
O1-T8
O1-CP6
O1-CP2
O1-P4
positive valence
negative valence
Frequency [Hz]

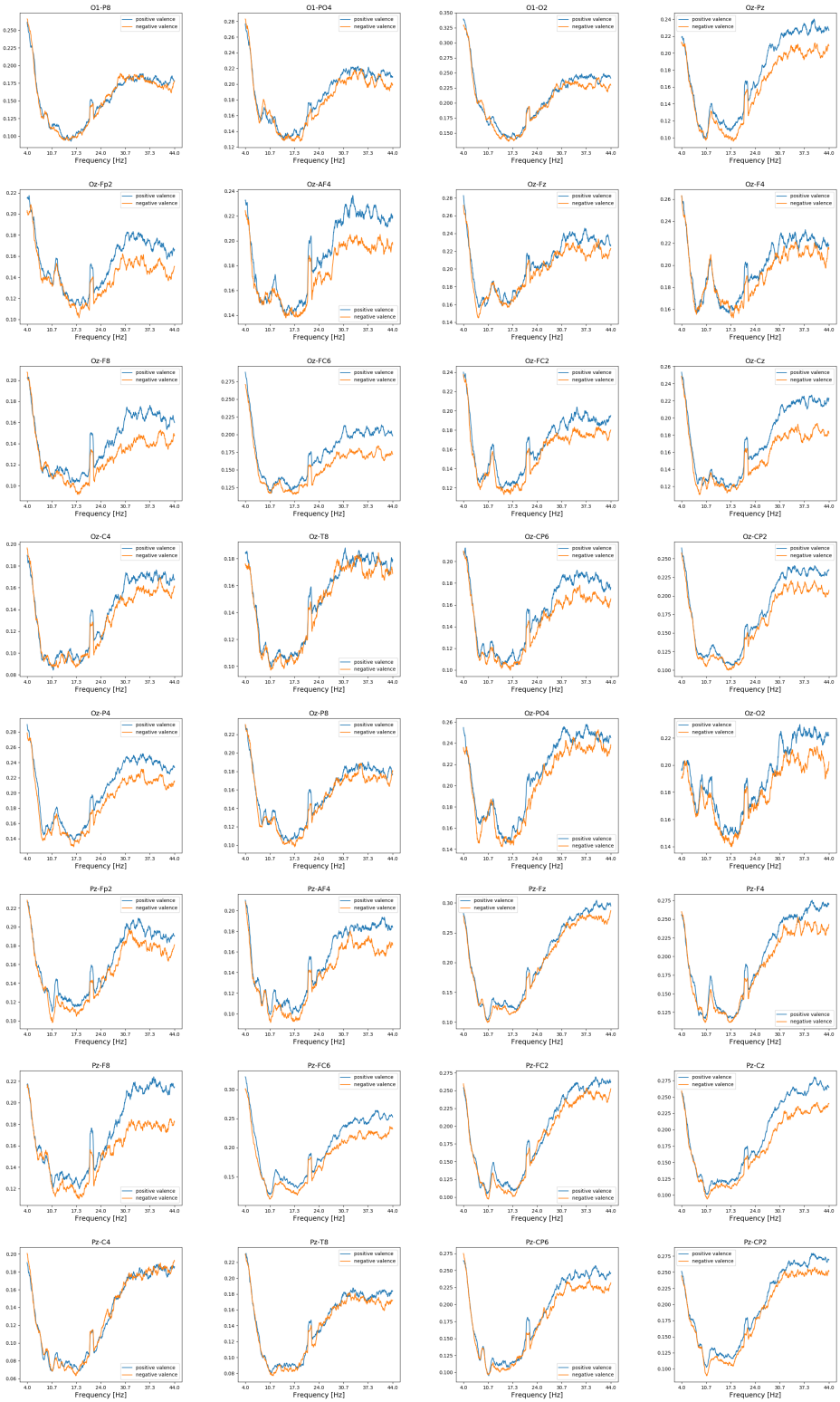
O1-P8
O1-PO4
O1-O2
Oz-Pz
Oz-Fp2
Oz-AF4
Oz-Fz
Oz-F4
Oz-F8
Oz-FC6
Oz-FC2
Oz-Cz
Oz-C4
Oz-T8
Oz-CP6
Oz-CP2
Oz-P4
Oz-P8
Oz-PO4
Oz-O2
Pz-Fp2
Pz-AF4
Pz-Fz
Pz-F4
Pz-F8
Pz-FC6
Pz-FC2
Pz-Cz
Pz-C4
Pz-T8
Pz-CP6
Pz-CP2
positive valence
negative valence
Frequency [Hz]

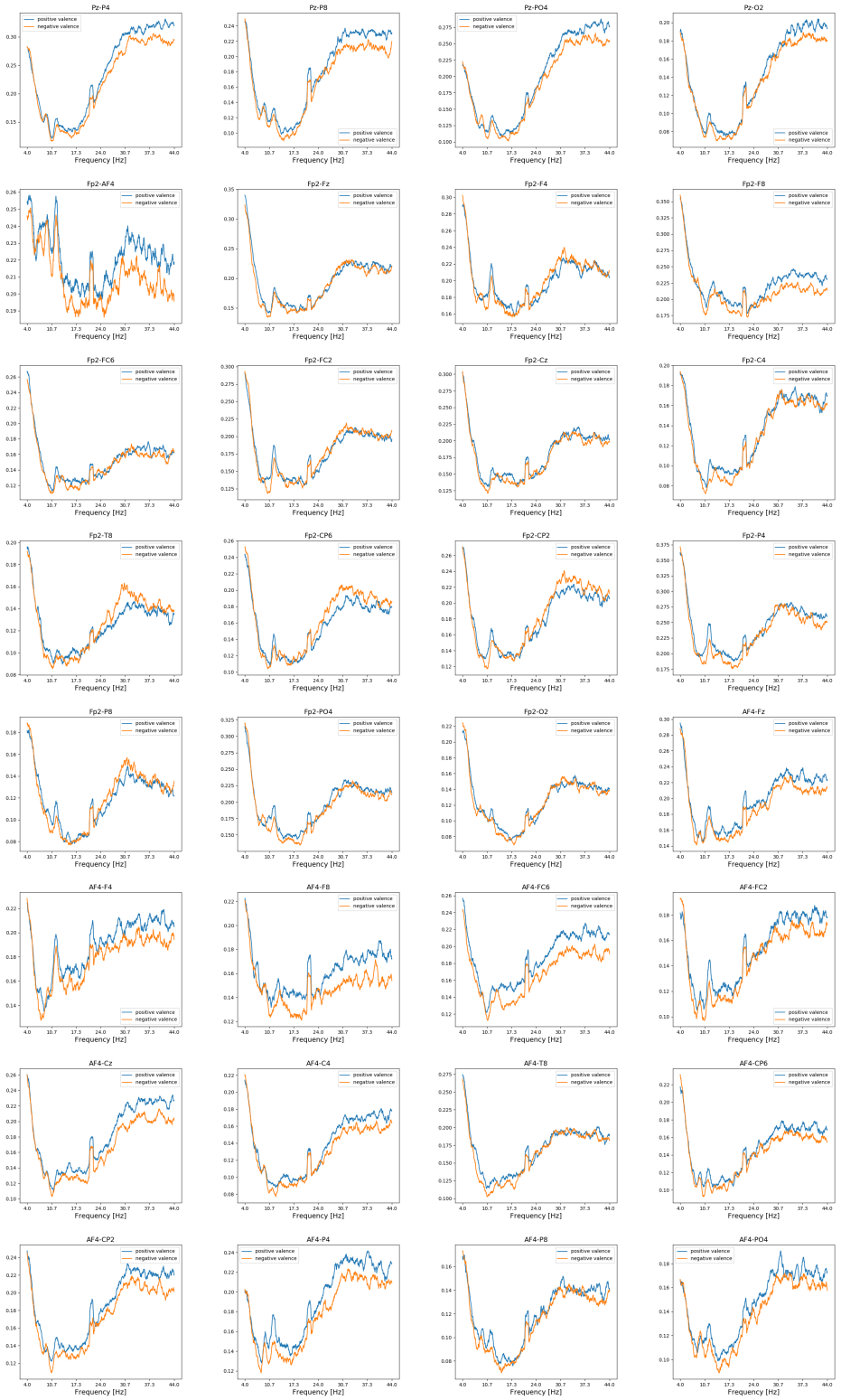
Pz-P4
Pz-P8
Pz-PO4
Pz-O2
Fp2-AF4
Fp2-Fz
Fp2-F4
Fp2-F8
Fp2-FC6
Fp2-FC2
Fp2-Cz
Fp2-C4
Fp2-T8
Fp2-CP6
Fp2-CP2
Fp2-P4
Fp2-P8
Fp2-PO4
Fp2-O2
AF4-Fz
AF4-F4
AF4-F8
AF4-FC6
AF4-FC2
AF4-Cz
AF4-C4
AF4-T8
AF4-CP6
AF4-CP2
AF4-P4
AF4-P8
AF4-PO4
positive valence
negative valence
Frequency [Hz]

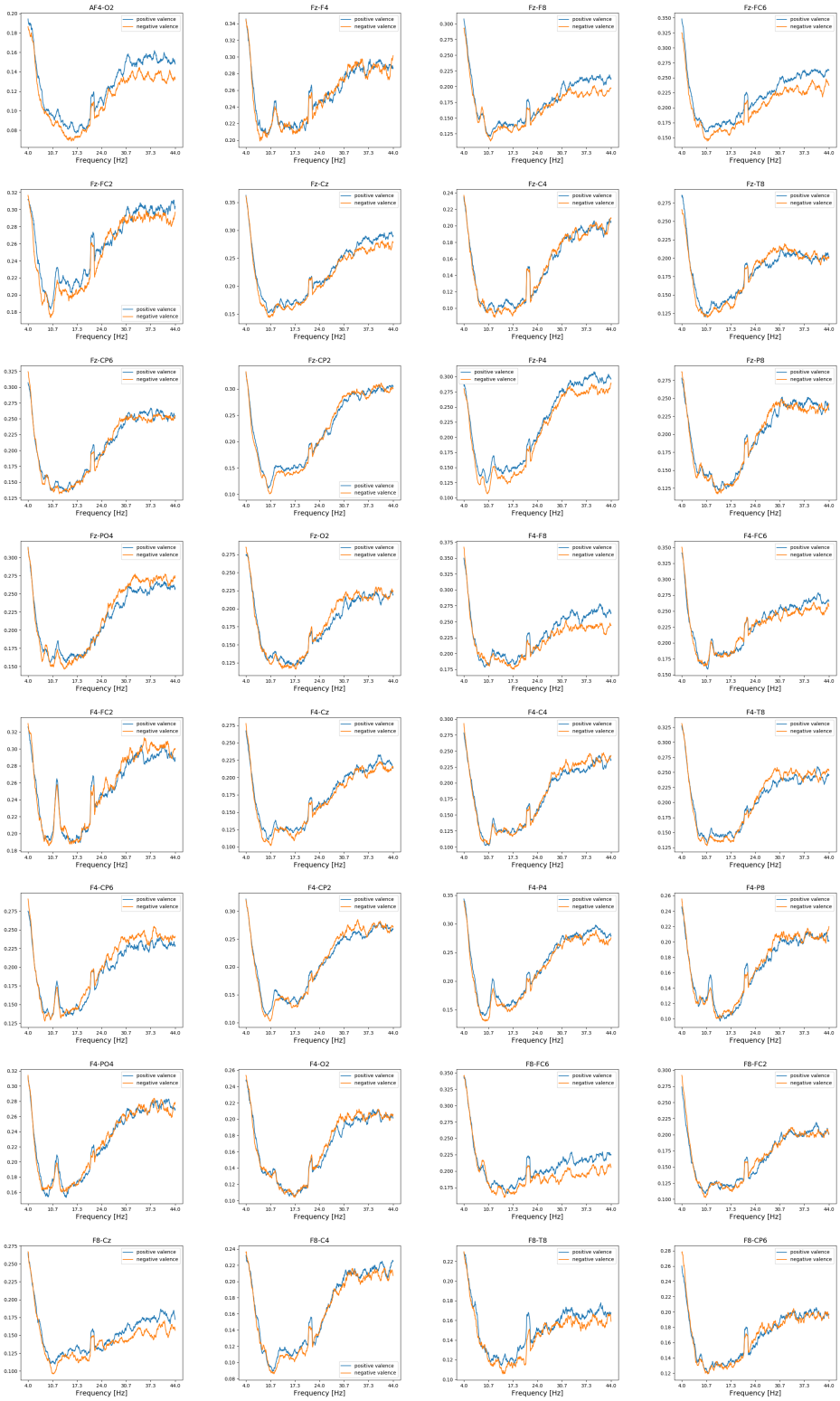
AF4-O2
Fz-F4
Fz-F8
Fz-FC6
Fz-FC2
Fz-Cz
Fz-C4
Fz-T8
Fz-CP6
Fz-CP2
Fz-P4
Fz-P8
Fz-PO4
Fz-O2
F4-F8
F4-FC6
F4-FC2
F4-Cz
F4-C4
F4-T8
F4-CP6
F4-CP2
F4-P4
F4-P8
F4-PO4
F4-O2
F8-FC6
F8-FC2
F8-Cz
F8-C4
F8-T8
F8-CP6
positive valence
negative valence
Frequency [Hz]

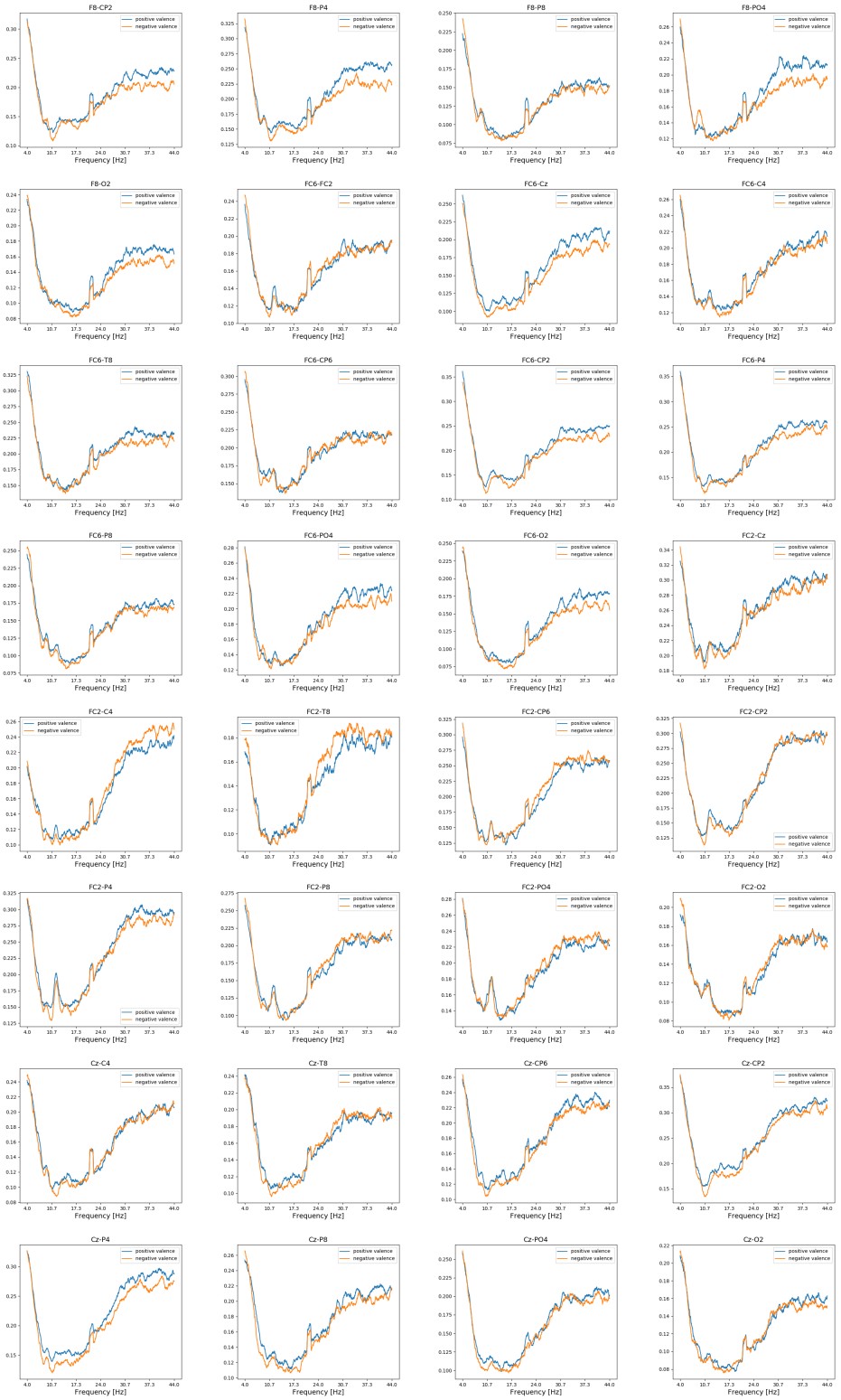
F8-CP2
F8-P4
F8-P8
F8-PO4
F8-O2
FC6-FC2
FC6-Cz
FC6-C4
FC6-T8
FC6-CP6
FC6-CP2
FC6-P4
FC6-P8
FC6-PO4
FC6-O2
FC2-Cz
FC2-C4
FC2-T8
FC2-CP6
FC2-CP2
FC2-P4
FC2-P8
FC2-PO4
FC2-O2
Cz-C4
Cz-T8
Cz-CP6
Cz-CP2
Cz-P4
Cz-P8
Cz-PO4
Cz-O2
positive valence
negative valence
Frequency [Hz]

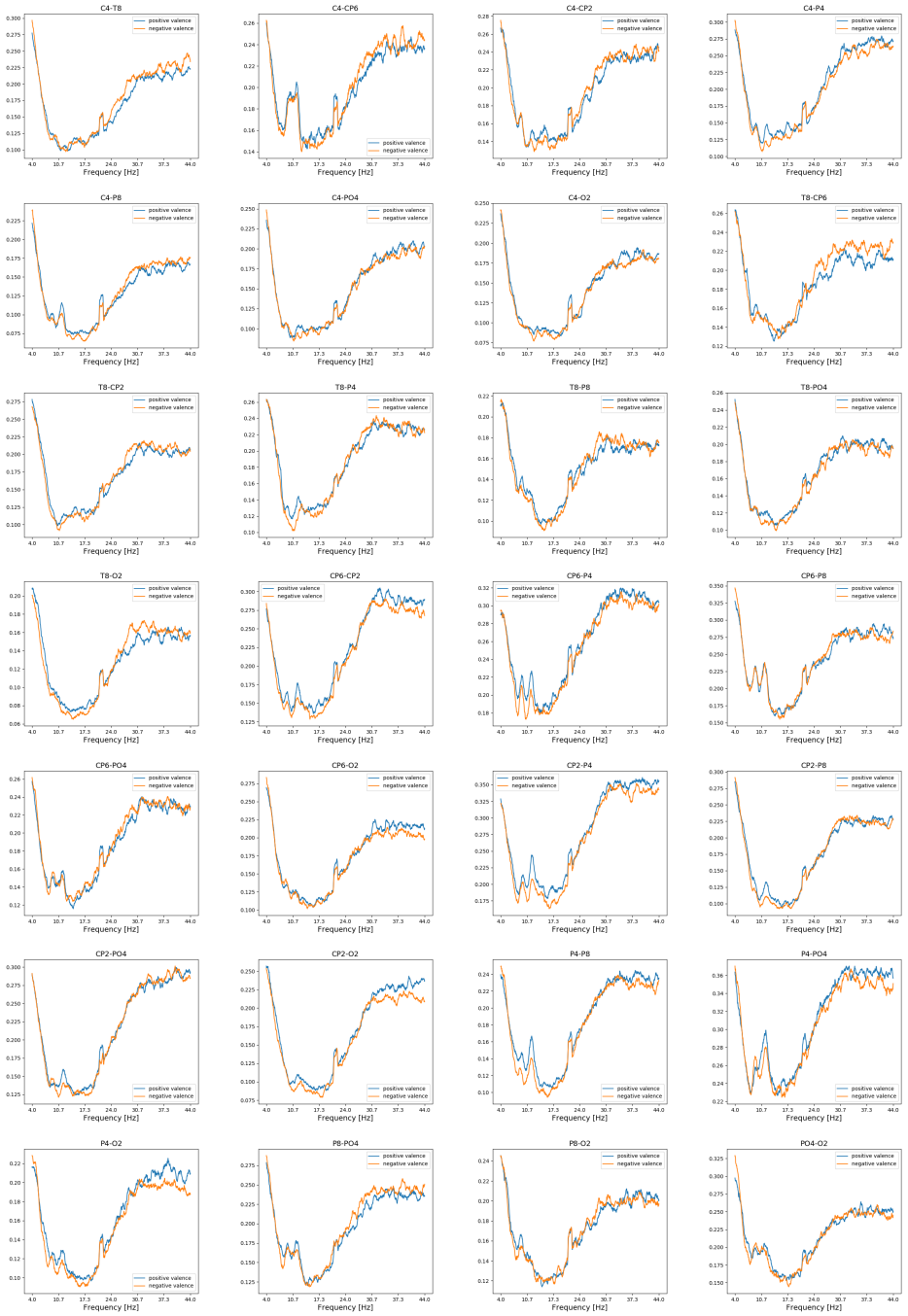
C4-T8
C4-CP6
C4-CP2
C4-P4
C4-P8
C4-PO4
C4-O2
T8-CP6
T8-CP2
T8-P4
T8-P8
T8-PO4
T8-O2
CP6-CP2
CP6-P4
CP6-P8
CP6-PO4
CP6-O2
CP2-P4
CP2-P8
CP2-PO4
CP2-O2
P4-P8
P4-PO4
P4-O2
P8-PO4
P8-O2
PO4-O2
positive valence
negative valence
Frequency [Hz]

APPENDIX B

FIGURE SET 2

$DSI_i(f)$ for combined spectral characteristics per channel and frequency in two cases of valence and arousal are shown in Figure B.1. We notice that the corresponding color bars are with much smaller ranges compared with $DSI_i^{AA}(f)$ or $DSI_i^{\phi\phi}(f)$ in all cases, and that all four panels do not show interesting patterns in terms of channels (brain regions).

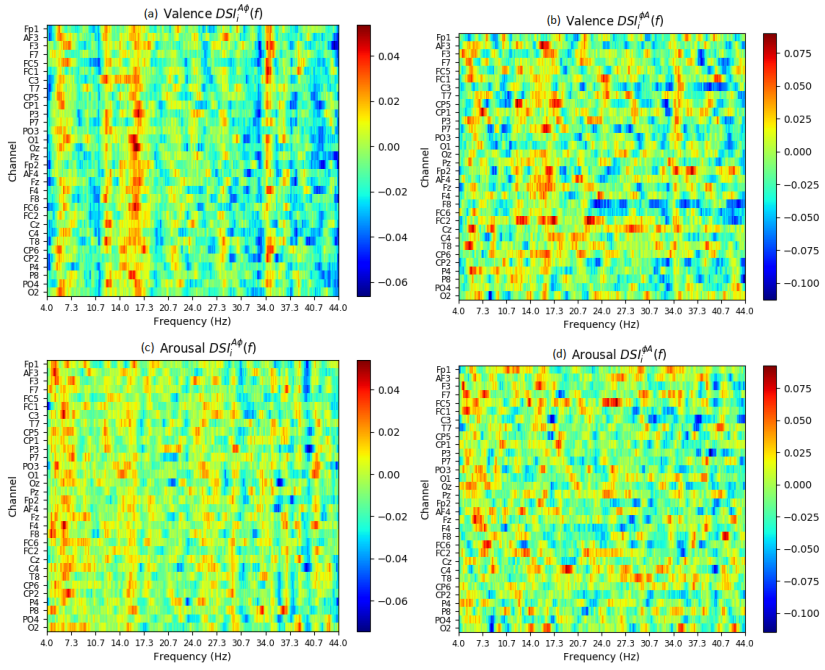

Figure B.1: (a) $DSI_i^{A\phi}(f)$ and (b) $DSI_i^{\phi A}(f)$ for different channels (vertical axis) and frequencies (horizontal axis) in valence, (c) $DSI_i^{A\phi}(f)$ and (d) $DSI_i^{\phi A}(f)$ for different channels and frequencies in arousal. For visualization purposes a moving average filter of length 30 is applied on the horizontal axis.

BIBLIOGRAPHY

[1] File:science edunihgovinfo fig02.gif. URL `https://commons.wikimedia.org/wiki/File:Science_edunihgovinfo_fig02.gif`. Retrieved on 2018-02-17.

[2] R. Reilly and T.C. Lee. Electrograms (ECG, EEG, EMG, EOG). *Technology And Health Care: Official Journal Of The European Society For Engineering And Medicine*, 18(6):443 – 458, 2010.

[3] Jake. Example: Fourier transform. URL `http://pgfplots.net/tikz/examples/fourier-transform/`. Retrieved on 2018-02-20.

[4] J. Russell. A circunplex model of affect. *Journal of Personality and Social Psychology*, 39(6):1161–1178, 1980.

[5] S. Koelstra, C. Muhl, M. Soleymani, J. S. Lee, A. Yazdani, T. Ebrahimi, T. Pun, A. Nijholt, and I. Patras. DEAP: A database for emotion analysis using physiological signals. *IEEE Transactions on Affective Computing*, 3(1):18–31, 2012.

[6] V. Mishra, B. Karumuri, N. Gautier, R. Liu, T. Hutson, S. Vanhoof-Villalba, I. Vlachos, L. Iasemidis, and E. Glasscock. Scn2a deletion improves survival and brain–heart dynamics in the kcna1-null mouse model of sudden unexpected death in epilepsy (SUDEP). *Human Molecular Genetics*, 26(11):2091–2103, 2017.

[7] I. W. Hunter and M. J. Korenberg. The identification of nonlinear biological systems: Wiener and hammerstein cascade models. *Biological Cybernetics*, 55 (2):135–144, Nov 1986.

[8] Michael J. Korenberg and Ian W. Hunter. The identification of nonlinear biological systems: Volterra kernel approaches. *Annals of Biomedical Engineering*, 24(2):250–268, Mar 1996.

[9] D. Brillinger. Some data analyses using mutual information. *Brazilian Journal of Probability and Statistics*, 18(2):163–182, 2004.

[10] H. Haken and H.P. Koepchen. *Rhythms in Physiological Systems: Proceedings of the International Symposium at Schloß Elmau, Bavaria, October 22–25, 1990*. Springer Berlin Heidelberg, 2012.

[11] E. Glaser. *Principles of neurobiological signal analysis*. Elsevier, 2012.

[12] L. Colgin, T. Denninger, M. Fyhn, T. Hafting, T. Bonnevie, O. Jensen, M. Moser, and E. Moser. Frequency of gamma oscillations routes flow of information in the hippocampus. *Nature*, 462(7271):353 – 357, 2009.

[13] L. Lewis, K. Setsompop, B. Rosen, and J. Polimeni. Fast fMRI can detect oscillatory neural activity in humans. *Proceedings of the National Academy of Sciences*, 113(43):E6679–E6685, 2016.

[14] J. Jeong. EEG dynamics in patients with alzheimer's disease. *Clinical Neurophysiology*, 115(7):1490 – 1505, 2004.

[15] D. Abásolo, J. Escudero, R. Hornero, C. Gómez, and P. Espino. Approximate entropy and auto mutual information analysis of the electroencephalogram in alzheimer's disease patients. *Medical & Biological Engineering & Computing*, 46 (10):1019–1028, 2008.

[16] R. Hornero, J. Escudero, A. Fernández, J. Poza, and C. Gómez. Spectral and nonlinear analyses of MEG background activity in patients with alzheimer's disease. *IEEE Transactions on Biomedical Engineering*, 55(6):1658 – 1665, 2008.

[17] S. Ramgopal, S.Thome-Souza, M. Jackson, N. Kadish, I. Fernndez, J. Klehm, W. Bosl, C. Reinsberger, S. Schachter, and T. Loddenkemper. Seizure detection, seizure prediction, and closed-loop warning systems in epilepsy. *Epilepsy & Behavior*, 37(Supplement C):291 – 307, 2014.

[18] J. David, S. Jones, and D. Giddens. Modern spectral analysis techniques for blood flow velocity and spectral measurements with pulsed doppler ultrasound. *IEEE Transactions on Biomedical Engineering*, 38(6):589–596, 1991.

[19] A. Vakkuri, A. Yli-Hankala, P. Talja, S. Mustola, H. Tolvanen-Laakso, T. Sampson, and H. Viertiö-Oja. Time-frequency balanced spectral entropy as a measure of anesthetic drug effect in central nervous system during sevoflurane, propofol, and thiopental anesthesia. *Acta Anaesthesiologica Scandinavica*, 48(2): 145–153, 2004.

[20] G. Pfurtscheller, A. Schwerdtfeger, A. Seither-Preisler, C. Brunner, C. Aigner, J. Brito, M. Carmo, and A. Andrade. Brain-heart communication: Evidence for central pacemaker oscillations with a dominant frequency at 0.1 hz in the cingulum. *Clinical Neurophysiology*, 128(1):183–193, 2017.

[21] D. Hoyer, U. Leder, H. Hoyer, B. Pompe, M. Sommer, and U. Zwiener. Mutual information and phase dependencies: measures of reduced nonlinear cardiorespiratory interactions after myocardial infarction. *Medical Engineering & Physics*, 24(1):33 – 43, 2002.

[22] F. Azevedo, L. R.B. Carvalho, L. Grinberg, J. Farfel, R. E.L. Ferretti, R. E.P. Leite, W. Jacob Filho, and S. Lent, R.and Herculano-Houzel. Equal numbers of neuronal and nonneuronal cells make the human brain an isometrically scaled-up primate brain. *The Journal of Comparative Neurology*, 513:532–41, 04 2009.

[23] K. Brodmann. *Vergleichende Lokalisationslehre der Grosshirnrinde in ihren Prinzipien dargestellt auf Grund des Zellenbaues*. Barth, 1909.

[24] E. Kandel, J. Schwartz, T. Jessell, S. Siegelbaum, A. Hudspeth, et al. *Principles of neural science*, volume 4. McGraw-hill New York, 2000.

[25] H. Jasper. Report of the committee on methods of clinical examination in electroencephalography. *Electroencephalography and Clinical Neurophysiology*, 10:370–375, 1958.

[26] A. Lutz, L.L. Greischar, N.B. Rawlings, M. Ricard, and R.J. Davidson. Long-term meditators self-induce high-amplitude gamma synchrony during mental practice. 101(46):16369–16373, 2004.

[27] D. Lehmann, P.L. Faber, P. Achermann, D. Jeanmonod, L.R. Gianotti, and D. Pizzagalli. Brain sources of eeg gamma frequency during volitionally meditation-induced, altered states of consciousness, and experience of the self.

Psychiatry Research: Neuroimaging, 108(2):111 – 121, 2001.

[28] J. Fell, N. Axmacher, and S. Haupt. From alpha to gamma: electrophysiological correlates of meditation-related states of consciousness. *Medical hypotheses*, 75 (2):218–224, 2010.

[29] S. Marple and S. Marple. *Digital spectral analysis: with applications*, volume 5. Prentice-Hall Englewood Cliffs, NJ, 1987.

[30] I. Abdel-Qader, O. Abudayyeh, and M.E. Kelly. Analysis of edge-detection techniques for crack identification in bridges. *Journal of Computing in Civil Engineering*, 17(4):255–263, 2003.

[31] H Laufs, A Kleinschmidt, A Beyerle, E Eger, A Salek-Haddadi, C Preibisch, and K Krakow. EEG-correlated fMRI of human alpha activity. *NeuroImage*, 19 (4):1463 – 1476, 2003.

[32] C.M. Harris. The fourier analysis of biological transients. *Journal of neuroscience methods*, 83(1):15–34, 1998.

[33] M. Cain, H. Ambos, F. Witkowski, and B. Sobel. Fast-fourier transform analysis of signal-averaged electrocardiograms for identification of patients prone to sustained ventricular tachycardia. *Circulation*, 69(4):711–720, 1984.

[34] E.J. Van der Schee and J.L. Grashuis. Running spectrum analysis as an aid in the representation and interpretation of electrogastrographic signals. *Medical and Biological Engineering and Computing*, 25(1):57–62, 1987.

[35] M. Talebinejad, A. Chan, A. Miri, and R. Dansereau. Fractal analysis of surface electromyography signals: a novel power spectrum-based method. *Journal of electromyography and kinesiology*, 19(5):840–850, 2009.

[36] R.V. Hogg, J.W. McKean, and A.T. Craig. *Introduction to Mathematical Statistics*. Pearson, 2013.

[37] R. Challis and R. Kitney. Biomedical signal processing (in four parts). Part 3. The power spectrum and coherence function. *Medical & Biological Engineering & Computing*, 29(3):225–241, 1991.

[38] ShouYan Wang and MengXing Tang. Exact confidence interval for magnitude-squared coherence estimates. *IEEE Signal Processing Letters*, 11(3):326–329, March 2004.

[39] D. Baldocchi, E. Falge, and K. Wilson. A spectral analysis of biosphereatmosphere trace gas flux densities and meteorological variables across hour to multi-year time scales. *Agricultural and Forest Meteorology*, 107(1):1 – 27, 2001.

[40] R. Worsnop, G. Bryan, J. Lundquist, and J. Zhang. Using large-eddy simulations to define spectral and coherence characteristics of the hurricane boundary layer for wind-energy applications. *Boundary-Layer Meteorology*, 165(1):55–86, 2017.

[41] E. Gassmann. *Characterization of the oceanic light field within the photic zone: Fluctuations of downward irradiance and asymmetry of horizontal radiance*. University of California, San Diego, 2016.

[42] V. Miskovic and A. Keil. Reliability of event-related EEG functional connectivity during visual entrainment: Magnitude squared coherence and phase synchrony estimates. *Psychophysiology*, 52(1):81–89, 2015.

[43] L. Felix, F. de Souza Ranaudo, A. Netto, et al. A spatial approach of magnitude-squared coherence applied to selective attention detection. *Journal*

of Neuroscience Methods, 229:28–32, 2014.

[44] J. Sarnthein and D. Jeanmonod. High thalamocortical theta coherence in patients with Parkinson's disease. *Journal of Neuroscience*, 27(1):124–131, 2007.

[45] S. Kilner, J.and Baker, S. Salenius, R. Hari, and R. Lemon. Human cortical muscle coherence is directly related to specific motor parameters. *Journal of Neuroscience*, 20(23):8838–8845, 2000.

[46] B. Kocsis, A. Bragin, and G. Buzsáki. Interdependence of multiple theta generators in the hippocampus: a partial coherence analysis. *Journal of Neuroscience*, 19(14):6200–6212, 1999.

[47] B. Schelter, M. Winterhalder, M. Eichler, M. Peifer, B. Hellwig, B. Guschlbauer, C. Lücking, R. Dahlhaus, and J. Timmer. Testing for directed influences among neural signals using partial directed coherence. *Journal of Neuroscience Methods*, 152(1-2):210–219, 2006.

[48] L. Baccalá and K. Sameshima. Partial directed coherence: a new concept in neural structure determination. *Biological Cybernetics*, 84(6):463–474, 2001.

[49] C. E. Shannon. A mathematical theory of communication. *Bell System Technical Journal*, 27(3):379–423, 1948.

[50] N. Vinh, J. Epps, and J. Bailey. Information theoretic measures for clusterings comparison: Variants, properties, normalization and correction for chance. *Journal of Machine Learning Research*, 11:2837–2854, 2010.

[51] J. Bruhn, L.. Lehmann, H. Ropcke, T. Bouillon, and A. Hoeft. Shannon entropy applied to the measurement of the electroencephalographic effects of desflurane. *Anesthesiology*, 95(1):30–35, 2001.

[52] S. Kullback and R. Leibler. On information and sufficiency. *The Annals of Mathematical Statistics*, 22(1):79–86, 1951.

[53] A. Fraser and H. Swinney. Independent coordinates for strange attractors from mutual information. *Physical Review A*, 33:1134–1140, Feb 1986.

[54] B. Moon, Y.and Rajagopalan and U. Lall. Estimation of mutual information using kernel density estimators. *Physical Review E*, 52(3):2318, 1995.

[55] J. Beirlant, E. Dudewicz, L. Györfi, and E. Van der Meulen. Nonparametric entropy estimation: An overview. *International Journal of Mathematical and Statistical Sciences*, 6(1):17–39, 1997.

[56] A. Kraskov, H. Stögbauer, and P. Grassberger. Estimating mutual information. *Physical Review E*, 69(6):066138, 2004.

[57] S. Gao, G. Ver Steeg, and A. Galstyan. Efficient estimation of mutual information for strongly dependent variables. In *Artificial Intelligence and Statistics*, pages 277–286, 2015.

[58] S. Frenzel and B. Pompe. Partial mutual information for coupling analysis of multivariate time series. *Physical Review Letters*, 99(20):204101, 2007.

[59] T.M. Cover and J.A. Thomas. *Elements of Information Theory*. Wiley-Interscience, 07 2006.

[60] G. Michaels, D. Carr, M. Askenazi, S. Fuhrman, X. Wen, and R. Somogyi. Cluster analysis and data visualization of large-scale gene expression data. In *Pacific Symposium on Biocomputing*, volume 3, pages 42–53, 1998.

[61] A. Butte and I. Kohane. Mutual information relevance networks: functional genomic clustering using pairwise entropy measurements. In *Biocomputing 2000*, pages 418–429. World Scientific, 1999.

[62] R. Steuer, J. Kurths, C. Daub, J. Weise, and J. Selbig. The mutual information: detecting and evaluating dependencies between variables. *Bioinformatics*, 18 (suppl 2):S231–S240, 2002.

[63] J. Jeong, J. Gore, and B. Peterson. Mutual information analysis of the EEG in patients with Alzheimer's disease. *Clinical Neurophysiology*, 112(5):827 – 835, 2001.

[64] S. Na, S. Jin, S. Kim, and B. Ham. EEG in schizophrenic patients: mutual information analysis. *Clinical Neurophysiology*, 113(12):1954 – 1960, 2002.

[65] A. Mehrabian and J. Russell. *An approach to environmental psychology.* The MIT Press, 1974.

[66] S. Umeda. Emotion, personality, and the frontal lobe. In *Emotions of Animals and Humans*, pages 223–241. Springer, 2012.

[67] Y. Liu, O. Sourina, and M. Nguyen. Real-time EEG-based human emotion recognition and visualization. In *Cyberworlds (CW), 2010 International Conference on*, pages 262–269. IEEE, 2010.

[68] A. Clerico, R. Gupta, and T. Falk. Mutual information between inter-hemispheric EEG spectro-temporal patterns: A new feature for automated affect recognition. In *Neural Engineering (NER), 2015 7th International IEEE/EMBS Conference on*, pages 914–917. IEEE, 2015.

[69] D. Huang, K. Guan, C.and Ang, H. Zhang, and Y. Pan. Asymmetric spatial pattern for EEG-based emotion detection. In *Neural Networks (IJCNN), The 2012 International Joint Conference on*, pages 1–7. IEEE, 2012.

[70] M. Müller, A. Keil, T. Gruber, and T. Elbert. Processing of affective pictures modulates right-hemispheric gamma band EEG activity. *Clinical Neurophysiology*, 110(11):1913–1920, 1999.

[71] Q. Luo, T. Holroyd, M. Jones, T. Hendler, and J. Blair. Neural dynamics for facial threat processing as revealed by gamma band synchronization using MEG. *NeuroImage*, 34(2):839–847, 2007.

[72] Q. Luo, D. Mitchell, X. Cheng, K. Mondillo, D. Mccaffrey, T. Holroyd, F. Carver, R. Coppola, and J. Blair. Visual awareness, emotion, and gamma band synchronization. *Cerebral Cortex*, 19(8):1896–1904, 2008.

[73] C. Mikutta, A. Altorfer, W. Strik, and T. Koenig. Emotions, arousal, and frontal alpha rhythm asymmetry during beethovens 5th symphony. *Brain Topography*, 25(4):423–430, 2012.

[74] P. Lang, M. Bradley, J. Fitzsimmons, B. Cuthbert, J. Scott, B. Moulder, and V. Nangia. Emotional arousal and activation of the visual cortex: an fMRI analysis. *Psychophysiology*, 35(2):199–210, 1998.

[75] E. Harmon-Jones, P. Gable, and C. Peterson. The role of asymmetric frontal cortical activity in emotion-related phenomena: A review and update. *Biological Psychology*, 84(3):451–462, 2010.

[76] L. Nummenmaa, H. Saarimäki, E. Glerean, A. Gotsopoulos, I. Jääskeläinen, R. Hari, and M. Sams. Emotional speech synchronizes brains across listeners and

engages large-scale dynamic brain networks. *NeuroImage*, 102:498–509, 2014.

[77] L. Nummenmaa, E. Glerean, R. Hari, and J. Hietanen. Bodily maps of emotions. *Proceedings of the National Academy of Sciences*, 111(2):646–651, 2014.

[78] J. Hietanen, E. Glerean, R. Hari, and L. Nummenmaa. Bodily maps of emotions across child development. *Developmental Science*, 19(6):1111–1118, 2016.

[79] H. Schupp, J. Markus, A. Weike, and A. Hamm. Emotional facilitation of sensory processing in the visual cortex. *Psychological Science*, 14(1):7–13, 2003.

[80] R. Canolty, E. Edwards, S. Dalal, M. Soltani, S. Nagarajan, H. Kirsch, M. Berger, N. Barbaro, and R. Knight. High gamma power is phase-locked to theta oscillations in human neocortex. *Science*, 313(5793):1626–1628, 2006.

[81] J. Yeh, C. Peng, M. Lo, C. Yeh, S. Chen, C. Wang, P. Lee, and J. Kang. Investigating the interaction between heart rate variability and sleep EEG using nonlinear algorithms. *Journal of Neuroscience Methods*, 219(2):233–239, 2013.

[82] K. Schindler, H. Leung, C.E. Elger, and K. Lehnertz. Assessing seizure dynamics by analyzing the correlation structure of multichannel intracranial EEG. *Brain*, 130(1):65–77, 2007.

[83] R. Salvador, J. Suckling, C. Schwarzbauer, and E. Bullmore. Undirected graphs of frequency-dependent functional connectivity in whole brain networks. *Philosophical Transactions of the Royal Society of London B: Biological Sciences*, 360(1457):937–946, 2005.

[84] G. Nolte, O. Bai, L. Wheaton, Z. Mari, S. Vorbach, and M. Hallett. Identifying true brain interaction from EEG data using the imaginary part of coherency. *Clinical Neurophysiology*, 115(10):2292 – 2307, 2004.

[85] C. Chen, J. Hsieh, Y. Wu, P. Lee, S. Chen, D. Niddam, T. Yeh, and Y. Wu. Mutual-information-based approach for neural connectivity during self-paced finger lifting task. *Human Brain Mapping*, 29(3):265–280, 2008.

[86] C. Lu, S. Teng, C. Hung, P. Tseng, L. Lin, P. Lee, and Y. Wu. Reorganization of functional connectivity during the motor task using EEG timefrequency cross mutual information analysis. *Clinical Neurophysiology*, 122(8):1569 – 1579, 2011.

[87] A. Gong, J. Liu, S. Chen, and Y. Fu. Time–frequency cross mutual information analysis of the brain functional networks underlying multiclass motor imagery. *Journal of Motor Behavior*, 0(0):1–14, 2017.

[88] D. Brillinger and A. Guha. Mutual information in the frequency domain. *Journal of Statistical Planning and Inference*, 137(3):1076 – 1084, 2007. Special Issue on Nonparametric Statistics and Related Topics: In honor of M.L. Puri.

[89] D. Scott. *Multivariate density estimation: theory, practice, and visualization*. John Wiley & Sons, 2015.

[90] A.W. Bowman and A. Azzalini. *Applied Smoothing Techniques for Data Analysis: The Kernel Approach with S-Plus Illustrations*. Oxford Statistical Science Series. OUP Oxford, 1997.

[91] B. W. Silverman. *Density Estimation for Statistics and Data Analysis*. Chapman & Hall, 1986.

[92] S.R. Jammalamadaka and U.J. Lund. The effect of wind direction on ozone levels: a case study. *Environmental and Ecological Statistics*, 13(3):287–298, 2006.

[93] S.R. Jammalamadaka, A. Sengupta, and A. Sengupta. *Topics in Circular Statistics*. Series on multivariate analysis. World Scientific, 2001.

[94] M. Marzio, A. Panzera, and C.C. Taylor. Kernel density estimation on the torus. *Journal of Statistical Planning and Inference*, 141(6):2156 – 2173, 2011.

[95] M. Babtlett. Smoothing periodograms from time-series with continuous spectra. *Nature*, 161(4096):686, 1948.

[96] P. Welch. The use of fast fourier transform for the estimation of power spectra: A method based on time averaging over short, modified periodograms. *IEEE Transactions on Audio and Electroacoustics*, 15(2):70–73, June 1967.

[97] J. Muthuswamy. Biomedical signal analysis. In M. Kutz, editor, *Standard Handbook of Biomedical Engineering and Design*, chapter 21. McGraw-Hill, 2 edition, 2009.

[98] W. Klonowski. Everything you wanted to ask about EEG but were afraid to get the right answer. *Nonlinear Biomedical Physics*, 3:2, 02 2009.

[99] L. Glass and M.C. Mackey. *From Clocks to Chaos: The Rhythms of Life*. Princeton paperbacks. Princeton University Press, 1988.

[100] E. Lorenz. Deterministic nonperiodic flow. *Journal of the Atmospheric Sciences*, 20(2):130–141, 1963.

[101] J. Sun, Y. Zhao, T.i Nakamura, and M. Small. From phase space to frequency domain: A time-frequency analysis for chaotic time series. *Physical Review E*, 76(1):016220, 2007.

[102] D. Farmer, J. Crutchfield, H. Froehling, N. Packard, and R. Shaw. Power spectra and mixing properties of strange attractors. *Annals of the New York Academy of Sciences*, 357(1):453–471, 1980.

[103] T. Kreuz, F. Mormann, R. Andrzejak, A. Kraskov, K. Lehnertz, and P. Grassberger. Measuring synchronization in coupled model systems: A comparison of different approaches. *Physica D: Nonlinear Phenomena*, 225 (1):29 – 42, 2007.

[104] D. V. Senthilkumar, M. Lakshmanan, and J. Kurths. Transition from phase to generalized synchronization in time-delay systems. *Chaos: An Interdisciplinary Journal of Nonlinear Science*, 18(2):023118, 2008.

[105] I. Vlachos and D. Kugiumtzis. Nonuniform state-space reconstruction and coupling detection. *Physical Review E*, 82(1):016207, 2010.

[106] M. Mackey, L. Glass, et al. Oscillation and chaos in physiological control systems. *Science*, 197(4300):287–289, 1977.

[107] T. Demiralp, Z. Bayraktaroglu, D. Lenz, S. Junge, N. Busch, B. Maess, M. Ergen, and C. Herrmann. Gamma amplitudes are coupled to theta phase in human EEG during visual perception. *International Journal of Psychophysiology*, 64 (1):24 – 30, 2007.

[108] M. Cohen, C. Elger, and J. Fell. Oscillatory activity and phase–amplitude coupling in the human medial frontal cortex during decision making. *Journal of Cognitive Neuroscience*, 21(2):390–402, 2008.

[109] M.P. Regan and D. Regan. A frequency domain technique for characterizing nonlinearities in biological systems. *Journal of Theoretical Biology*, 133(3):293 – 317, 1988.

[110] V. Zemon and F. Ratliff. Intermodulation components of the visual evoked potential: responses to lateral and superimposed stimuli. *Biological Cybernetics*, 50(6):401–408, 1984.

[111] Z. Mohammadi, J. Frounchi, and M. Amiri. Wavelet-based emotion recognition system using EEG signal. *Neural Computing and Applications*, 28(8):1985–1990, 2017.

[112] N. Jatupaiboon, S. Pan-ngum, and P. Israsena. Real-time EEG-based happiness detection system. *The Scientific World Journal*, 2013.